

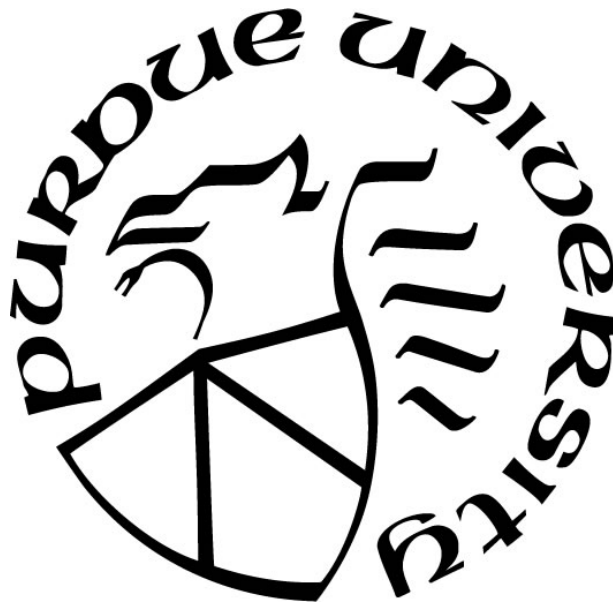
**ADULT GLIOMA MANAGEMENT WITH SELECTIVE BIOPSY, VOXEL-
WISE RADIOMICS, AND SIMULTANEOUS PET/MR IMAGING**

by
Emily Diller

A Dissertation

*Submitted to the Faculty of Purdue University
In Partial Fulfillment of the Requirements for the degree of*

Doctor of Philosophy



School of Health Sciences
West Lafayette, Indiana
August 2020

**THE PURDUE UNIVERSITY GRADUATE SCHOOL
STATEMENT OF COMMITTEE APPROVAL**

Dr. Ulrike Dydak, Co-Chair

School of Health Sciences

Dr. Jason Parker, Co-Chair

Indiana University School of Medicine

Dr. Keith Stantz

School of Health Sciences

Dr. Carlos Perez-Torres

School of Health Sciences

Approved by:

Dr. Jason Parker

For my loves Logan, Abigail, Callie, and Alistair.

ACKNOWLEDGMENTS

I wish to express my deepest gratitude to those who have helped me reach this milestone. First, Dr. Parker for the continuous support of my PhD study and research, his patience, motivation, and immense knowledge. His guidance helped me immensely during research and writing and I could not have imagined a better mentor. My advisory committee, Dr. Dydak, Dr. Stantz, and Dr. Perez-Torres, I am thankful for their insightful comments, words of encouragement, and thought-provoking questions which widened my perspective.

TABLE OF CONTENTS

LIST OF TABLES.....	8
LIST OF FIGURES	9
ABSTRACT.....	11
CHAPTER ONE: BACKGROUND AND SIGNIFICANCE	12
Glioma diagnosis and treatment.....	12
Advanced imaging techniques for glioma	15
Spatial radiomics for glioma.....	16
References.....	18
CHAPTER TWO: THE CASE REPORT.....	21
Transient neurologic deficit without vascular pathology correlates with reversible focal hypoperfusion on arterial spin-labeled perfusion imaging	21
Introduction.....	21
Case report.....	21
Discussion.....	26
References.....	28
CHAPTER THREE: BIOPSY SELECTION	31
Variation in correlation between prognosis and histologic feature based on biopsy selection .	31
Introduction.....	31
Methods	32
Data selection.	32
Data analysis.	33
Results.....	34
Clinical and genomic data for cohort.	34
Correlation between overall survival and histologic feature vary by biopsy method.	35
Correlation between progression free survival and histologic feature vary by biopsy method.	36
Correlation between prognosis and histologic feature vary by the number of biopsies selected.	37

Discussion.....	38
References.....	40
CHAPTER FOUR: VOXEL-WISE RADIOMIC MODELS	42
Predicted disease compositions of human gliomas estimated from multiparametric MRI can predict endothelial proliferation, tumor grade, and overall survival	42
Introduction.....	42
Methods	44
Patient population.....	44
Imaging Data	44
Image Annotation	47
Image Registration and Feature Vector.....	47
k-NN Radiomics Algorithm	47
Statistical Analysis	48
Results.....	50
k-NN Radiomics Algorithm Performance and Accuracy.....	50
Linear Regression.....	51
Canonical Discriminant Analysis.....	51
Discussion.....	53
Using Nosologic Imaging Algorithms to Quantitatively Standardize Grade Differentiation in Adult Primary Glioma.....	55
Predicting Individual Survival Times from Multiparametric Nosologic Imaging Classifications of Glioblastoma.....	57
Integrating Cellular and Magnetic Relaxation Properties for Multimodal Nosologic Imaging of Gliomas	59
References.....	61
CHAPTER FIVE: SIMULTANEOUS PET AND MRI.....	64
Feasibility of simultaneous dynamic PET and functional MRI studies.....	64
Introduction.....	64
Methods	64
Study design	64
Subject recruitment.....	65

Simultaneous PET/MRI design	66
PET imaging protocol	67
MRI imaging protocol	67
Auditory stimulation	68
Results.....	69
Subject recruitment	69
Initial and residual activity	70
Discussion.....	71
PET count variation during PET/MRI acquisition with multiple EPI sequences	73
References.....	75
CHAPTER SIX: OUTLOOK	76
References.....	77
APPENDIX A. SIMULTANEOUS PET AND MRI PROCEDURE INSTRUCTIONS.....	78
APPENDIX B. PET/MR PROTOCOL.....	85
PUBLICATIONS.....	107
Journal Papers	107
Conference Proceedings.....	107

LIST OF TABLES

Table 1. Clinical and genomic data for research cohort. PTEN: Phosphatase and Tensin Homolog; IDH1: Isocitrate Dehydrogenase 1; MGMT: O-6-Methylguanine-DNA Methyltransferase; PCR: Polymerase chain reaction.....	35
Table 2. Summary of clinical characteristics with Bonferroni corrected p-values.....	45
Table 3. Summary of MR Sequence Settings.....	46
Table 4. Summary of kNN model parameters.....	48
Table 5. Dice similarity coefficient (DSC) computed for each class, based on the predicted class label and ground truth class label.....	51
Table 6. Summary of Canonical Discriminant Analysis statistical findings. Accuracy, sensitivity, specificity, positive predictive value (PPV), and negative predictive value (NPV) are reported in percentage. Low (-) and high (+) state defined for CDA to maximally separate derived discriminant scores (DS). Confidence intervals (CI) were determined for each state from the DS calculated by the respective CDA model coefficients.....	52
Table 7. Inclusion and exclusion criteria for simultaneous PET and MRI study.....	65
Table 8. Initial and residual activity by completed session.....	71

LIST OF FIGURES

Figure 1. Glioma diagnosis and treatment cycle. The cycle begins with symptom presentation and is followed by a neurological and medical imaging exam. Next, a needle biopsy is taken and evaluated for histologic and molecular characteristics. If diagnosed with glioma, a treatment plan is established including resection, radiation therapy, and chemotherapy. The cycle may repeat while monitoring treatment response..... 13

Figure 2. NIH-NCI SEER data for invasive cancers of the brain and nervous system. One-year survival rates span from 1995-2016, increased survival is observed from 1995 to 2006, however survival becomes stagnant from 2006 to 2016. Meanwhile, five-year survival rate remains relatively consistent from 1995 to 2012..... 15

Figure 3. Cerebral MRI data from day of symptom onset. (A) DWI imaging showed no acute infraction; (B) FLAIR demonstrated no signal abnormalities indicative of edema; (C) ASL showed decreased cerebral perfusion on the left hemisphere with normal perfusion on the right hemisphere; (D) DCE bolus imaging confirmed asymmetric perfusion observed in ASL. 24

Figure 4. Angiography from day of symptom onset showed enlarged cerebral arteries without evidence of occlusion nor vasospasm in MRA (A) and CT (B) imaging modalities. 25

Figure 5. Cerebral MRI data one day after symptom onset. (A) ASL and (B) DCE imaging showed complete resolution of observed left hemisphere perfusion abnormality while (C) DWI demonstrated the absence of infraction..... 25

Figure 6. An example of slide annotation from IvyGAP. The tumor feature annotation (left), the annotation boundary on hematoxylin and eosin slide (center), and the tumor feature legend (right). 33

Figure 7. Correlation between prognosis and structural features across biopsy methods. (A) Correlation between overall survival (OS) and histology structural features by limited volume, needle biopsy (NB) like methods. (B) Correlation between progression free survival (PFS) and histology structural features by limited volume, needle biopsy (NB) like methods. (C) Overall survival (OS) correlation to histologic structural features using a larger volume, surgical biopsy (SB) like methods. (D) Progression free survival (PFS) correlation to histologic structural features using a larger volume, surgical biopsy (SB) like methods. (E) Correlation between prognostic factors and histologic structural features using enblock method. 37

Figure 8. Variation in correlation between prognosis and histology based on the number of biopsies taken. PFS: progression free survival; OS: overall survival. 38

Figure 9. Selected genetic mutation status defined as wild-type (light) or mutant (dark) by patient and TCGA grade class. Patients above the bold black line were diagnosed as GBM. Patients below the bold black line were diagnosed as LGG..... 49

Figure 10. Radiomics algorithm k-NN Confusion Matrix. The k-NN model accuracy was tested using a 25% hold-out method. As observed, there is strong main axis agreement between the true

and predicted classes. The accuracy for the entire model, including disease and normal tissue classes, was 97.0%. The average accuracy for the diseased classes was 95.61%. 50

Figure 11. Comparison of NIA classifications for GBM and LGG diagnosis..... 56

Figure 12. Statistical analysis for NIA percent abnormal classification between groups GBM and LGG. 56

Figure 13. Correlation between percent of tumor in class and prognosis..... 58

Figure 14. Percentage of the four conditions in one patient per diagnostic grade..... 60

Figure 15. Pictorial representation of simultaneous dynamic PET and functional MRI study. A 3T Siemens mMR scanner was used to acquire simultaneous PET/MRI data. A MEDRAD power injector delivered a solution of FDG and saline. The digital TR pulse was elongated by an Arduino then sent to the mMR scanner and recorded in the LLM data as an external signal. A projection screen was placed at the head of the participant. 66

Figure 16. Simultaneous dynamic PET and MRI protocol paradigm. The protocol begins with a localizer and MR based attenuation correction (MRAC) sequence, then the dynamic PET begins with a constant infusion rate of 0.01 ml/sec. During the dynamic PET acquisition, an anatomical T1, an ASL, and six functional MRIs are acquired. 67

Figure 17. Passive listening on-off block design. During ‘on’ white noise sound is delivered to the participant through in ear headphones. During ‘off’ no sound is delivered to the participant through in ear headphones. 68

Figure 18. Auditory Stroop correct response examples. The red dot represents the subject using the indicated finger for a response. If the sound delivered is soft or low, the subject indicates with the button under their left index finger. If the sound delivered is loud or high, the subject indicates with the button under their right index finger..... 69

Figure 19. Enrollment results by month. Total users include potential subjects that enter some personal information on the Indiana CTSI study page. Completed users have completed all required information and the digital screener. Qualified users have completed the required information and passed the digital screener. Referrals are qualified users that have requested contact from study staff. Consented users have completed the informed consent process. 70

Figure 20. Temperature and counts changes during protocol. (A) Gantry temperatures during the protocol when the gantry started at homogeneous temperature (cold). (B) Gantry temperatures during the protocol when the gantry was “warm” with residual heat from previous protocol. (C) The normalized counts for the first half of the protocol for “cold” and “warm” conditions. (D) The normalized counts for the second half of the protocol for “cold” and “warm” conditions. .. 74

ABSTRACT

Every year more than fourteen-thousand adults in the United States are diagnosed with glioma, the most common malignant tumor of the central nervous system. Gliomas arise from glue like glial cells and present with a range of grade and prognosis. Glioblastoma multiforme (GBM), a grade IV glioma, is the most common glioma subtype and carries dismal prognosis with fewer than one half of patients surviving one year after diagnosis. The standard treatment for GBM is resection followed by a cocktail of chemo and radiation therapy. Unfortunately, complete surgical resection is impossible for GBM, and intra-tumor heterogeneity, a GBM hallmark, negatively impacts chemo and radiation therapy efficacy. This thesis contains six chapters that evaluate advanced imaging and statistical methods that may be used to improve glioma management. Chapter one presents background information to establish the relationship of four subsequent studies with ranging topics on advanced imaging techniques, biopsy sampling, and radiomic analysis. In chapter two, a case report is presented that demonstrates the importance of advanced magnetic resonance imaging (MRI) such as arterial spin labeled (ASL) perfusion sequences. In this case, a patient with a benign cerebral lesion presents with receptive aphasia and of the imaging data acquired, only ASL showed decrease cerebral aphasia. Chapter three describes the impact biopsy selection has on correlation between prognostic and histologic features in 35 patients with GBM. Multiple biopsy selection methods were compared, resulting in a wide range in correlation significance. Chapter four presents different voxel-wise radiomic models in adult glioma patients. From one voxel-wise radiomic model, predicted disease compositions (PDC) were computed in 17 glioma patients and were able to significantly ($\alpha = 0.05$) predict overall survival, tumor grade, and endothelial proliferation. Chapter five describes the feasibility and hardware constraints of simultaneous PET/MR imaging protocols. A dynamic infusion of fluorodeoxyglucose (FDG) was administered with simultaneous MR imaging including echo planar imaging (EPI) based sequences used for functional MRI (fMRI). Heat from the EPI sequences deposited in the PET detector hardware and resulted in significant hardware failure. Finally, chapter six provides outlook and application to glioma clinical management considering the methods and findings presented in each study.

CHAPTER ONE: BACKGROUND AND SIGNIFICANCE

Glioma is the most common malignant tumor of the central nervous system, accounting for more than fourteen-thousand adult diagnoses each year in the United States^{1,2}. Glioblastoma (GBM) is the most frequent and aggressive form of glioma in adults that has not shown improved prognosis despite innovative diagnostic and therapeutic tools^{3,4}. The dismal prognosis associated with GBM is likely related to the complex intra- and inter-tumoral heterogeneity resulting from an unstable microenvironment. Recent advancements in genomics, epigenetics, and quantitative methods, such as radiomics, have led to potential predictive biomarkers. Radiomics is a recently defined field that extracts quantitative features from medical imaging data by an analytic process, the features are then mined to generate or test a hypothesis⁵. This chapter will provide background information from the perspective of adult glioma management for glioma, advanced imaging techniques, and radiomics.

Glioma diagnosis and treatment

Gliomas arise from glue like glial cells and present with a range of intensities, prognoses, and genetic characteristics. Gliomas ranging World Health Organization (WHO) grades I to IV have a median diagnostic age of 41 years with 56.6% and 32.1% of patients surviving one and five years, respectively^{6,7}. Glioblastoma multiforme (GBM), WHO grade IV glioma, is the most common and aggressive subtype⁸. The median age at diagnosis for GBM is 64 years, and despite advancements in diagnostic and treatment methods the median survival is only 14.6^{1,8}.

Similar to other neoplasms, GBM follows a diagnosis-treatment cycle (Figure 1) including symptom presentation, medical imaging, biopsy, resection, radiation therapy, and chemotherapy. Although rare, cases of recurrent GBM may present resulting in subsequent iterations of the diagnosis-treatment cycle. The diagnosis-treatment cycle begins with symptom presentation, which may vary by tumor size, location in the brain, and growth rate. Common symptoms of GBM include headache, nausea or vomiting, confusion, memory loss, personality changes, balance changes, changes in vision, speech difficulties, and/or seizures. If a neurological exam indicates an issue in vision, hearing, balance, coordination, strength or reflexes, medical imaging tests are ordered. Magnetic resonance imaging (MRI) is the preferred

modality due to soft tissue differentiation and sequence availability, however imaging with other modalities like computerized tomography (CT) and positron emission tomography (PET) may be used.



Figure 1. Glioma diagnosis and treatment cycle. The cycle begins with symptom presentation and is followed by a neurological and medical imaging exam. Next, a needle biopsy is taken and evaluated for histologic and molecular characteristics. If diagnosed with glioma, a treatment plan is established including resection, radiation therapy, and chemotherapy. The cycle may repeat while monitoring treatment response.

Next, an abnormal tissue needle biopsy is collected, localized or guided by medical imaging data. The biopsy undergoes histologic analysis to determine pathologic and molecular characteristics. Histopathology of GBM is variable due to intra-tumoral heterogeneity, however the most common features used to diagnose GBM is the presence of necrosis and/or prominent angiogenesis (microvascular proliferation)⁸. GBM can be classified as primary or secondary, where primary occurs without a prior glioma and secondary develops from a prior glioma. Approximately 90% of GBMs are primary and tend to be older compared to secondary GBM⁹.

Although the macro- and microscopic presentations of primary and secondary GBM are indistinguishable, they have different trends in genomic alterations. Primary GBMs typically

have alterations to the RTK pathway, EGFR, PTN, and chromosome 10, where secondary GBM commonly have alterations to IDH1, TP53, and chromosome 19q¹⁰⁻¹³. Crucially, IDH1 mutation is associated with increased overall survival (OS) and is used to differentiate primary from secondary GBM. The hallmark therapeutic approach for GBM is surgery, however complete resection is impossible due to infiltrative cells. Following resection with radiotherapy and chemotherapy, such as temozolomide (TMZ) and bevacizumab, has improved progression free survival (PFS) but not OS¹⁴.

Regardless of ideal treatment, almost all patients experience recurrence, progression, and ultimately mortality. In a study by deSouza et al, survival outcomes for GBM patients were compared over a ten-year period, between 1999-2000 (n=133) and 2009-2010 (n=184)¹⁵. The one-year survival rates were 20.7% and 40.0% for patients in 1999-2000 and 2009-2010 respectively, and statistical analysis was significant at P<0.001. The median overall survival was 0.36 and 0.74 years in 1999-2000 and 2009-2010 respectively. The authors credit significant improvement in one-year survival to adopting evidence based treatment protocols, specifically conjunctive radiation and chemotherapy. The National Cancer Institute (NCI) of the National Institute of Health (NIH) established the Surveillance, Epidemiology, and End Results Program (SEER) to catalog incident data of various diseases between 1975 to 2017⁶. The SEER data published one- and five-year survival rates for invasive cancers of the brain and nervous system as shown in Figure 2. The data demonstrates increased one-year survival rate between 1999-2000 and 2009-2010 consistent with deSouza et al findings, however between 2009-2010 and 2015-2016 one-year survival has become stagnant. Potential explanations for the recent plateau in survival rate may be found in the diagnosis-treatment cycle, specifically how medical imaging and biopsy data are used in treatment planning and management.

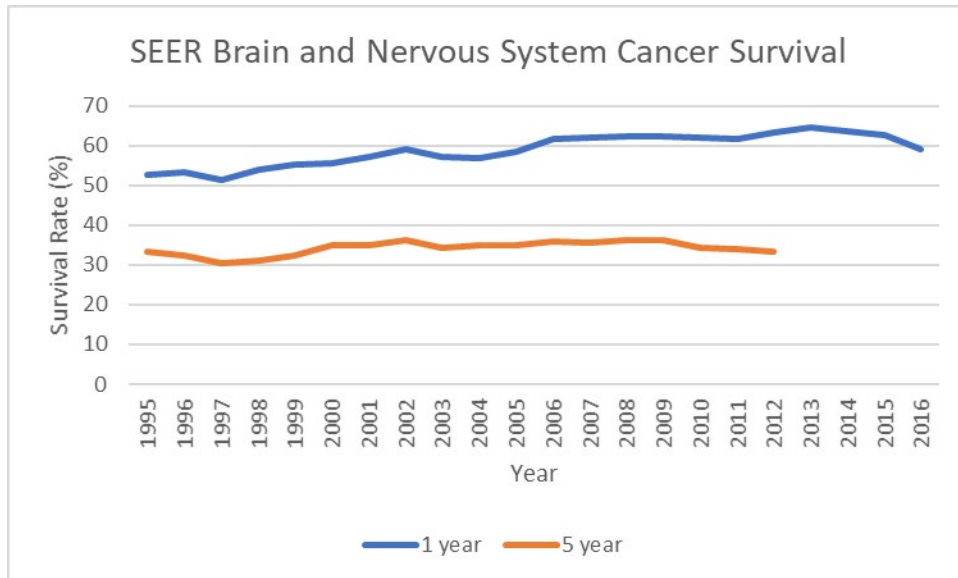


Figure 2. NIH-NCI SEER data for invasive cancers of the brain and nervous system. One-year survival rates span from 1995-2016, increased survival is observed from 1995 to 2006, however survival becomes stagnant from 2006 to 2016. Meanwhile, five-year survival rate remains relatively consistent from 1995 to 2012.

Advanced imaging techniques for glioma

As discussed above, the diagnostic gold standard for glioblastoma (GBM) includes medical imaging and biopsy confirmation. In GBM, the preferred imaging technique is magnetic resonance imaging (MRI), however protocol parameters vary greatly across institutions, providers, and vendors. Recently, guidelines for a standardized brain tumor imaging protocol have been proposed by the Jumpstarting Brain Tumor Drug Development Coalition Imaging Standardization Steering Committee³. The committee proposed minimum standards for GBM imaging to include five acquisitions: (1) pre-contrast, isotropic 3D T1-weighted (T1w); (2) pre-contrast, axial 2D T2-weighted fluid-attenuated inversion recovery (FLAIR); (3) pre-contrast, axial 2D, 3-directional diffusion-weighted images (DWI); (4) post-contrast axial 2D T2-weighted (T2w); and (5) post-contrast, isotropic 3D T1w. Although the recommended standards improve parameter consistency within and across institutions, it fails to maximize quantitative imaging techniques. Sequences such as T1w, T2w, and FLAIR are helpful in describing qualitative anatomic features but cannot provide quantitative or functional insight on their own. Thus, explicit comparison between patient data is inappropriate, requiring additional feature extraction

(i.e. size, location, etc). In contrast, advanced MRI and positron emission tomography (PET) provide quantitative data that may be compared across a GBM cohort.

Advanced MRI techniques provide quantitative and functional measurements relevant to GBM diagnosis and prognosis. Arterial spin labelling (ASL) is a perfusion imaging technique that is both non-invasive and non-ionizing. In GBM, ASL can differentiate progression from pseudoprogression, and is a reliable alternative to extrinsic contrast methods¹⁷. DWI measures the diffusion (random Brownian motion) of water molecules in a voxel. The apparent diffusion coefficient (ADC), is a quantitative measurement calculated from DWI and correlates with glioma grades¹⁸. MR spectroscopy (MRS) measures the concentration of metabolites within a volume, and for GBM patients the spectrum is often characterized by an increased choline, lactate, and lipids, with decreased NAA and myoinositol¹⁹. Functional MRI (fMRI) is a task-based technique that identifies areas of the brain with increased oxygenated blood volumes. For GBM, fMRI is a useful tool for resection planning since it can illuminate important regions and connectomes of the brain²⁰.

PET is a nuclear imaging technique and provides crucial biological insight for GBM, unavailable in advanced MRI techniques. The most widely used, validated, available, and cost-effective PET radiotracer is ¹⁸F-2-fluoro-2-deoxy-D-glucose (FDG)¹⁶. FDG is linked to cellular metabolic activity since it is a glucose analogue, generally uptake is greater in higher grade tumors since the metabolic needs are more aggressive. In GBM, FDG is a useful radiotracer during the disease's initial stage. Recently advancements in amino acid based radiotracers, such as O-(2-[¹⁸F]-fluoroethyl)-L-tyrosine (FET), have led to increased use for GBM since sensitivity is greater compared to FDG²¹.

Spatial radiomics for glioma

Although advanced MRI sequences and genome testing have become more common and cost effective, GBM survival rates have remained stagnant. Potential explanations for the recent plateau in survival rate may be found in the diagnosis-treatment cycle, specifically how medical imaging and biopsy data are used in treatment planning and management. Acquiring multiple biopsies throughout GBM treatment and management could lead to important findings, however the burden and considerable risk is untenable.

Recently, there has been an increased interest in utilizing radiomics, an analytic method that applies machine learning techniques to medical imaging and biopsy derived data⁵. Like other aggressive oncologic diseases, GBM is characterized by intra-tumoral heterogeneity (ITH) however leading radiomics repositories, such as The Cancer Genome Atlas (TCGA) and The Cancer Imaging Archive (TCIA), are largely comprised of single location biopsy data assumed sampled from the tumor bed²². Though radiomics studies from repositories like TCGA-TCIA have been intriguing, spatial correlation between micro and macroscopic features is unreliable.

This work proposes a spatial radiomics analysis to medical imaging data with spatially registered biopsy. As previously discussed, GBM is characterized by inter- and intra-tumoral heterogeneity. This heterogeneity may be observed macroscopically, through medical imaging and gross resection, and microscopically, through biopsy derived measures like histologic and genomic features. Macroscopic heterogeneity is commonly described by medical imaging techniques, such as MRI and PET, throughout the diagnosis-treatment cycle to measure intervention response. Microscopic heterogeneity is only described through biopsy. Due to reasonable safety constraints, biopsy sampling is commonly limited to pre-intervention or at the time of resection.

A spatial radiomic approach generates unique data that spatially correlates micro- and macroscopic features across the neoplasm. Since biopsy in GBM is extremely invasive and potentially dangerous acquisition is limited. In contrast, medical imaging methods such as MRI and PET are non or minimally invasive. By utilizing spatially registered biopsy and medical imaging data, unique localized imaging features are extracted leading to correlations between micro- to macroscopic environments. Models derived from spatial radiomic methods will likely improve GBM management over the diagnosis-treatment cycle since they can quantitatively correlate features previously only available by biopsy.

References

- [1] Barnholtz-Sloan JS, Ostrom QT, Cote D. Epidemiology of Brain Tumors. *Neurol Clin.* 2018;36(3):395-419. doi:10.1016/j.ncl.2018.04.001
- [2] Louis N, Perry A, Reifenberge RG, von Deimling A, Figarella-Branger D, Cavenee WK, et al. The 2016 World Health Organization classification of tumors of the central nervous system: A summary. *Acta Neuropathol.* 2016;131:803–20.
- [3] Ellingson, Benjamin M et al. Consensus recommendations for a standardized Brain Tumor Imaging Protocol in clinical trials. *Neuro-oncology.* 2015;17(9):1188-98. doi:10.1093/neuonc/nov095
- [4] Lombardi MY, Assem M. Glioblastoma Genomics: A Very Complicated Story. *Glioblastoma.* Brisbane (AU): Codon Publications; 2017 Sep 27. doi: 10.15586/codon.glioblastoma.2017.ch1
- [5] Gillies, R.J., Kinahan, P.E., and Hricak, H. (2016). Radiomics: Images Are More than Pictures, They Are Data. *Radiology* 278, 563–577.
- [6] SEER Cancer Stat Facts: Brain and Other Nervous System Cancer. National Cancer Institute. Bethesda, MD, <https://seer.cancer.gov/statfacts/html/brain.html>
- [7] Ostrom, Q.T., Gittleman, H., Liao, P., Rouse, C., Chen, Y., Dowling, J., Wolinsky, Y., Kruchko, C., and Barnholtz-Sloan, J. (2014). CBTRUS Statistical Report: Primary Brain and Central Nervous System Tumors Diagnosed in the United States in 2007-2011. *Neuro-Oncology* 16, iv1–iv63
- [8] Louis N, Perry A, Reifenberge RG, von Deimling A, Figarella-Branger D, Cavenee WK, et al. The 2016 World Health Organization classification of tumors of the central nervous system: A summary. *Acta Neuropathol.* 2016;131:803–20.
- [9] Ohgaki H, Kleihues P. The definition of primary and secondary glioblastoma. *Clin Cancer Res.* 2013;19:764–72.
- [10] Assem M, Sibenaller Z, Agarwal S, Al-Keilani MS, Alqudah MAY, Ryken TC. Enhancing diagnosis, prognosis and therapeutic outcome prediction of gliomas using genomics. *OMICS.* 2012;16(3):113–22
- [11] Kleihues P, Ohgaki H. Primary and secondary glioblastomas: From concept to clinical diagnosis. *Neuro Oncol.* 1999;1:44–51.

- [12] Ohgaki H, Dessen P, Jourde B, Horstmann S, Nishikawa T, Di Patre PL, et al. Genetic pathways to glioblastoma: A population-based study. *Cancer Res.* 2004;64:6892–9.
- [13] Sturm D, Bender S, Jones DT, Lichter P, Grill J, Becher O, et al. Pediatric and adult glioblastoma: Multifocal (epi) genomic culprits emerge. *Nat Rev Cancer.* 2014;14(2):92–107.
- [14] Fernandes C, Costa A, Osório L, et al. Current Standards of Care in Glioblastoma Therapy. In: De Vleeschouwer S, editor. *Glioblastoma*. Brisbane (AU): Codon Publications; 2017 Sep 27. Chapter 11. doi: 10.15586/codon.glioblastoma.2017.ch1
- [15] deSouza, R.M., Shaweis, H., Han, C., Sivasubramiam, V., Brazil, L., Beaney, R., Sadler, G., Al-Sarraj, S., Hampton, T., Logan, J., et al. (2015). Has the survival of patients with glioblastoma changed over the years? *British Journal of Cancer* 114, 146–150.
- [16] Verger A, Langen KJ. PET Imaging in Glioblastoma: Use in Clinical Practice. In: De Vleeschouwer S, editor. *Glioblastoma*. Brisbane (AU): Codon Publications; 2017 Sep 27. Chapter 9. doi: 10.15586/codon.glioblastoma.2017.ch9
- [17] Jovanovic M, Radenkovic S, Stosic-Opincal T, et al. Differentiation between progression and pseudoprogression by arterial spin labeling MRI in patients with glioblastoma multiforme. *J BUON.* 2017;22(4):1061-1067.
- [18] Hilario A, Ramos A, Perez-Nuñez A et-al. The added value of apparent diffusion coefficient to cerebral blood volume in the preoperative grading of diffuse gliomas. *AJNR Am J Neuroradiol.* 2012;33 (4): 701-7. doi:10.3174/ajnr.A2846
- [19] Kalpathy-Cramer J, Gerstner ER, Emblem KE, Andronesi O, Rosen B. Advanced magnetic resonance imaging of the physical processes in human glioblastoma. *Cancer Res.* 2014;74(17):4622-4637. doi:10.1158/0008-5472.CAN-14-0383
- [20] Salama GR, Heier LA, Patel P, Ramakrishna R, Magge R, Tsiouris AJ. Diffusion Weighted/Tensor Imaging, Functional MRI and Perfusion Weighted Imaging in Glioblastoma-Foundations and Future. *Front Neurol.* 2018;8:660. Published 2018 Jan 22. doi:10.3389/fneur.2017.00660
- [21] Demetriades AK, Almeida AC, Bhangoo RS, Barrington SF. Applications of positron emission tomography in neuro-oncology: A clinical approach. *Surg J R Coll Surg Edinb Irel.* 2014 Jun;12(3):148–57.

[22] The cancer genome atlas research network. Comprehensive, integrative genomic analysis of diffuse lower-grade gliomas. *The New England Journal of Medicine* 2015;372:2481-2498. doi: 10.1056/NEJMoa1402121

CHAPTER TWO: THE CASE REPORT

Transient neurologic deficit without vascular pathology correlates with reversible focal hypoperfusion on arterial spin-labeled perfusion imaging

Citation:

Diller E, et al. Transient Neurologic Deficit without Vascular Pathology Correlates with Reversible Focal Hypoperfusion on Arterial Spin Labeled Perfusion Imaging. *Journal of Pediatric Neurology*. 2019. 17(02):089-094. doi: 10.1055/s-0038-1660502

Introduction

The differential diagnosis for acute onset of new neurologic deficits in children is broad and often prompts magnetic resonance imaging (MRI) during initial evaluation. The most common presentations in the Pediatric Emergency Department include migraine, seizure, Bell's palsy, ischemic stroke, and conversion disorder¹. Diffusion and perfusion-weighted MRI are essential modalities for the primary evaluation of a new neurologic deficit and have high sensitivity to detect tissue ischemia and hypoperfusion, respectively².

Arterial spin-labeling (ASL) has emerged as a non-invasive technique to quantify cerebral perfusion without contrast injection. Compared to other imaging modalities, such as dynamic contrast-enhanced (DCE) perfusion, ASL is beneficial for evaluating pediatric patients due to its non-invasive technique, increased safety, convenience, high labeling efficiency, high signal-to-noise ratio, and high quantitative fidelity^{3,4}. Initial experiences with ASL have demonstrated feasibility and reliability for providing clinical information about cerebral blood flow in pediatric ischemic stroke⁵. We report the use of ASL to demonstrate the correlation between focal hypoperfusion and a neurologic deficit without evidence of vascular pathology.

Case report

A 16 year-old male presented with acute onset encephalopathy and receptive aphasia. His past medical history was significant for Type I diabetes mellitus, factor V Leiden mutation, and a remote history of right frontal stroke. Additionally, he was followed for a benign left cerebellar tonsil lesion, stable over serial examinations, with his most recent brain MRI approximately one

month prior to presentation. His medications included insulin glargine each evening and an insulin aspart sliding scale, three to five times daily. He had no history of migraine headaches. On the morning of presentation, his family found him moaning and confused. A blood glucose check at home was normal and he was brought by ambulance to the Emergency Department. After arrival he had several apneic spells and transient bradycardic events. His blood glucose, electrolytes, and a toxicology screen were normal. He would briefly open his eyes to commands, mumble incoherently, and quickly lay his head down. He would not answer questions or follow commands consistently, but would squeeze with his left hand. A head CT revealed no acute processes. He was transferred to the Pediatric Intensive Care Unit and the senior author was consulted.

Upon examination, the patient's blood pressure was 130/61, pulse 76, temperature 36.9° C, respirations 22, SpO2 96%. He was warm, well perfused, well nourished, hydrated, and athletic appearing (height 193 cm, weight 93.5 kg). He rested comfortably and quietly but with a confused expression. He was normocephalic with normal facial features, atraumatic, with anicteric sclera, and patent nares and oropharynx. There was no cyanosis or clubbing and he spoke easily without effort. He had normal chest symmetry and expansion during respiration. There was no edema of the extremities, and no abnormalities of the skin.

He was awake, alert, and pleasant, but unable to cooperate fully with the examination without visual prompting. His speech was fluent but nonsensical, with receptive errors and only partial understanding of posed questions. His pupils were equal, round, and reactive to light. His gaze was conjugate and unrestricted, without phoria or tropia. His face was symmetrical at rest and with expression. There was no dysarthria, hoarseness, or difficulty handling secretions. There was no pronator drift and he had full and symmetrical strength in the upper and lower extremities.

Brain MRI was obtained at 3T (750W, GE Healthcare, Milwaukee, Wisconsin) with standard protocol sequences, including T1, T2, fluid-attenuated inversion recovery (FLAIR), proton density (PD), diffusion-weighted imaging (DWI), and ASL. The ASL sequence used pseudo-continuous arterial spin labeling (pCASL)⁶ with inversion (tagging) pulses immediately inferior to the imaging volume. Background suppression pulses were applied to reduce the signal of stationary tissues^{7, 8, 9} and improve signal-to-noise ratio of arterial blood. The imaging volume was obtained with a 3D fast spin echo (3D FSE). Quantitative cerebral blood flow (CBF)

maps were derived from raw ASL data using PD maps and a single-compartment perfusion model^{10, 11, 12}. CBF measurements were taken in regions of interest (ROI) within gray matter near the vertices.

No acute infarction or edema was found on DWI or FLAIR, as shown in Figure 1 Parts A and B, respectively. A quantitative cerebral blood flow map derived from ASL showed reduced left hemispheric perfusion (21 ± 7 ml/100 mg/min) compared with the contralateral side (62 ± 19 ml/100 mg/min), which was within normal limits (Figure 1C). Bolus perfusion DCE imaging confirmed the asymmetric perfusion deficit (Figure 1D). The Circle of Willis and large caliber cerebral arteries were patent on MRI (Figure 2A) and CT (Figure 2B) angiography, without evidence of occlusion or vasospasm to explain reduced perfusion in the left hemisphere. An echocardiogram was normal and electroencephalography (EEG) demonstrated left posterior temporal slowing, but no seizures.

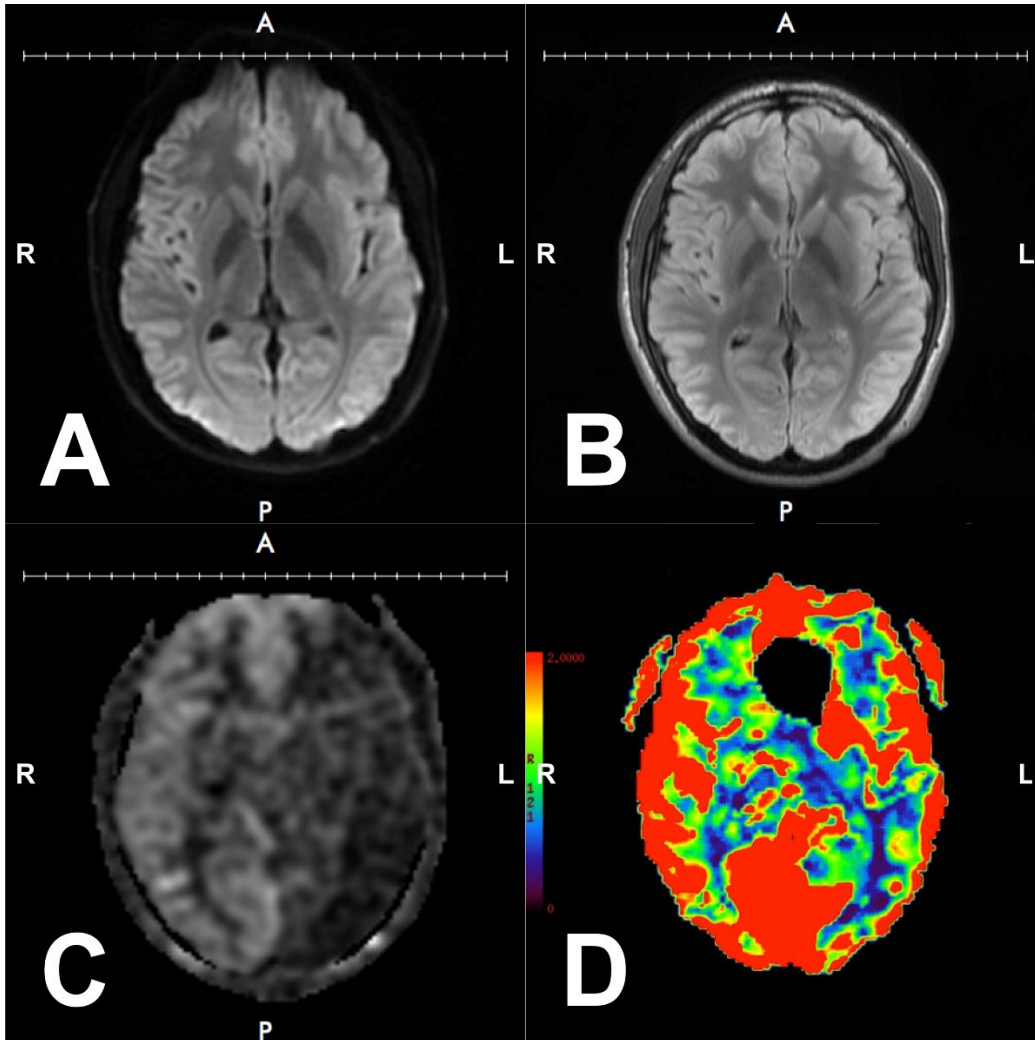


Figure 3. Cerebral MRI data from day of symptom onset. (A) DWI imaging showed no acute infraction; (B) FLAIR demonstrated no signal abnormalities indicative of edema; (C) ASL showed decreased cerebral perfusion on the left hemisphere with normal perfusion on the right hemisphere; (D) DCE bolus imaging confirmed asymmetric perfusion observed in ASL.

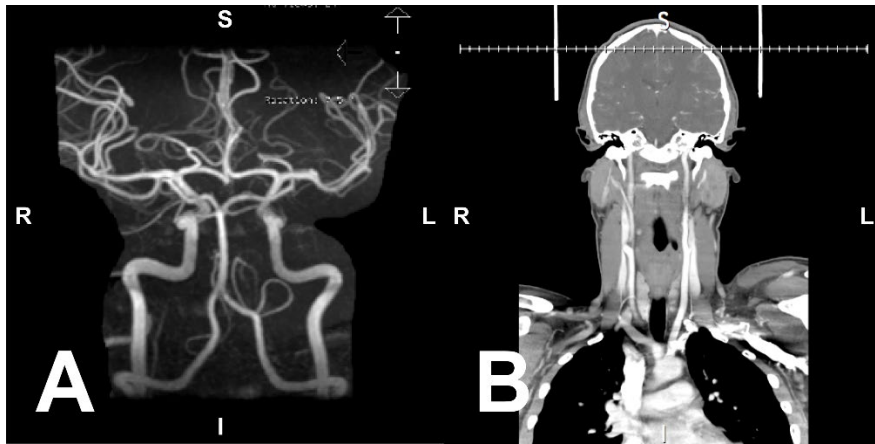


Figure 4. Angiography from day of symptom onset showed enlarged cerebral arteries without evidence of occlusion nor vasospasm in MRA (A) and CT (B) imaging modalities.

During examination the following morning, the patient was awake, alert, appropriately conversant, pleasant and cooperative. His speech was fluent, comprehension was intact, and he had full and symmetric strength in the upper and lower extremities. A repeat brain MRI displayed complete resolution of the perfusion abnormality without evidence of an infarction, as observed in Figure 3. Cerebral blood flow calculated by ASL was 67 ± 10 ml/100 mg/min in the left hemisphere and 63 ± 12 ml/100 mg/min in the right hemisphere.

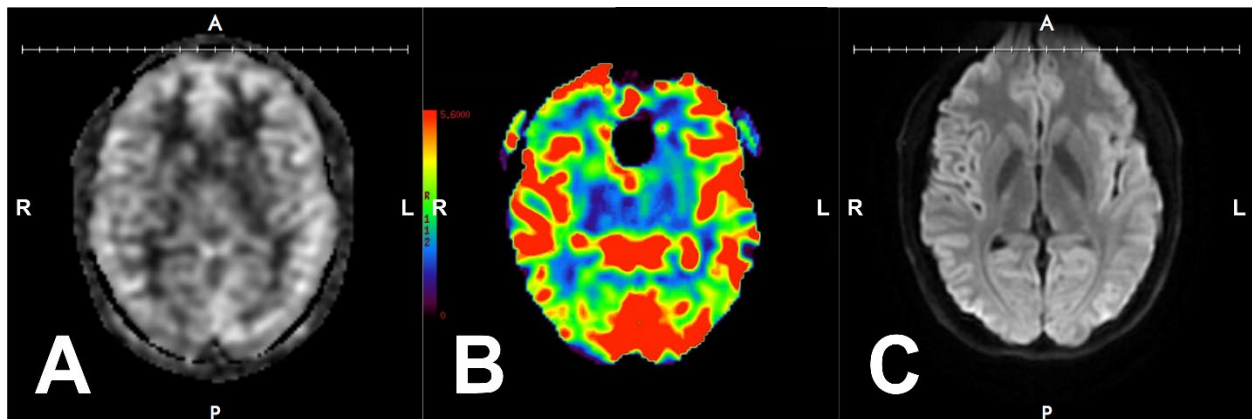


Figure 5. Cerebral MRI data one day after symptom onset. (A) ASL and (B) DCE imaging showed complete resolution of observed left hemisphere perfusion abnormality while (C) DWI demonstrated the absence of infraction.

The patient was discharged home and resumed participation in school and sports activities. A follow-up EEG was performed two weeks later and was normal. Repeat imaging at three months and again at almost 18 months confirmed his cerebral perfusion remained normal. At 18

months after the incident he was doing well, although he reported one transient episode of poor responsiveness when his blood glucose was ~40 mg/dL, with resolution of symptoms after drinking some juice. He continued to participate in school and athletic activities.

Discussion

This is a case of acute onset encephalopathy with receptive aphasia in a patient with insulin-dependent diabetes mellitus and a history of transient episodes of altered mental status with hypoglycemia. Although we did not have direct laboratory evidence at the time of his deficit, the reversible nature of his condition suggests that his symptoms were a result of transient hypoglycemia, which can cause focal neurologic deficits with or without seizures^{13, 14}. In his case, a prolonged reversible neurologic deficit was accompanied by hemispheric hypoperfusion confirmed by both ASL and DCE perfusion techniques.

Seizure with postictal cerebral dysfunction may be associated with altered cerebral flow detected with ASL¹⁵. Migraine attacks may also be associated with hypoperfusion during an aura phase, followed by hyperperfusion after the onset of a headache^{16, 17}. A recent study on ASL perfusion in children with atypical aura demonstrated regional cerebral hypoperfusion in most cases, associated with minor cerebral vasospasm on time-of-flight MRA¹⁸. One case report of hemiplegic migraine studied with ASL demonstrated single hemispheric hypoperfusion with subtle narrowing of the corresponding middle cerebral artery¹⁹. These pathologic processes remain in the differential diagnosis, although this patient had no clinical or electrographic evidence of seizures, and no clinical history of complex migraines.

Apparent hypoperfusion may occur in cases of normal CBF with proximal vessel occlusion, resulting from underestimation in standard ASL sequences that use a single delay between labeling and image acquisition, a phenomenon known as “arterial transit artifact²⁰.” In this case, both CT and MRI angiography showed no evidence of large vessel occlusion indicative of an arterial transit artifact, and hemispheric hypoperfusion was confirmed with DCE. Additionally, the reversible nature of the perfusion abnormality coupled with his neurologic deficit are not suggestive of technical artifact.

Cerebral perfusion and metabolism are tightly coupled since energy demands during brain activity are met largely through oxidative metabolism²¹. Hypoglycemia may cause increased CBF with redistribution of blood flow to specific sites from an autonomic stress

response²². There are previous reports of transient hypoglycemia mimicking acute stroke with reversible restricted diffusion and hyperperfusion²³, in addition to cases of hypoglycemic hemiplegia associated with hypoperfusion²⁴. Animal models of hypoglycemia provide evidence for both hypoglycemia-related hyperperfusion and subsequent delayed hypoperfusion²⁵. Future studies on the mechanism of this phenomenon should consider hypoglycemic effects on cerebral metabolism.

In this case, ASL was a valuable technique used to quantify perfusion for a pediatric patient. ASL provided non-invasive perfusion imaging data that rivals similar information obtained through xenon-133, single-photon emission computed tomography (SPECT), and DCE perfusion techniques. ASL is a convenient and safe MRI sequence that provides reliable quantitative data critical for the differential diagnosis of acute onset neurologic deficits in children.

References

- [1] Mackay MT, Yock-Corrales A, Churilov L, Monagle P, Donnan GA, Babl FE. Accuracy and Reliability of Stroke Diagnosis in the Pediatric Emergency Department. *Stroke* 2017;48(5):1198–202. Available at: <http://dx.doi.org/10.1161/STROKEAHA.116.015571>
- [2] Vilela P, Rowley HA. Brain ischemia: CT and MRI techniques in acute ischemic stroke. *European Journal of Radiology* 2017;96:162–72. Available at: <http://dx.doi.org/10.1016/j.ejrad.2017.08.014>
- [3] Wang J, Licht DJ. Pediatric Perfusion MR Imaging Using Arterial Spin Labeling. *Neuroimaging Clinics of North America* 2006;16(1):149–67. Available at: <http://dx.doi.org/10.1016/j.nic.2005.10.002>
- [4] Telischak NA, Detre JA, Zaharchuk G. Arterial spin labeling MRI: Clinical applications in the brain. *Journal of Magnetic Resonance Imaging* 2014;41(5):1165–80. Available at: <http://dx.doi.org/10.1002/jmri.24751>
- [5] Chen J, Licht DJ, Smith SE, et al. Arterial spin labeling perfusion MRI in pediatric arterial ischemic stroke: Initial experiences. *Journal of Magnetic Resonance Imaging* 2009;29(2):282–90. Available at: <http://dx.doi.org/10.1002/jmri.21641>
- [6] Silvia AC, Kim SG. Pseudo-continuous arterial spin labeling technique for measuring CBF dynamics with high temporal resolution. *Magnetic Resonance in Medicine* 1999;42(3):425-9. Available at: [http://dx.doi.org/10.1002/\(SICI\)1522-2594\(199909\)42:3<425::AID-MRM3>3.0.CO;2-S](http://dx.doi.org/10.1002/(SICI)1522-2594(199909)42:3<425::AID-MRM3>3.0.CO;2-S)
- [7] Mani S, Pauly J, Conolly S, Meyer C, Nishimura D. Background suppression with multiple inversion recovery nulling: Applications to projective angiography. *Magnetic Resonance in Medicine* 1997;37(6):898–905. Available at: <http://dx.doi.org/10.1002/mrm.1910370615>
- [8] Dixon WT, Sardashti M, Castillo M, Stomp GP. Multiple inversion recovery reduces static tissue signal in angiograms. *Magnetic Resonance in Medicine* 1991;18(2):257–68. Available at: <http://dx.doi.org/10.1002/mrm.1910180202>

- [9] Ye FQ, Frank JA, Weinberger DR, McLaughlin AC. Noise reduction in 3D perfusion imaging by attenuating the static signal in arterial spin tagging (ASSIST). *Magnetic Resonance in Medicine* 2000;44(1): 92–100. Available at: [http://dx.doi.org/10.1002/1522-2594\(200007\)44:1<92::AID-MRM14>3.0.CO;2-M](http://dx.doi.org/10.1002/1522-2594(200007)44:1<92::AID-MRM14>3.0.CO;2-M)
- [10] Mutsaerts HJMM, Steketee RME, Heijtel DFR, et al. Inter-Vendor Reproducibility of Pseudo-Continuous Arterial Spin Labeling at 3 Tesla. *PLoS ONE* 2014;9(8):e104108. Available at: <http://dx.doi.org/10.1371/journal.pone.0104108>
- [11] Alsop DC, Detre JA, Golay X, et al. Recommended implementation of arterial spin-labeled perfusion MRI for clinical applications: A consensus of the ISMRM perfusion study group and the European consortium for ASL in dementia. *Magnetic Resonance in Medicine* 2014;73(1):102–16. Available at: <http://dx.doi.org/10.1002/mrm.25197>
- [12] Alsop DC, Detre JA. Reduced transit-time sensitivity in noninvasive magnetic resonance imaging of human cerebral blood flow. *Journal of Cerebral Blood Flow Metabolism* 1996; 16(6):1236-49. Available at: <http://dx.doi.org/10.1097/00004647-199611000-00019>
- [13] Pocecco M, Ronfani L. Transient focal neurologic deficits associated with hypoglycaemia in children with insulin-dependent diabetes mellitus. *Acta Paediatrica* 1998;87(5):542–4. Available at: <http://dx.doi.org/10.1111/j.1651-2227.1998.tb01500.x>
- [14] Wattoo MA, Liu HH. Alternating transient dense hemiplegia due to episodes of hypoglycemia. *Western Journal of Medicine*. 1999;170(3):170-171. Available at: <http://dx.doi.org/10.1097/00004647-199611000-00019>
- [15] Gaxiola-Valdez I, Singh S, Perera T, Sandy S, Li E, Federico P. Seizure onset zone localization using postictal hypoperfusion detected by arterial spin labelling MRI. *Brain* 2017;140(11):2895–911. Available at: <http://dx.doi.org/10.1093/brain/awx241>
- [16] Olesen J, Larsen B, Lauritzen M. Focal hyperemia followed by spreading oligemia and impaired activation of rcbf in classic migraine. *Annals of Neurology* 1981;9(4):344–52. Available at: <http://dx.doi.org/10.1002/ana.410090406>
- [17] Olesen J, Friberg L, Olsen TS, et al. Timing and topography of cerebral blood flow, aura, and headache during migraine attacks. *Annals of Neurology* 1990;28(6):791–8. Available at: <http://dx.doi.org/10.1002/ana.410280610>

- [18] Cadiot D, Longuet R, Bruneau B, et al. Magnetic resonance imaging in children presenting migraine with aura: Association of hypoperfusion detected by arterial spin labelling and vasospasm on MR angiography findings. *Cephalalgia* 2017;033310241772357. Available at: <http://dx.doi.org/10.1177/0333102417723570>
- [19] Bosemani T, Burton VJ, Felling RJ, et al. Pediatric hemiplegic migraine: Role of multiple MRI techniques in evaluation of reversible hypoperfusion. *Cephalalgia* 2013;34(4):311–5. Available at: <http://dx.doi.org/10.1177/0333102413509432>
- [20] Haller S, Zaharchuk G, Thomas DL, Lovbald KO, Barkhof F, Golay X. Arterial Spin Labeling Perfusion of the Brain: Emerging Clinical Applications. *Radiology* 2016;281(2):337-356. Available at: <http://dx.doi.org/10.1148/radiol.2016150789>
- [21] Hoge RD, Atkinson J, Gill B, Crelier GR, Marrett S, Pike GB. Linear coupling between cerebral blood flow and oxygen consumption in activated human cortex. *Proceedings of the National Academy of Sciences* 1999;96(16):9403–8. Available at: <http://dx.doi.org/10.1073/pnas.96.16.9403>
- [22] Wiegers EC, Becker KM, Rooijackers HM, et al. Cerebral blood flow response to hypoglycemia is altered in patients with type 1 diabetes and impaired awareness of hypoglycemia. *Journal of Cerebral Blood Flow & Metabolism* 2016;37(6):1994–2001. Available at: <http://dx.doi.org/10.1177/0271678x16658914>
- [23] Cordonnier C, Oppenheim C, Lamy C, Meder J-F, Mas J-L. Serial diffusion and perfusion-weighted MR in transient hypoglycemia. *Neurology* 2005;65(1):175–175. Available at: <http://dx.doi.org/10.1212/01.wnl.0000167128.14769.7b>
- [24] 24. Shintani S, Tsuruoka S, Shiigai T. Hypoglycaemic hemiplegia: a repeat SPECT study. *Journal of Neurology, Neurosurgery & Psychiatry* 1993;56(6):700–1. Available at: <http://dx.doi.org/10.1136/jnnp.56.6.700>
- [25] Abdul-Rahman A, Agardh CD, Siesjø BK. Local cerebral blood flow in the rat during severe hypoglycemia, and in the recovery period following glucose injection. *Acta Physiologica Scandinavica* 1980;109(3):307–14. Available at: <http://dx.doi.org/10.1111/j.1748-1716.1980.tb06601.x>

CHAPTER THREE: BIOPSY SELECTION

Variation in correlation between prognosis and histologic feature based on biopsy selection

Glioblastoma multiform carries a dismal prognosis with poor response to gold standard treatment¹. Innovative data analysis methods have been developed to characterize tumor genomic expression with histologic features. In a clinical setting, biopsy selection methods may be constrained by time and burden to the patient. Thus, we investigate the impact of biopsy selection on correlation between prognostic and histologic features in 35 patients with GBM. We compared methods using limited volumes, moderate volumes, and enblock tumor volumes. Additionally, we investigated the impact of random versus strategic methods for limited and moderate volume biopsies. Finally, we compared correlation results by selecting one to five small biopsy. We observed a wide range in correlation significance across selection methods. These findings may aid clinical management of GBM and direct better biopsy selection necessary for the development and deployment of targeted therapies.

Introduction

Glioblastoma multiform (GBM) is the most common and worst form of glioma in terms of therapeutic response, aggressiveness, and prognosis¹⁻³. The treatment gold standard for GBM includes surgical resection, chemotherapy, and radiotherapy, which is invasive, has unwanted side effects, and can have a large negative impact on quality of life¹. Even with the efforts of gold standard treatment, tumor recurrence incidence is higher in GBM compared to other neoplasms⁴. Thus, efforts have been made to characterize the molecular and genetic profile within GBM so targeted therapeutic methods could be used with a more effective clinical approach^{5,6}.

Recently, Ivy Glioblastoma Atlas Project (Ivy GAP) initiated a several studies to evaluate genetic expression associated with histologic and clinical features^{7,8}. Cantanhede and Oliveira observed that within histologic features there are significant variations between platelet derived growth factor (PDGR) family genes. Additionally, they found significant differences in expression between left and right lobes. Similarly, Puchalski et al observed that RNA-seq had significant variation across histologic structural features defined as cellular tumor, leading edge,

palisading necrosis, and microvascular proliferation. These works demonstrate with statistical confidence a link between histologic structural features and genetic expression.

In a clinical setting, the diagnostic gold standard is medical imaging, preferably magnetic resonance imaging (MRI), followed by biopsy confirmation^{9,10}. Biopsy tissue volume may vary across cases from needle biopsy to biopsy sectioning during resection. In either case, the tissue sampling is likely less than the average volume per patient, 7 cm³, used by Ivy GAP. Since a GBM hallmark is intratumor heterogeneity, we hypothesized that biopsy features would vary greatly between methods.

Methods

Data selection.

Histologic features, clinical and genomic data for 35 of 41 available GBM patients was retrospective obtained from the Ivy GAP repository (Allen Institute for Brain Science. Ivy Glioblastoma Atlas Project. Available from: <https://glioblastoma.alleninstitute.org/>). The cohort was selected based on the following inclusion criteria: enbloc resection contains at least three sub blocks; and complete prognosis data. Histologic feature data was acquired from Ivy GAP (Allen Institute for Brain Science. Ivy Glioblastoma Atlas Project. Available from: <https://glioblastoma.alleninstitute.org/static/download.html>). The histologic features defined by Ivy GAP are: leading edge (LE); hyperplastic blood vessels in leading edge (LEhbv); infiltrating tumor (IT); hyperplastic blood vessels in infiltrating tumor (IThbv); cellular tumor (CT); perinecrotic zone (CTpnz); psuedopalising cells but no visible necrosis (CTpnn); pseudopalising cells around necrosis (CTpan); hyperplastic blood vesselsin cellular tumor (CThbv); microvascular proliferation (CTmvp); and necrosis (CTne). Figure 4 depicts an annotated slide. Histologic features were normalized to the total H&E tissue area for each slide. Clinical and genomic data was acquired from Ivy GAP (Allen Institute for Brain Science. Ivy Glioblastoma Atlas Project. Available from: <https://glioblastoma.alleninstitute.org/static/download.html>) and tabulated for the selected cohort.

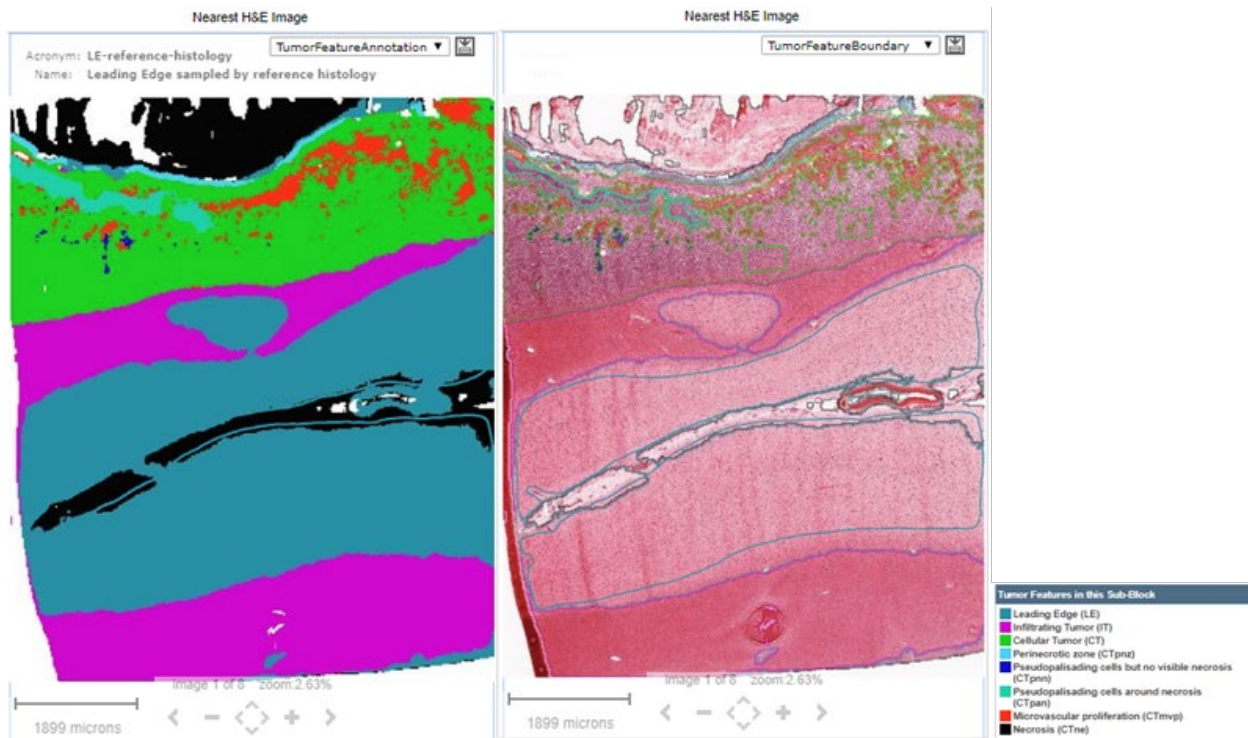


Figure 6. An example of slide annotation from IvyGAP. The tumor feature annotation (left), the annotation boundary on hematoxylin and eosin slide (center), and the tumor feature legend (right).

Data analysis.

From the compiled data, we analyzed seven biopsy selection methods in MATLAB R2018b (www.mathworks.com). Three location methods (random, tumor center, and max necrosis) were applied to two volume methods (slide and block), resulting in the following six combinations: (A) randomly select one slide; (B) randomly select one block average; (C) one slide at tumor centroid; (D) one block average at tumor centroid; (E) one slide at necrosis; and (F) one block average at necrosis. We selected slide and block volumes to represent needle biopsy (NB) and surgical biopsy (SB) volumes respectively. The last method was (G) the enbloc average, representing the max tissue volume of data available for a patient. For methods C and E, if the location of interest contained more than one slide, a slide was chosen at random. For methods B, D, and F all the slides from the corresponding block were averaged together. For biopsy number analysis, we randomly selected one to five slides from unique block locations across each tumor. Correlation between un-censored, continuous variables overall survival (OS), progression free

survival (PFS) and histologic features were evaluated by Pearson's correlation. Correlations were considered statistically significant if p value < 0.10 .

Results

Clinical and genomic data for cohort.

Information from the compiled data as summarized in Table 1 reveals that the cohort has a young age at the time of diagnosis and comparable gender distribution. For gross primary tumor locations, the right frontal lobe has the highest incident, followed by left parietal and mixed right hemisphere. The cohort has high functioning Karnofsky Performance Status (KPS), with nearly half presenting neurologic defect, indicating mildly impaired quality of life and favorable prognosis (10,11,12). However, as common with GBM, the prognostic outcomes for the cohort are poor with median progression free survival (PFS) of 107 days, and median overall survival (OS) of 439 days. For genomic expression, Isocitrate Dehydrogenase 1 (IDH1) mutation is observed in three patients, consistent with the literature.

Table 1. Clinical and genomic data for research cohort. PTEN: Phosphatase and Tensin Homolog; IDH1: Isocitrate Dehydrogenase 1; MGMT: O-6-Methylguanine-DNA Methyltransferase; PCR: Polymerase chain reaction.

Clinical Data			Genomic Data		
Gender			PTEN		
Female	N=17	48.57%	Deletion/Loss	N=18	51.43%
Male	N=18	51.43%	Gain	N=3	8.57%
Age At Diagnosis (years)			Normal	N=3	8.57%
Mean \pm standard deviation	58.7 \pm 12.0		IDH1		
Median	61		Wild-type	N=30	85.71%
Karnofsky Performance Status			Mutated	N=3	8.57%
Mean \pm standard deviation	88 \pm 10.5		1p19q Deletion		
>70	N=29	82.86%	Positive	N=3	8.57%
\leq 70	N=6	17.14%	Negative/Normal	N=21	60.00%
History of Seizure			MGMT PCR		
Present	N=10	28.57%	Methylated	N=6	17.14%
Not-present	N=25	71.43%	Unmethylated	N=19	54.29%
Neurologic defect					
Present	N=16	45.71%			
Not-present	N=19	54.29%			
Primary Tumor Location					
Left frontal	N=1	2.86%			
Left Occipital	N=1	2.86%			
Left Parietal	N=6	17.14%			
Left Temporal	N=5	14.29%			
Right Frontal	N=7	20.00%			
Right Parietal	N=4	11.43%			
Right Temporal	N=5	14.29%			
Mixed Right Hemisphere	N=6	17.14%			
Progression free survival (days)					
Mean \pm standard deviation	205.5 \pm 256.8				
Median	107				
Overall survival (days)					
Mean \pm standard deviation	491.4 \pm 321.5				
Median	439.5				

Correlation between overall survival and histologic feature vary by biopsy method.

Correlation significance between overall survival (OS) and LE, IT, CTpzn, CTpnn, CTmvp, CTne vary by biopsy method as shown in Figure 5. The correlation between OS and LE is significant for NB methods taken at random and at max necrosis (p=0.05, and p=0.09 respectively). For IT, correlation with OS is significant for NB method taken from max necrosis (p=0.08). The correlation between CTpzn and OS is significant for NB methods taken at random and from max necrosis (p=0.05 and 0.07 respectively). For CTpnn, the correlation is significant

for SB methods taken at random and at tumor centroid ($p=0.008$, 0.02 respectively), while for NB method it is significant taken from tumor center ($p=0.002$). Histologic feature CTmvp has significant correlation with OS for SB methods taken at max necrosis and enblock ($p=0.06$, and 0.006 respectively). For OS and CTne SB at max necrosis has significant correlation ($p=0.04$). The correlation between OS and NB, SB, and enbloc is shown in Figure 5 A, C, and E respectively.

Correlation between progression free survival and histologic feature vary by biopsy method.

The correlation between progression free survival (PFS) and histologic features CTpnn and CTmvp vary based on biopsy method as shown in Figure 5. For SB based methods, the correlation between PFS and CTpnn is significant if the biopsy is taken from the center ($p=0.007$). The correlation between PFS and CTmvp is significant if NB biopsy from the tumor center or SB from random is used ($p=0.03$, and $p=0.035$ respectively). The correlation between PFS and NB, SB, and enbloc is shown in Figure 5 B, D, and E respectively.

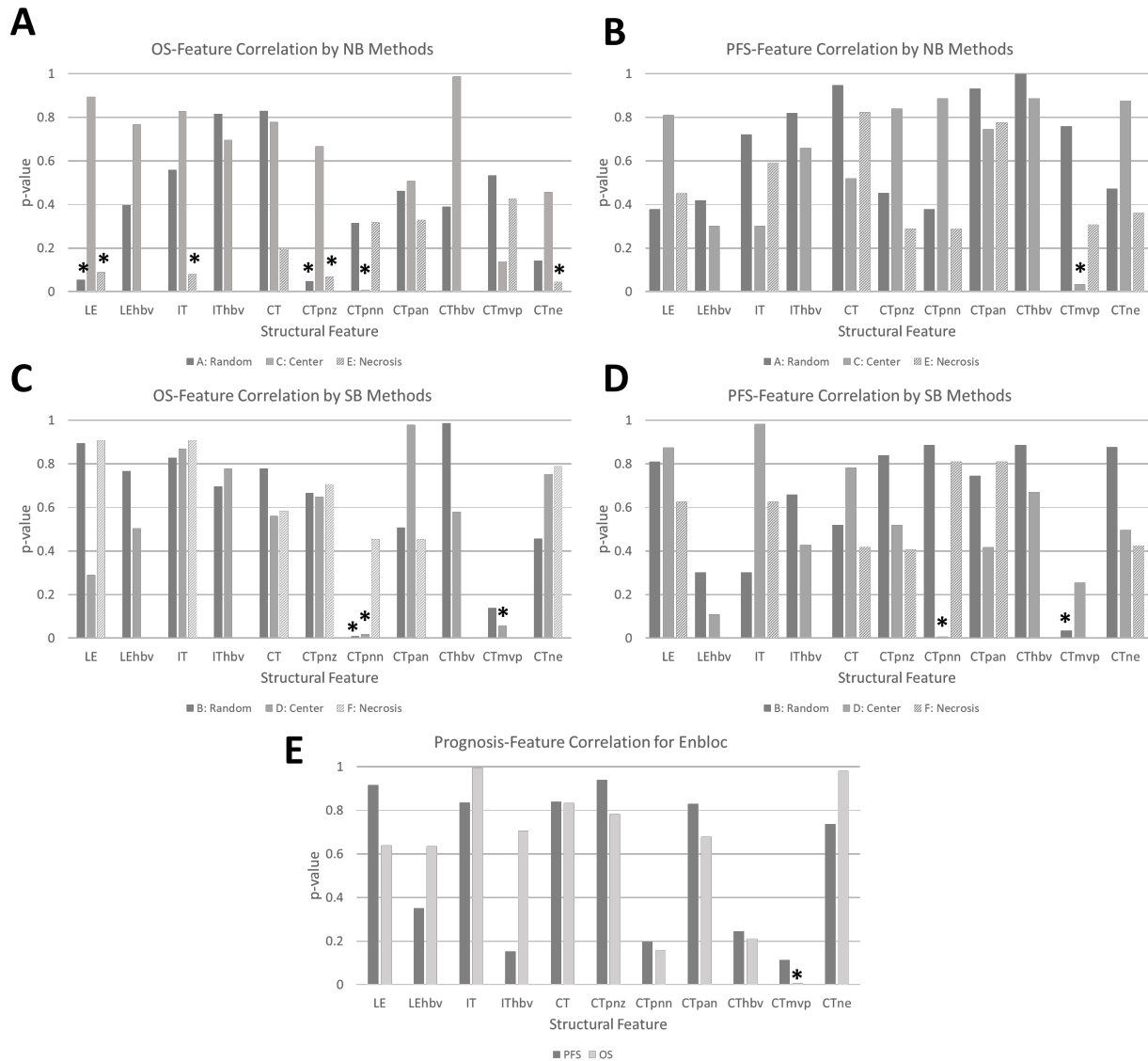


Figure 7. Correlation between prognosis and structural features across biopsy methods. (A) Correlation between overall survival (OS) and histology structural features by limited volume, needle biopsy (NB) like methods. (B) Correlation between progression free survival (PFS) and histology structural features by limited volume, needle biopsy (NB) like methods. (C) Overall survival (OS) correlation to histologic structural features using a larger volume, surgical biopsy (SB) like methods. (D) Progression free survival (PFS) correlation to histologic structural features using a larger volume, surgical biopsy (SB) like methods. (E) Correlation between prognostic factors and histologic structural features using enblock method.

Correlation between prognosis and histologic feature vary by the number of biopsies selected.

For correlation between PFS and histologic feature CTpnz ($p=0.036$) there was significant variation from the number of biopsies. For correlation between OS and histologic features LE

($p=0.026$), LEhbv ($p=0.011$), and CTmvp ($p=0.003$) there was significant variation from the number of biopsies. Variation in correlation between prognosis and histologic features due to the number of biopsies can be observed in Figure 6.

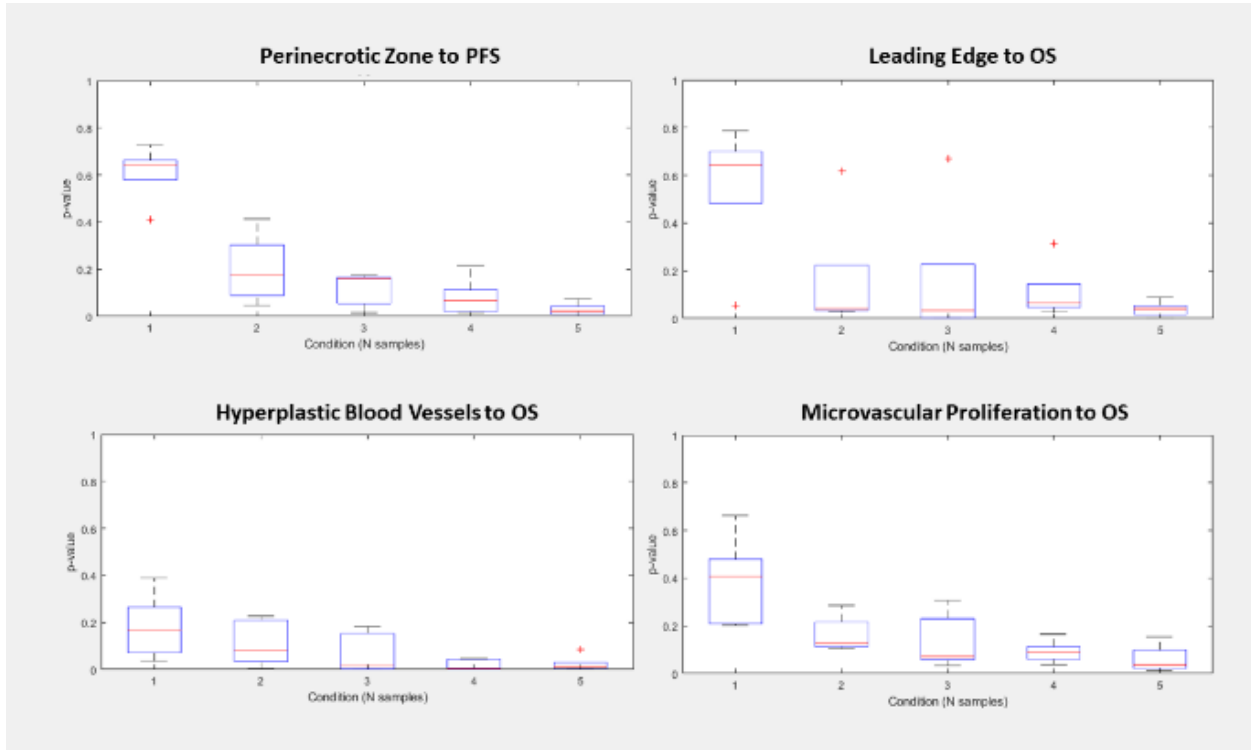


Figure 8. Variation in correlation between prognosis and histology based on the number of biopsies taken. PFS: progression free survival; OS: overall survival.

Discussion

This study presents the impact of biopsy selection method on correlation between prognosis and histologic features. The impact of intra-tumoral heterogeneity can be observed in the correlation range by method. Between needle like biopsy, surgical biopsy, and enblock analysis, correlation with prognosis varies greatly.

GBM has been studied widely, however to our knowledge, this is the first study to look at the effects of sampling technique from in-vivo data. Repositories, such as The Cancer Genome Atlas (TCGA) have clinical, genomic, and biopsy data, however the location of biopsy relative to the tumor is unknown¹¹. Additionally, the biopsies volume used to derive histologic features characteristic of GBM, such as the presence of necrosis or palisading tumor, is unknown^{12,13}.

However, multiple studies have linked, or argue such, that a relationship between histologic features and genomic expression and/or imaging features are reliable ^{14,15}.

Based on this analysis, we can observe vast variation in correlation between limited volume biopsies, such as needle biopsy. Between one and three samples there is a wide shift in correlation, consistent with intra-tumoral heterogeneity¹⁶⁻²⁰. Additionally, a plateau is observed in limited volume biopsies between three and five samples, this appears consistent with the observation between random, tumor center, and necrotic core for limited volume biopsy. However, when moving to mid volume or max volume observed, methods B, D, F, and G, few correlations between OS or PFS and histologic features are significant. This appears to represent a “wash-out” like effect, where the heterogeneity across the tumor is no longer observed. Considering the presented data, select limited volume biopsy, such as needle biopsy, across the tumor has the most robust correlation with prognostic factors OS and PFS. Clinically, these methods may be applied to robustly capture histologic features consistent with GBM. Three to five limited volume biopsies taken from the tumor center, max necrosis, and randomly at a minimum of 1 cm separation results in strong correlation to prognostic features.

References

- [1] Fernandes C, Costa A, Osório L, et al. Current Standards of Care in Glioblastoma Therapy. In: De Vleeschouwer S, editor. Glioblastoma. Brisbane (AU): Codon Publications; 2017 Sep 27. Chapter 11. doi: 10.15586/codon.glioblastoma.2017.ch1
- [2] Barnholtz-Sloan JS, Ostrom QT, Cote D. Epidemiology of Brain Tumors. *Neurol Clin.* 2018;36(3):395-419. doi:10.1016/j.ncl.2018.04.001
- [3] Louis N, Perry A, Reifenberge RG, von Deimling A, Figarella-Branger D, Cavenee WK, et al. The 2016 World Health Organization classification of tumors of the central nervous system: A summary. *Acta Neuropathol.* 2016;131:803–20.
- [4] Urbanska, K., Sokolowska, J., Szmidt, M. & Sysa, P. Glioblastoma multiforme - An overview. *Wspolczesna Onkol.* 18, 307–312 (2014).
- [5] Omuro, A. & LM, D. Glioblastoma and other malignant gliomas: A clinical review. *JAMA* 310, 1842–1850 (2013).
- [6] Vitucci, M., Hayes, D. N. & Miller, C. R. Gene expression profiling of gliomas: merging genomic and histopathological classification for personalised therapy. *Br. J. Cancer* 104, 545–553 (2011).
- [7] Puchalski, R., Shah, N., Miller, J., et al. An anatomic transcriptional atlas of human glioblastoma. *Science* 360, 660-663 (2018).
- [8] Cantanhede, I., and de Oliveira, J. PDGF Family Expression in Glioblastoma Multiforme: Data Compilation from Ivy Glioblastoma Atlas Project Database. *Scientific Reports* 7. (2017).
- [9] Ellingson, Benjamin M et al. Consensus recommendations for a standardized Brain Tumor Imaging Protocol in clinical trials. *Neuro-oncology.* 2015;17(9):1188-98. doi:10.1093/neuonc/nov095
- [10] Lombardi MY, Assem M. Glioblastoma Genomics: A Very Complicated Story. Glioblastoma. Brisbane (AU): Codon Publications; 2017 Sep 27. doi: 10.15586/codon.glioblastoma.2017.ch1
- [11] The cancer genome atlas research network. Comprehensive, integrative genomic analysis of diffuse lower-grade gliomas. *The New England Journal of Medicine* 2015;372:2481-2498. doi: 10.1056/NEJMoa1402121

- [12] Liu, S., Wang, Y., Xu, K., Wang, Z., Fan, X., Zhang, C., Li, S., Qiu, X., and Jiang, T. Relationship between necrotic patterns in glioblastoma and patient survival: fractal dimension and lacunarity analyses using magnetic resonance imaging. *Scientific Reports* 7. (2017).
- [13] Raza, S.M., Lang, F.F., Aggarwal, B.B., Fuller, G.N., Wildrick, D.M., and Sawaya, R. Necrosis and Glioblastoma: A Friend or a Foe? A Review and a Hypothesis. *Neurosurgery* 51, 2–13. (2002).
- [14] Belden, C.J., Valdes, P.A., Ran, C., Pastel, D.A., Harris, B.T., Fadul, C.E., Israel, M.A., Paulsen, K., and Roberts, D.W. Genetics of Glioblastoma: A Window into Its Imaging and Histopathologic Variability. *RadioGraphics* 31, 1717–1740. (2011).
- [15] Barajas, R.F., Hodgson, J.G., Chang, J.S., Vandenberg, S.R., Yeh, R.-F., Parsa, A.T., McDermott, M.W., Berger, M.S., Dillon, W.P., and Cha, S. Glioblastoma Multiforme Regional Genetic and Cellular Expression Patterns: Influence on Anatomic and Physiologic MR Imaging. *Radiology* 254, 564–576. (2010).
- [16] Louis N, Perry A, Reifenberge RG, von Deimling A, Figarella-Branger D, Cavenee WK, et al. The 2016 World Health Organization classification of tumors of the central nervous system: A summary. *Acta Neuropathol.* 2016;131:803–20.
- [17] Ohgaki H, Kleihues P. The definition of primary and secondary glioblastoma. *Clin Cancer Res.* 2013;19:764–72.
- [18] Ohgaki H, Dessen P, Jourde B, Horstmann S, Nishikawa T, Di Patre PL, et al. Genetic pathways to glioblastoma: A population-based study. *Cancer Res.* 2004;64:6892–9.
- [19] Assem M, Sibenaller Z, Agarwal S, Al-Keilani MS, Alqudah MAY, Ryken TC. Enhancing diagnosis, prognosis and therapeutic outcome prediction of gliomas using genomics. *OMICS.* 2012;16(3):113–22
- [20] Kleihues P, Ohgaki H. Primary and secondary glioblastomas: From concept to clinical diagnosis. *Neuro Oncol.* 1999;1:44–51.

CHAPTER FOUR: VOXEL-WISE RADIOMIC MODELS

Predicted disease compositions of human gliomas estimated from multiparametric MRI can predict endothelial proliferation, tumor grade, and overall survival

Biopsy is the main determinants of glioma clinical management, but require invasive sampling that fail to detect relevant features because of tumor heterogeneity. The purpose of this study was to evaluate the accuracy of a voxel-wise, multiparametric MRI radiomic method to predict features and develop a minimally invasive method to objectively assess neoplasms. Multiparametric MRI were registered to T1-weighted gadolinium contrast-enhanced data using a 12 degree-of-freedom affine model. The retrospectively collected MRI data included T1-weighted, T1-weighted gadolinium contrast-enhanced, T2-weighted, fluid attenuated inversion recovery, and multi-b-value diffusion-weighted acquired at 1.5T or 3.0T. Clinical experts provided voxel-wise annotations for five disease states on a subset of patients to establish a training feature vector of 611,930 observations. Then, a k-nearest-neighbor (k-NN) classifier was trained using a 25% hold-out design. The trained k-NN model was applied to 13,018,171 observations from seventeen histologically confirmed glioma patients. Linear regression tested overall survival's (OS) relationship to predicted disease compositions (PDC) and diagnostic age ($\alpha = 0.05$). Canonical discriminant analysis tested if PDC and diagnostic age could differentiate clinical, genetic, and microscopic factors ($\alpha = 0.05$). The model predicted voxel annotation class with a Dice similarity coefficient of $94.34\% \pm 2.98$. Linear combinations of PDCs and diagnostic age predicted OS ($p = 0.008$), grade ($p = 0.014$), and endothelia proliferation ($p = 0.003$); but fell short predicting gene mutations for TP53BP1 and IDH1. This voxel-wise, multi-parametric MRI radiomic strategy holds potential as a non-invasive decision-making aid for clinicians managing patients with glioma.

Introduction

Every year more than 6 per 100,000 adults in the United States are diagnosed with glioma, the most common malignant tumor of the central nervous system.¹ For clinical purposes, the World Health Organization (WHO) grades gliomas I to IV, based on histologic and molecular features, with the worst survival associated with glioblastoma, WHO grade IV, in which only one half of

patients survive one year after diagnosis.² Lower grade gliomas (LGG), as defined by The Cancer Genome Atlas (TCGA), include WHO grades II and III gliomas and have a survival range of one to fifteen years.³ Grading informs various treatment protocols including resection, chemotherapy, radiation therapy, and long-term monitoring. Unfortunately, complete surgical resection may be infeasible, and both epigenetic characteristics and tumor heterogeneity may reduce sensitivity to chemotherapy and radiotherapy.²

The current standard for glioma diagnosis is histopathologic evaluation after resection or biopsy, with refinements in tumor classification based on molecular features. However, not all patients are candidates for surgery and, even with advancements in stereotaxic methods, the availability and quality of diagnostic tissue is constrained by procedure time, sampling error, and user interpretation.^{5,6} Therefore, alternative non-invasive methods must be developed to quantitatively investigate glioma phenotypic heterogeneity, which could alter clinical management strategies.

Magnetic resonance imaging (MRI) is a noninvasive imaging modality that provides critical information for glioma detection and diagnosis. Routine protocols usually include the qualitative imaging sequences T1-weighted (T1), gadolinium contrast-enhanced T1 (T1-GD), T2-weighted (T2), and fluid-attenuated inversion recovery (FLAIR).^{7,8} More advanced quantitative MRI sequences, such as diffusion-weighted imaging (DWI) and derived apparent diffusion coefficient (ADC) maps, have predictive potential for glioma differentiation.⁹ However, most studies focus on the power of a single MRI sequence, using measurement techniques that neglect heterogeneity.

Radiomics is a recently defined discipline of medical imaging that utilizes quantitative feature extraction and machine-learning models to develop clinically significant predictions.¹⁰ There have been many promising studies using radiomics principles for various cancers, often focused on anatomical locations such as breast, lung, and pancreas, with fewer focused on gliomas.¹¹⁻¹⁴ The Brain Tumor Segmentation (BraTS), developed by Bakas et al, is a collection of glioma annotations based on T1, T1-GD, T2, and FLAIR MRI data, recently applied to predict overall survival (OS) and progression free survival (PFS) based on radiomic features.¹⁵⁻¹⁷ Inano et al used diffusion tensor imaging (DTI) in a voxel-by-voxel (voxel-wise) method to develop k-means clusters that significantly differentiated WHO grade II from WHO grade III and IV gliomas.¹⁸ Tian et al used multiparametric MRI data from T1, T1-GD, T2, DWI, and arterial spin

labeling (ASL) sequences to define texture features that significantly differentiated glioma grades using a more complex and resource intensive support vector machine (SVM) model.¹⁹ However, the utilization of multiparametric MRI with a voxel-wise radiomics method for predicting glioma grade, genetic mutations, and prognosis has not been fully verified.

We hypothesized that a voxel-wise radiomics method using multiparametric MRI data could provide phenotypic classification reflecting general tumor heterogeneity (predicted disease compositions, PDC), with predictive utility for glioma grade and genetic mutations. We tested this with a non-parametric machine learning model employing k-nearest neighbor (k-NN) in a voxel-wise based feature vector across five MRI sequences from a publicly available data set (<http://www.iu.edu/~mip1>), with phenotype classifications defined by field experts.

Methods

Patient population

We obtained anonymized medical data for 28 patients with histologic diagnoses of LGG (N = 14) or glioblastoma multiforme (GBM, N = 14) from TCGA, in which WHO grade II and III glial tumors were designated as LGG.³ We excluded 11 patients: five for incomplete brain coverage, and six for motion or artefact. Therefore, we included 17 patients (10 LGG, 7 GBM; clinical characteristics summarized in Table 2).

Imaging Data

We obtained pre-intervention MRI data for all 17 patients from The Cancer Imaging Archive (TCIA). For each we selected five sequences in the axial plane: (1) T1; (2) T2; (3) FLAIR; (4) DWI; and (5) T1-GD. DWI data were processed into quantitative ADC maps using a custom script that solved the Stejskal-Tanner equation at each voxel.²⁰ The DWI sequences used two b values (0, and 1000 s/mm²) over two, four, or five directions for ten, one, and six patients, respectively. Due to the nature of the archive, field strength, manufacturer, and coil selection were inconsistent across patients. Table 3 summarizes the MRI parameters across respective sequences.

Table 2. Summary of clinical characteristics with Bonferroni corrected p-values.

	Lower Grade (LGG)	Glioblastoma (GBM)	p-value
Demographics			
Patients	58.8% (10/17)	41.2% (7/17)	N/A
Age at diagnosis, years (mean ± SD)	51.88 ±10.67	65.72 ±12.91	0.029
Gender			0.653
Male	60.0% (6/10)	71.4% (5/7)	
Female	40.0% (4/10)	28.6% (2/7)	
PFS, months (mean ± SD)	20.75 ±13.30	4.95 ±7.51	0.003*
OS, months (mean ± SD)	34.72 ±15.74	15.04 ±1.05	0.016*
Histologic subtype	Oligoastrocytoma WHO II, 40% (4/10) Oligodendroglioma WHO II, 20% (2/10) Anaplastic oligoastrocytoma WHO III, 20% (2/10) Anaplastic astrocytoma WHO III, 20% (2/10)	Glioblastoma WHO IV, 100% (7/7)	N/A
Genetic Mutation Status (Wild-type : Mutated)			
CDKN2A	9:1	3:4	0.037
TP53	3:7	5:2	0.104
EGFR	9:1	3:4	0.037
NF1	7:3	6:1	0.484
CDKN2B	10:0	3:4	0.004*
CDK4	8:2	5:2	0.704
TP53BP1	6:4	7:0	0.061
IDH1	1:9	6:1	<0.0001*
Histologic Expression Status (Not present : present)			
Endothelial proliferation	10:0	1:6	<0.0001*
Palisading necrosis	10:0	4:3	0.021

Table 3. Summary of MR Sequence Settings

MR Parameter	T1	T1+	T2	FLAIR	ADC
TR [ms] (0018, 0080)	2315.97 ±961.99 [500.00, 3116.00]	2645.97 ±1028.42 [500.00, 3236.34]	3427.45 ±449.42 [3000.00, 4000.00]	10002.35 ±0.79 [10002.00, 10004.00]	10000.00 ±0.00 [10000.00, 10000.02]
TE [ms] (0018, 0081)	7.81 ±2.98 [6.36, 14.00]	7.81 ±2.98 [6.36, 14.00]	92.59 ±27.17 [22.00, 104.97]	130.51 ±11.69 [123.50, 155.00]	75.45 ±7.40 [71.80, 99.00]
Inversion Time [ms] (0018, 0082)	1084.21 ±184.37 [860.00, 1238.00]	1211.00 ±101.02 [860.00, 1238.00]	0.00 ±0.00 [0.00, 0.00]	2241.18 ±19.65 [2200.00, 2250.00]	0.00 ±0.00 [0.00, 0.00]
Spacing between slices (0018, 0088)	4.65 ±0.79 [3.00, 5.00]	2.59 ±0.20 [2.50, 3.00]	4.65 ±0.79 [3.00, 5.00]	2.59 ±0.20 [2.50, 3.00]	4.81 ±0.75 [3.00, 6.00]
Acquisition matrix (0018, 1310)	313.60 ±17.94 [256.00, 320.00]	313.60 ±17.94 [256.00, 320.00]	317.87 ±19.00 [256.00, 352.00]	311.47 ±22.52 [256.00, 320.00]	128.00 ±0.00 [128.00, 128.00]
	219.73 ±11.26 [192.00, 224.00]	219.73 ±11.26 [192.00, 224.00]	219.73 ±11.26 [192.00, 224.00]	219.73 ±11.26 [192.00, 224.00]	128.00 ±0.00 [128.00, 128.00]
Pixel spacing (0028, 0030)	0.55 ±0.18 [0.47, 0.94]	0.55 ±0.18 [0.47, 0.94]	0.55 ±0.18 [0.47, 0.94]	0.57 ±0.19 [0.47, 0.94]	1.00 ±0.23 [0.94, 1.88]
Slice Thickness (0018, 0050)	4.65 ±0.79 [3.00, 5.00]	2.59 ±0.20 [2.50, 3.00]	4.65 ±0.79 [3.00, 5.00]	2.59 ±0.20 [2.50, 3.00]	4.81 ±0.75 [3.00, 6.00]
Number of Averages (0018, 0083)	1.31 ±0.79 [1.00, 4.00]	1.31 ±0.79 [1.00, 4.00]	2.00 ±0.00 [2.00, 2.00]	1.19 ±0.75 [1.00, 4.00]	1.00 ±0.00 [1.00, 1.00]
Parameters constant across sequences:					
Field strength 2.90 ±0.39 [1.50, 3.00]					
Flip angle 90.00 ±0.00 [90.00, 90.00]					
Mean ± standard deviation; [min, max]					

Image Annotation

Within our research team, a neurosurgeon and radiologist independently annotated regions of interest on a pre-selected T1-GD slice, after reviewing axial MRI data (T1, T2, FLAIR, ADC, T1-GD) for each patient on a local picture archiving and communication system (PACS). We annotated diseased regions with high confidence (>95%) in categories of (1) pure cyst without necrosis, (2) necrosis, (3) tumor, or (4) edema. For regions with moderate confidence of disease (>50%) but unknown classification, the reader could annotate the area as “suspicious” for disease. We also annotated uninvolved, normal appearing regions in categories of (1) white matter (WM), (2) gray matter (GM), (3) cerebral spinal fluid (CSF), or (4) air.

Image Registration and Feature Vector

We registered each MRI sequence to its respective T1-GD scan in FSL (Analysis Group, FMRIB v5.0, Oxford, UK) using an affine 12-parameter model with a correlation rasion cost function and tri-linear interpolation, spatially smoothed the data with a one-mm Gaussian filter, and normalized the qualitative sequences (T1, T1-GD, T2, and FLAIR) to each patient’s average normal-appearing WM. From the annotations we created a labeled matrix of feature vectors in which each observation represented one voxel within an annotated region across five MRI sequences. For disease annotations, only voxels with agreement between our neurosurgeon and radiologist were included in the feature vector. The resultant matrix contained 611,930 observations (voxels) from fourteen patients, across five feature vectors (MRI sequences), where each observation belonged to one of nine classes (annotation labels).

k-NN Radiomics Algorithm

We developed a radiomics algorithm based on the k-NN classification model in MATLAB® (R2017a, The MathWorks, Inc.), with model parameters listed in Table 4. Based on exploratory methods, the k-NN model demonstrated comparable or higher accuracy with lower computational requirements compared to other parametric and non-parametric machine learning methods. Our model trained on a randomly selected three-fourths of the labeled observations (N = 458,948) and tested on the remaining one-fourth (N = 152,982). The developed radiomics

algorithm then predicted the class of each voxel from eleven slices across five MRI contrasts as new observations from seventeen patients, resulting in a total of 13,018,171 class predictions. The predicted class slices included the disease annotation slice, and five slices superior and inferior to the diseased annotation slice. Next, we defined the PDC phenotypes for each classified slice as a distribution of percent suspicious (%Suspicious), percent edema (%Edema), percent tumor (%Tumor), percent cyst (%Cyst), and percent necrosis (%Necrosis).

Table 4. Summary of kNN model parameters

Property	Value
N Neighbors	10
Distance	Euclidean
Include ties	False (0)
Distance weight	Equal
Break ties	Smallest
NS Method	Kdtree
Bucket size	50
Standardize data	True (1)
Mu	[105.77, 124.69, 144.49, 67.62, 148.69]
Sigma	[134.92, 150.77, 182.78, 74.05, 219.84]
Prior probability	[0.0177, 0.0089, 0.0831, 0.0002, 0.0002, 0.1448, 0.0447, 0.5335, 0.1665]

Statistical Analysis

We performed statistical analyses with SPSS (IBM, Version 25), with an a priori α significance level of 0.05. We tested the assumption of normality for each continuous variable and applied Box-Cox transformations when necessary. We compared values of age at diagnosis, gender, binary genetic mutation status (CDKN2A, TP53, EGFR, NF1, CDKN2B, CDK4, TP53BP1, IDH1), and binary features of endothelial proliferation (EP) and palisading necrosis (PN) between LGG and GBM using student's t-test. We compared PFS and OS between groups using the log rank test, and tested the relationship between both PFS and OS with PDC phenotypes using linear regression. Although PFS and OS are censored variables, linear regression was appropriately applied because all cohort subjects experienced the same events. We used canonical discriminant analysis with a stepwise Wilk's lambda model that included independent factors with F probabilities < 0.1 and a Bonferroni correction to test differentiation power of one or more disease components on dependent categorical factors with significant prognostic

implications. The continuous variables included age at diagnosis and PDC phenotypes (%Suspicious, %Edema, %Tumor, %Cyst, and %Necrosis). The dependent variables included binary categorical factors of tumor grade (TCGA classification of LGG versus GBM), mutation status (wild-type versus mutant) of the abovementioned genes, and the histologic features of EP and PN. Genetic mutation status by patient is shown in Figure 7. We computed prior probabilities based on each dependent variable's group size and tested the final model with a cross-validation method.



Figure 9. Selected genetic mutation status defined as wild-type (light) or mutant (dark) by patient and TCGA grade class. Patients above the bold black line were diagnosed as GBM. Patients below the bold black line were diagnosed as LGG.

Results

k-NN Radiomics Algorithm Performance and Accuracy

The k-NN model demonstrated 97.0% average accuracy on the training data. On the five diseased tissue classifications, the average accuracy was $95.61 \pm 1.48\%$, with “Suspicious” having the highest performance at 98.4% and “Cyst” the poorest performance at 94.29%. Figure 8 shows the confusion matrix between the true and predicted classes for the testing data (N = 152,982). The Dice similarity coefficient (DSC) was calculated for each classification (Table 5). The average DSC was 94.35 ± 2.98 across all classes, 94.39 ± 1.90 across disease classes, and 94.29 ± 4.35 across normal tissue classes. Example expert annotations and predictions are shown in Figure 8.

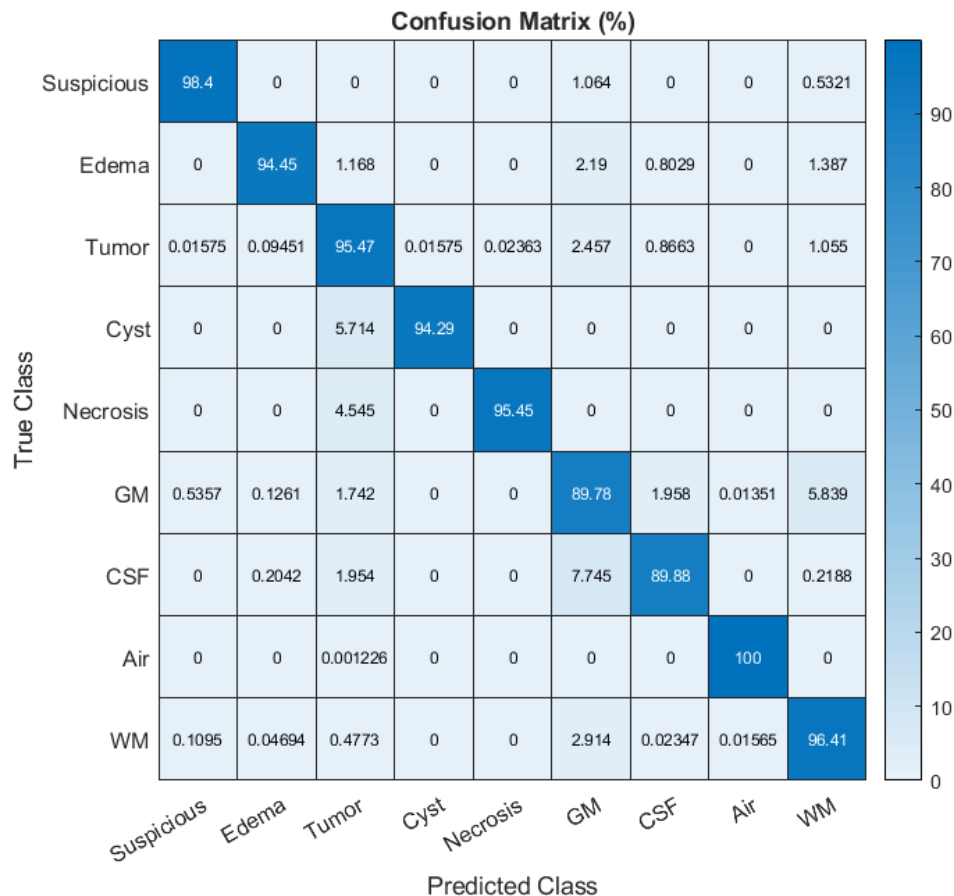


Figure 10. Radiomics algorithm k-NN Confusion Matrix. The k-NN model accuracy was tested using a 25% hold-out method. As observed, there is strong main axis agreement between the true and predicted classes. The accuracy for the entire model, including disease and normal tissue classes, was 97.0%. The average accuracy for the diseased classes was 95.61%.

Table 5. Dice similarity coefficient (DSC) computed for each class, based on the predicted class label and ground truth class label.

	Suspicious	Edema	Tumor	Cyst	Necrosis	GM	CSF	Air	WM
N_{truth}	2631	1370	12697	35	22	22212	6856	81596	25563
$N_{\text{predicted}}$	2589	1294	12122	33	21	19943	6162	81595	24646
DSC	96.44	94.8	95.14	94.29	91.3	91.06	90.75	100	95.36
Accuracy	98.40	94.45	95.47	94.29	95.45	89.78	89.88	100.00	96.41

Linear Regression

In linear regression analysis, the continuous variable %Tumor predicted OS [$F(1, 15) = 7.186, p = 0.017$] and accounted for 27.9% of the explained variability in OS. The regression equation was: Predicted OS = $7.67 - 0.037(\%Tumor)$. There was no relationship between PDC phenotypes and PFS.

Canonical Discriminant Analysis

The CDA determined that linear functions of one or more disease components differentiated the binary status of four out of 11 dependent categorical variables (Table 6). A linear combination of %Suspicious and age at diagnosis differentiated LGG from GBM with 76.5% accuracy, 85.7% sensitivity, and 70.0% specificity ($p = 0.014$). The discriminant equation to maximally separate discriminant score (DS) by TCGA study class was:

$$DS(\text{TCGA}) = 0.575(\%Suspicious) - 0.057(\text{Age at Diagnosis}) + 2.472.$$

The discriminant equation to maximally separate DS by IDH1 mutational status was: $DS(\text{IDH1}) = 0.040(\%Tumor) - 2.997$. EP status was differentiated with 88.2% classification accuracy, 66.7% sensitivity, and 100% specificity by %Necrosis and Age at Diagnosis ($p = 0.003$). The discriminant equation to maximally separate DS by EP status was:

$$DS(\text{EP}) = 2.479(\%Necrosis) + 0.066(\text{Age at Diagnosis}) - 24.253.$$

Table 6. Summary of Canonical Discriminant Analysis statistical findings. Accuracy, sensitivity, specificity, positive predictive value (PPV), and negative predictive value (NPV) are reported in percentage. Low (-) and high (+) state defined for CDA to maximally separate derived discriminant scores (DS). Confidence intervals (CI) were determined for each state from the DS calculated by the respective CDA model coefficients.

	TCGA	EP	TP53BP1	IDH1
Accuracy (%)	76.5	88.2	82.4	70.6
Sensitivity (%)	85.7	66.7	50.0	70.0
Specificity (%)	70.0	100	92.3	71.4
PPV (%)	66.7	100	66.7	77.8
NPV (%)	87.5	84.6	85.7	62.5
p value	0.014*	0.003*	0.097	0.054
Wilk's λ	0.544	0.442	0.827	0.774
χ^2	8.533	11.420	2.762	3.720
df	2	2	1	1
R canonical	0.676	0.747	0.416	0.476
CDA Model Coefficients				
Suspicious	0.575	-	0.711	-
Edema	-	-	-	-
Tumor	-	-	-	0.040
Necrosis	-	2.479	-	-
Age at Diagnosis	-0.057	0.066	-	-
Constant	2.472	-4.253	-0.989	-2.997
CDA Model Discriminant Score ANOVA				
Low state (-)	LGG	Not present	Wild type	Wild type
High state (+)	GBM	Present	Mutant	Mutant
Mean (-)	0.711	-0.791	-0.239	0.630
95% CI (-)	(0.036, 1.386)	(-1.432, -0.150)	(-0.829, 0.352)	(-0.181, 1.440)
Mean (+)	-1.041	1.412	0.774	-0.409
95% CI (+)	(-1.848, -0.234)	(0.544, 2.280)	(-0.291, 1.839)	(-1.087, 0.269)
p value	0.003	0.001	0.097	0.054
Effect Size	0.457	0.558	0.173	0.226
Observed Power	0.912	0.981	0.382	0.500

Discussion

Accurate glioma grading is critical for precise therapeutic planning.²¹ Histopathologic glioma grading, the diagnostic gold standard, has inherent limitations. Biopsies are often taken from areas of contrast enhancement that may fail to accurately characterize intratumoral heterogeneity and tumoral infiltration.^{22,23} Here we developed a voxel-wise radiomics method using multiparametric MRI data to PDC and their relevance to microscopic and molecular features. The major finding of this study is that PDC from multiparametric MRI data differentiates lower grade gliomas from GBM at the resolution of a single MRI voxel with accuracy, sensitivity, and specificity greater than or equal to 70%.

A unique tool for glioma research is BraTS: a multiparametric MRI data set of histologically confirmed LGG and GBM patients, which includes pre-intervention MRI data (T1, T2, T1Gd, FLAIR) registered to a universal, anatomical template (MNI-152) with manual segmentations for necrosis, edema, and contrast-enhancing tumor.¹⁵ However, previous studies with this have struggled to discriminate LGG from GBM with specificity greater than or equal to 70%.²⁴ Here we created a model with multiparametric MRI data from glioma patients in the TCGA, yielding strong agreement between true and predicted disease classes with 95.6% and 94.4% average DSC.

The continuous variable %Tumor inversely correlated with OS, which was worse in GBM compared to LGG ($p = 0.016$), as expected (Table 2). Although our CDA model did not find that %Tumor or %Necrosis predicted grade, GBM had higher %Tumor, %Necrosis, and age at diagnosis compared to LGG, which interestingly had greater %Suspicious ($p = 0.035, 0.016, 0.049, \text{ and } 0.015$, respectively), a classification defined during expert annotation as regions of moderate confidence for disease and potentially reflecting a more homogeneous abnormal compartment in LGG.²⁸ Additionally, we found differential power between LGG and GBM by a linear function of %Suspicious, and age at diagnosis. Specifically, with GBM being associated with a decrease in PDC Suspicious and an increase in age. Patients with GBM are generally older at diagnosis than patients with LGG.²⁵⁻²⁷

The most common pattern of confusion occurred when the true disease classes “Cyst” and “Necrosis” were predicted as “Tumor” and “Edema,” and when “Tumor” was predicted as “normal-appearing GM”. Such labeling confusion is expected, just as inter- and intra-observer

error is unavoidable,^{21, 22} and we attempted to mitigate this by defining disease class ground truth as voxels of agreement between the independent annotation of two expert clinicians.

Despite the promising results, this study has limitations. First, this retrospective study has a small sample size with variations in MRI protocols, manufacturers, and field strengths across different institutions. Although these variations may help support the generalizability of our findings, a future large-scale study is required to fully assess the generalizability of this model. Second, due to the limited sample size, this study applied machine learning techniques to each voxel as an observation across sequences resulting in a train and test feature vectors with randomly assigned voxels across patients. Since the voxels are randomly assigned to one of two feature vectors, a voxel neighboring a train voxel will be assigned to the test feature vector and could lead to over fitting. In the future, train and test feature vectors distributed by patient instead of random voxel selection should be explored. Third, the disease classification is based on annotation agreement between two expert readers following a common protocol. In future work, annotations should be collected from multiple experts following an established protocol and annotations of high agreement across expert readers should be used for a model.

In conclusion, we have proposed a five-feature, voxel-wise model with five phenotype signature described by PDC that have potential as an imaging biomarker to differentiate prognostic features. Non-invasive methods to reliably classify and differentiate prognostic features is an important development for the advancement of glioma treatment management. The results shown in this work demonstrate the promise and need for future development of computer-aided decision-making tools through multiparametric, voxel-wise radiomic algorithms. Utilizing the power of radiomics, gliomas may be non-invasively managed resulting in the advancement of treatment and care.

Using Nosologic Imaging Algorithms to Quantitatively Standardize Grade Differentiation in Adult Primary Glioma

Purpose: Nosologic imaging algorithms (NIAs) reduce large quantities of MR data to 3D maps of tumor type and grade. Frequently focused on MR spectroscopy, NIAs often fail to utilize routine clinical MR data. This work developed a multimodal NIA using five common clinical contrasts (ADC, FLAIR, T1, T1+, and T2) across high (GBM) and lower grade gliomas (LGG). We hypothesized that GBM would demonstrate an increased percentage of tumor necrotic voxels compared to LGG, and that survival time would have a positive correlation to the percentage of voxels classified as suspicious.

Methods: The NIA classified voxels based on a weighted k Nearest Neighbor machine-learning algorithm that trained on physician annotations of five abnormal tissue types (tumor, necrosis, edema, pure cyst, suspicious for tumor) across five MR contrasts (ADC, FLAIR, T1, T1+, T2) and predicted abnormal voxels as one of the five diseased classifications. An example of annotations for GBM and LGG is shown in Figure 9. Prognosis and MR data for 7 GBM and 10 LGG biopsy diagnosed patients were registered to the patients respective T1+ data and scaled to normal appearing white matter. The percent abnormal classification was analyzed in SPSS using a corrected multivariate general linear model ($\alpha=0.1$) and correlated to prognosis by a two-tail bivariate correlation test and Cox regression($\alpha=0.05$).

Results: The GBM patients had a higher percent of their tumor marked necrotic ($p=0.079$) compared to LGG, while LGG had a greater percent marked suspicious compared to GBM ($p=0.07$). Additionally, Percent suspicious had a positive correlation with survival time ($R=0.579$, $p=0.015$), shown in Figure 10.

Conclusion: For a small cohort, the NIA demonstrates promising results consistent with WHO diagnostic standards. These results provide preliminary support for our hypothesis and demonstrate that NIA may hold the potential to increase the accuracy, efficiency, and standardization of diagnosis in a clinical setting.

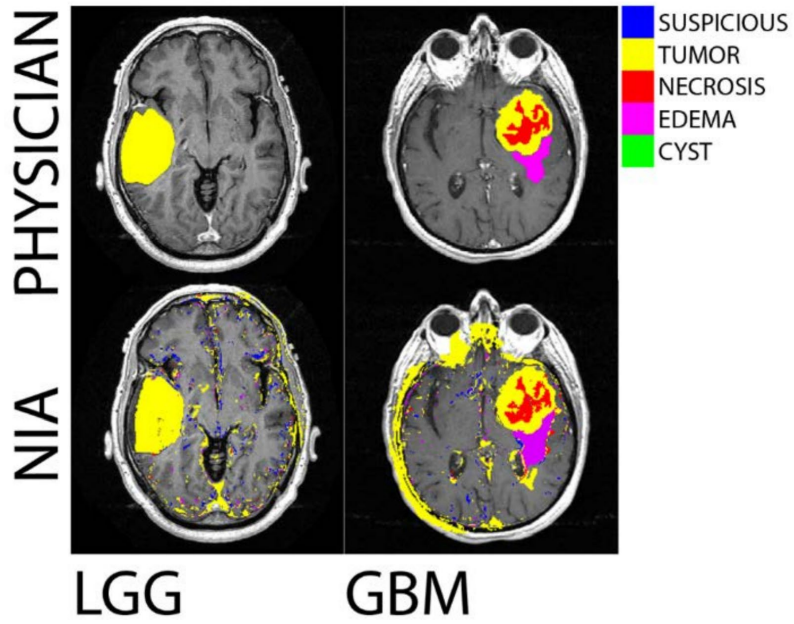


Figure 11. Comparison of NIA classifications for GBM and LGG diagnosis.

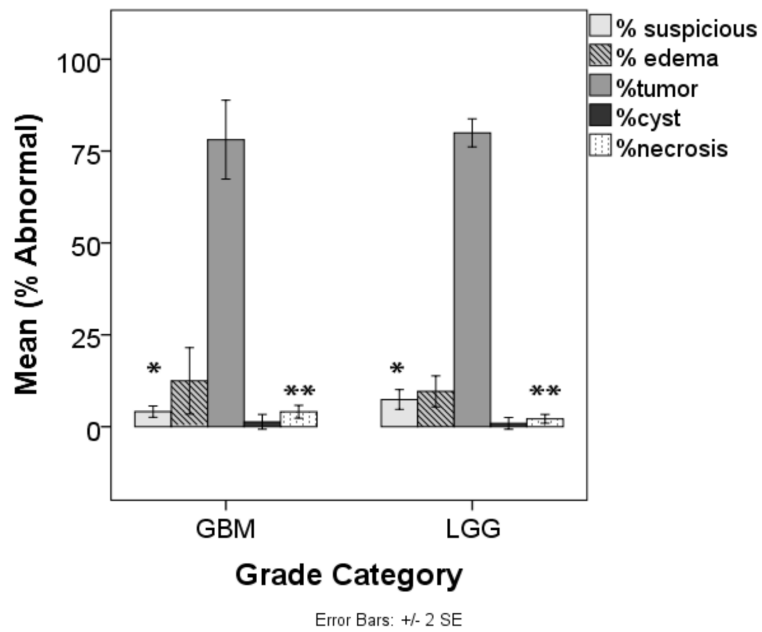


Figure 12. Statistical analysis for NIA percent abnormal classification between groups GBM and LGG.

Predicting Individual Survival Times from Multiparametric Nosologic Imaging Classifications of Glioblastoma

Purpose: Predicting individual survival times for patients with glioblastoma multiforme (GBM) can assist in treatment planning and clinical decision making. Genomic characterization has been used to predict prognosis, however detecting genomic abnormalities is invasive and expensive. The purpose of this study was to develop and evaluate a nosologic imaging algorithm (NIA) based on multiparametric magnetic resonance imaging (MRI) data to predict individual recurrence-free and overall survival times in GBM patients.

Materials and Methods: The NIA classified voxels independently using an image intensity decision tree based on published clinical studies. Abnormal voxels were classified as suspicious, low-grade, active, or necrotic. The NIA developed images and reported the percentage of voxels classified in each tissue types using multiparametric MRI data of 10 histologically-confirmed GBM patients from The Cancer Imaging Archive. MRI contrasts for each patient included: apparent diffusion coefficient maps generated from DWI; T1; T1+; T2; and fluid attenuated inversion recovery (FLAIR). Each contrast was registered to MNI-152 space using a 12 degree-of-freedom affine transformation. T1, T1+, T2, and FLAIR images were individually scaled to the fractional signal intensity relative to normal appearing white matter. Prognosis was measured in months as survival time and time to recurrence. Multivariate analysis was conducted to determine the pairwise correlations between NIA percentages and prognosis measures ($\alpha=0.10$).

Results: Consistent with published findings, the sampled patients had a 7.13 month median recurrence time and a 12.94 month median survival time. Percent suspicious is positively correlated with time to recurrence ($R=0.68$, $p=0.064$) and percent active is negatively correlated with time to recurrence ($R=0.89$, $p=0.036$). Additionally, percent low grade is positively correlated with overall survival time ($R=0.74$, $p=0.006$), while percent active ($R=0.78$, $p=0.042$) and percent necrotic ($R=0.83$, $p=0.044$) are negatively correlated with survival time. Correlations are shown in Figure 5.

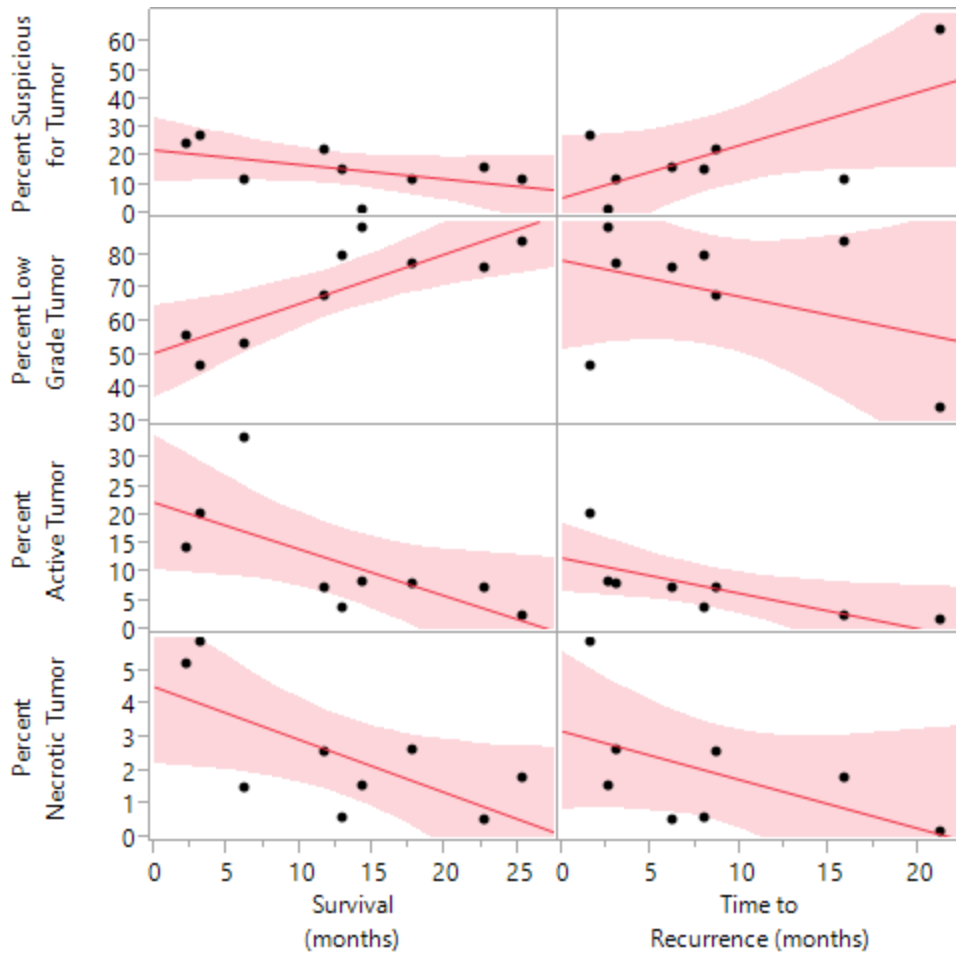


Figure 13. Correlation between percent of tumor in class and prognosis.

Conclusions: Our results indicate that quantitative NIA phenotypes can be used effectively to characterize GBM tumors and predict the prognosis of patients with GBM.

Clinical Relevance Statement: Simple volumetric studies with MRI data have been used to characterize tumor phenotypes. This study expands upon previous work to include additional MRI data to characterize tumor phenotypes for the prediction of prognosis in patients with GBM.

Integrating Cellular and Magnetic Relaxation Properties for Multimodal Nosologic Imaging of Gliomas

Purpose: Nosologic imaging (NI) utilizes voxel-by-voxel analyses to reduce MR data to 3D maps of tumor type and grade. Often focused on MR spectroscopy, NI fails to utilize vast amounts of data routinely collected during clinical examination. The purpose of this work was to develop a multimodal NI algorithm based on common clinical scans including DWI, FLAIR, T1, T1+, and T2 contrasts across high (GBM) and low grade gliomas (LGG). We hypothesized that GBM would demonstrate increased number of tumor necrotic voxels compared to LGG. This abstract presents initial results from our ongoing study.

Materials and Methods: The NI algorithm classified voxels independently based on thresholding logic of published tissue characteristics for cellular and magnetic relaxation properties. Voxels were categorized as normal, suspicious for tumor, low grade tumor, active tumor, or tumor necrotic. DWI, FLAIR, T1, T1+, and T2 MR data for 1 GBM and 3 LGG patients were obtained from The Cancer Imaging Archive (TCIA) and registered to MNI-152 T1 data using a 12 degree-of-freedom affine transformation with parameters optimized according to a correlation ratio cost function. Apparent diffusion coefficient (ADC) maps were calculated from registered DWI echo-planar volumes. The registered T1, T1+, T2, and FLAIR images were scaled on a voxel-by-voxel basis to the fractional signal intensity relative to normal appearing white matter (NAWM) for each patient.

Results: Consistent with World Health Organization diagnostic standards, the GBM patient had a marked increase in the percentage of necrotic tumor volume compared to all 3 LGG patients. Additionally, the LGG patients demonstrated increased suspicious and decreased active tumor volume compared to GBM shown in Figure 12.

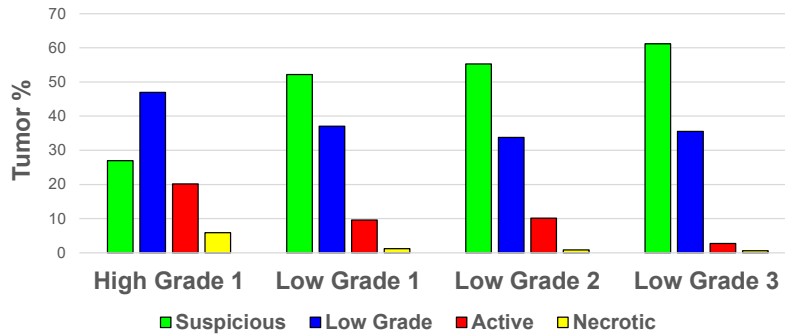


Figure 14. Percentage of the four conditions in one patient per diagnostic grade.

Conclusions: The multimodal NI algorithm correctly identified increased tumor necrotic voxels in GBM compared to LGG. These results provide preliminary support for our hypothesis and demonstrate that NI may hold the potential to increase the accuracy, efficiency, and standardization of diagnosis in a clinical setting. Data collection is ongoing with 13 GBM and 13 LGG datasets identified in TCIA to further statistically evaluate the multimodal NI algorithm.

Clinical Relevance Statement: This work developed automated multimodal NI for the grading of GBM and LGG tumors and holds the potential to spur future research to reduce the use of invasive biopsies of the brain.

References

- [1] Barnholtz-Sloan JS, Ostrom QT, Cote D. Epidemiology of Brain Tumors. *Neurologic Clinics* 2018;36:395-419. doi: 10.1016/j.ncl.2018.04.001
- [2] Cavenee WK, Wiestler OD, Ohgaki H, Louis H, editors. WHO classification of tumours of the central nervous system, revised, 4th edition. Lyon: IARC; 2016. p 15-76.
- [3] The cancer genome atlas research network. Comprehensive, integrative genomic analysis of diffuse lower-grade gliomas. *The New England Journal of Medicine* 2015;372:2481-2498. doi: 10.1056/NEJMoa1402121
- [4] Messaoudi K, Clavreul A, Lagarce F. Toward an effective strategy in glioblastoma treatment. Part I: Resistance mechanisms and strategies to overcome resistance of glioblastoma to temozolomide. *Drug Discov Today* 2015;20:899–905. doi: 10.1016/j.drudis.2015.02.011
- [5] Jackson RJ, Fuller GN, Abi-Said D, et al. Limitations of stereotactic biopsy in the initial management of gliomas. *Neuro Oncol* 2001;3:193-200. doi: 10.1093/neuonc/3.3.193
- [6] Grimm F, Naros G, Gutenberg A, Keric N, Giese A, Gharabaghi A. Blurring the boundaries between frame-based and frameless stereotaxy: feasibility study for brain biopsies performed with the use of a head-mounted robot. *Journal of Neurosurgery* 2015;123:732-742. doi: 10.3171/2014.12.JNS141781
- [7] Pope WB, Spittler K. Molecular imaging of diffuse low grade glioma. Duffau H editor. *Diffuse low-grade gliomas in adults*, 2nd edition. Springer, Cham; 2017. p 173-195. doi: 10.1007/978-3-319-55466-2_10
- [8] Roy B, Gupta R, Maudsley K, et al. Utility of multiparametric 3-T MRI for glioma characterization. *Neuroradiology* 2013;55:603-613. doi: 10.1007/s00234-013-1145-x
- [9] Zhang L, Min Z, Tang M, Chen S, Lei X, Zhang X. The utility of diffusion MRI with quantitative ADC measurements for differentiating high-grade from low-grade cerebral gliomas: Evidence from a meta-analysis. *Journal of the Neurological Sciences* 2013;373:9-15. doi: 10.1016/j.jns.2016.12.008
- [10] Gillies R, Kinahan P, Hricak, H. Radiomics: images are more than pictures, they are data. *Radiology* 2016;278:563-77. doi: 10.1148/radiol.2015151169

- [11] Nagarajan MB, Huber MB, Schlossbauer T, Leinsinger G, Krol A, Wismuller A. Classification of small lesions in breast MRI: Evaluating the role of dynamically extracted texture features through feature selection. *J Med Biol Eng* 2013;33(1). doi: 10.5405/jmbe.1183
- [12] Chen B, Zhang R, Gan Y, Yang L, Li W. Development and clinical application of radiomics in lung cancer. *Radiation Oncology* 2017;12:1-8. doi: 10.1186/s13014-017-0885-x
- [13] Fehr D, Veeraraghavan H, Wibmer A, et al. Automatic classification of prostate cancer Gleason scores from multiparametric magnetic resonance images. *Proc Natl Acad Sci U S A* 2015;112:E6265–6273. doi: 10.1073/pnas.1505935112
- [14] Caulo M, Panara V, Tortora D, et al. Data-driven grading of brain gliomas: A multiparametric MR imaging study. *Radiology* 2014;272:494–503. doi: 10.1148/radiol.14132040
- [15] Menze BH, Jakab A, Bauer S, et al. The multimodal brain tumor image segmentation benchmark (BRATS). *IEEE Trans Med Imaging* 2015;34:1993-2024. doi: 10.1109/TMI.2014.2377694
- [16] Bakas S, Akbari H, Sotiras A, et al. Advancing the cancer genome atlas glioma MRI collections with expert segmentation labels and radiomic features. *Sci Data* 2014;4:170117. doi: 10.1038/sdata.2017.117
- [17] Isensee F, Kickingereder P, Wick W, Bendsuz M, Maier-Hein KH. Brain tumor segmentation and radiomics survival prediction: Contribution to the BRATS 2017 challenge. *Lecture notes in computer science* 2018;10370:287-297. doi: /10.1007/978-3-319-75238-9_25
- [18] Inano R, Oishi N, Kunieda T, et al. Voxel-based clustered imaging by multiparameter diffusion tensor images for glioma grading. *NeuroImage: Clinical* 2014;5:396-407. doi: 10.1016/j.nicl.2014.08.001
- [19] Tian Q, Yan LF, Zhang X, et al. Radiomics strategy for glioma grading using texture features from multiparametric MRI. *JMRI* 2018. doi: 10.1002/jmri.26010
- [20] Chilla GS, Tan TH, Xu C, Poh CL. Diffusion weighted magnetic resonance imaging and its recent trend—a survey. *Quant Imaging Med Surg* 2015;5:407-422. doi: 10.3978/j.issn.2223-4292.2015.03.01

- [21] Whittle IR. The dilemma of low grade glioma. *Journal of Neurology, Neurosurgery & Psychiatry* 2004;75:31-36. doi: 10.1136/jnnp.2004.040501
- [22] Coons SW, Johnson PC, Scheithauer BW, Yates AJ, Pearl DK. Improving diagnostic accuracy and interobserver concordance in the classification and grading of primary gliomas. *Cancer* 1997;79:1381-93. doi: 10.1002/(SICI)1097-0142(19970401)79:7<1381::AID-CNCR16>3.0.CO;2-W
- [23] Cha S, Knopp EA, Johnson G, et al. Intracranial mass lesions: dynamic contrast-enhanced susceptibility-weighted echo-planar perfusion MR imaging. *Radiology* 2002;223:11–29. doi: 10.1148/radiol.2231010594
- [24] Cho H, Lee S, Kim J, Park H. (2018). Classification of the glioma grading using radiomics analysis. *PeerJ* 2018; 6: e5982. doi: 10.7717/peerj.5982
- [25] Ohgaki H, Kleihues P. Population-Based Studies on Incidence, Survival Rates, and Genetic Alterations in Astrocytic and Oligodendroglial Gliomas. *Journal of Neuropathology: Experimental Neurology* 2005;64:479-489. doi: 10.1093/jnen/64.6.479
- [26] Ostrom QT, Gittleman H, Fulop J, et al. CBTRUS Statistical Report: Primary Brain and Central Nervous System Tumors Diagnosed in the United States in 2008-2012. *Neuro-Oncology* 2015;17:1–62. doi: 10.1093/neuonc/nov189.
- [27] Dubrow R, Darefsky AS. Demographic variation in incidence of adult glioma by subtype, United States, 1992-2007. *BMC Cancer* 2011;11:325-335. doi: 10.1186/1471-2407-11-325
- [28] Nestler U, Lutz K, Pichlmeier U, et al. Anatomical features of glioblastoma and their potential impact on survival. *Acta Neurochir* 2015;157:179-186. doi: 10.1007/s00701-014-2271-x

CHAPTER FIVE: SIMULTANEOUS PET AND MRI

Feasibility of simultaneous dynamic PET and functional MRI studies

Introduction

In recent years, technological advancement and clinical interest has grown to support hybridization of imaging modalities. For decades, [18-F]-fluro-deoxyglucose (FDG) has been used to study glucose metabolism and utilization with positron emission tomography (PET)^{1,2}. In clinical FDG-PET studies, FDG is typically administered as a bolus with an uptake period ranging from twenty to sixty minutes^{3,4}. The bolus method allows for dose standardization across patients, however critical information of early FDG uptake is lost⁵. Additionally, once the brain reaches FDG equilibrium, task-based uptake information is no longer viable. In contrast to FDG-PET, functional magnetic resonance imaging (fMRI) has temporal resolution ranging on seconds and can be used to measure the brains task or stimulus-based response⁶. Blood oxygen level dependent (BOLD) fMRI sequences are used frequently for human studies, however these sequences are not true quantitative measurements, instead the relative changes represents the brains complex hemodynamic and metabolic response⁷. In this study, we aimed to establish methods for simultaneous dynamic PET and fMRI in healthy subjects.

Methods

Study design

All studies involving human subjects were reviewed and approved by the Human Research Protection Office (HRPO) at the Department of Defense Hearing Center of Excellence (FSG20180031H) and by the Institutional Review Board (IRB) at Indiana University (1803751735) and Wright State University (06168). This study consisted of an informed consent session and five consecutive data collection session, requiring up to eleven hours of the subjects time. On day one of data collection the subject had a PET/MRI scan and was required to fast for six hours prior to their appointment. On days two, three, and four the subject performed some training exercises. On day five, the subject had another PET/MRI scan and was required to fast

for six hours before their appointment. Female participants were required to provide a urine sample for a pregnancy test on days one and five, a negative result was required to continue participation. All subjects underwent a blood glucose test on days one and five, a normal value (70-120 mg/dL) was required to continue participation.

Subject recruitment

Subjects were recruited through physical flyers, digital flyers available to the Indiana University community, and through the Indiana Clinical and Translational Sciences Institute (CTSI) in compliance with Indiana University IRB recruitment policies. Potential subjects were screened digitally through the Indiana CTSI website. If the potential subject passed the web-based screening, they were contacted by email to schedule a telephone eligibility appointment. During the telephone eligibility appointment, the study design and subject responsibilities would be explained, if the potential subject was interested in participation then eligibility questions were administered. If the potential subject was eligible and interested in participation, then an in-person informed consent appointment was scheduled. Potential subjects were screened for MRI compatibility and defined inclusion and exclusion criteria, shown in Table 7. All subjects enrolled in the study were required to physically sign an informed consent document in compliance with IRB policies.

Table 7. Inclusion and exclusion criteria for simultaneous PET and MRI study

Inclusion Criteria	Exclusion Criteria
<ul style="list-style-type: none"> • Between 18 and 50 years of age • Able to read and write in English • Right-handed • Able to lay supine for up to an hour • Normal or corrected to normal vision • Able to complete all training sessions • Signed the informed consent 	<ul style="list-style-type: none"> • Conditions that would preclude the completion of an MRI • Serious unstable medical or mental illness • Have been diagnosed with diabetes • History of brain cancer or other brain disease • Medical contradiction to any element of the study procedure • Hearing loss above 40 dB • Have not signed the informed consent

Simultaneous PET/MRI design

All imaging studies were performed on a 3-T Siemens Biograph mMR scanner (Siemens Healthcare, Inc). PET data was collected continuously in large list-mode (LLM) format. Magnetic resonance imaging was collected with a 64 channel receive-only head and neck coil designed for the mMR considering photon attenuation properties (Siemens Healthcare, Inc.). A power injector administered a solution of FDG and saline. Auditory stimulation and instructions were delivered by in-ear headphones (Siemens Healthcare, Inc.) with consideration for photon attenuation. Functional MRI tasks were presented to the subject on a projection screen and formatted by Presentation (Neurobehavioral Systems, Inc.). Subject were provided with clickers to indicate a response to defined tasks. For temporal synchronization, the TR pulse was converted to a digital signal and elongated by 500 ms. The lengthened, digital TR pulse was then sent to the mMR as an external signal and permanently recorded in the LLM data. A pictorial representation of the experiment design is shown in Figure 13.

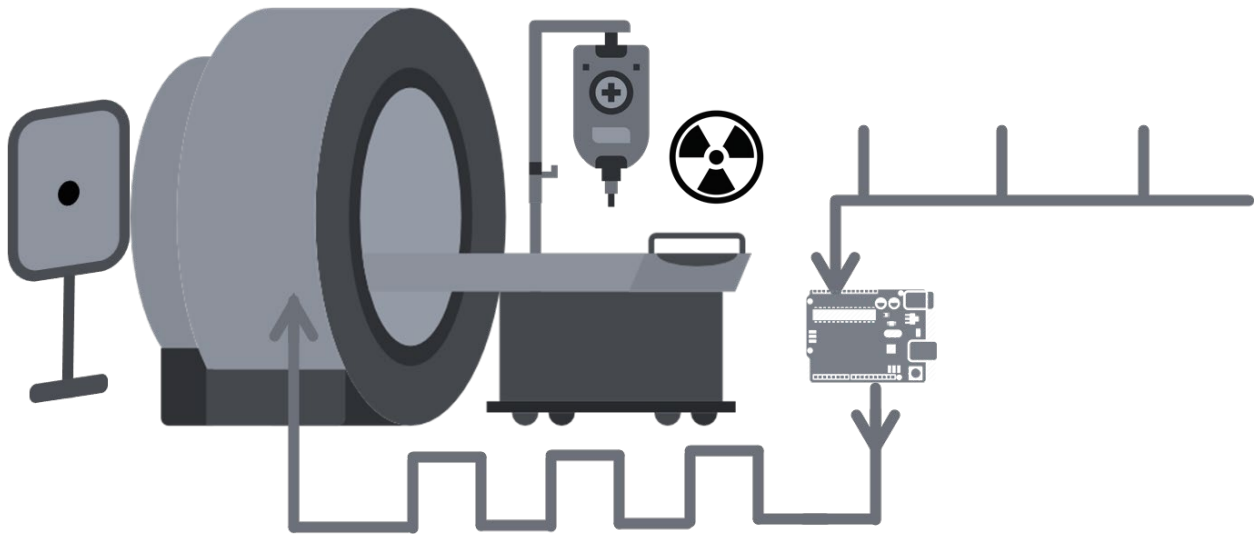


Figure 15. Pictorial representation of simultaneous dynamic PET and functional MRI study. A 3T Siemens mMR scanner was used to acquire simultaneous PET/MRI data. A MEDRAD power injector delivered a solution of FDG and saline. The digital TR pulse was elongated by an Arduino then sent to the mMR scanner and recorded in the LLM data as an external signal. A projection screen was placed at the head of the participant.

PET imaging protocol

A solution of FDG and saline was administered intravenously by power injector (MEDRAD MRXperion, Bayer HealthCare LLC) continuously at a rate of 0.01 ml/sec for up to 90 minutes. The max initial activity was 17 mCi, resulting in a max injected activity of 10 mCi per session. The LLM PET data was collected in one bed position consisting of 127 transverse slices of 344 x 344 pixels (2.0863 x 2.0863 mm²) and smoothed with a 5-mm isotropic Gaussian kernel.

MRI imaging protocol

All MRI sequences were obtained from the Siemens library and optimized for study design. Anatomical studies consisted of a MR based attenuation correction (MRAC) based on a 3D Dixon sequence with ultra-short TE sequence (TR = 4.14 ms, TE = 1.28 ms, flip angle = 10°, and voxel size of 1.3 x 1.3 x 2.0 mm) and a high-resolution 3D T1-weighted IRSPGR sequence (TR = 1960.0 ms, TE = 2.19 ms, TI = 989 ms, flip angle = 10°, and 1.0 mm isotropic). A 2D arterial spin labelling (ASL) sequence (TR = 3000 ms, TE = 13.0 ms, TI = 1800.0 ms, bolus duration = 700 ms, flip angle = 90°, and voxel size of 4.0 x 4.0 x 5.0 mm) was acquired. Functional MRI was acquired with a 2D EPI BOLD MOCO sequence (TR = 2000 ms, TE = 17.0 ms, flip angle = 78°, and voxel size of 3.8 x 3.8 x 3.0 mm). The protocol paradigm timeline is described in Figure 14. Additional information on protocol parameters can be found in Appendix A.

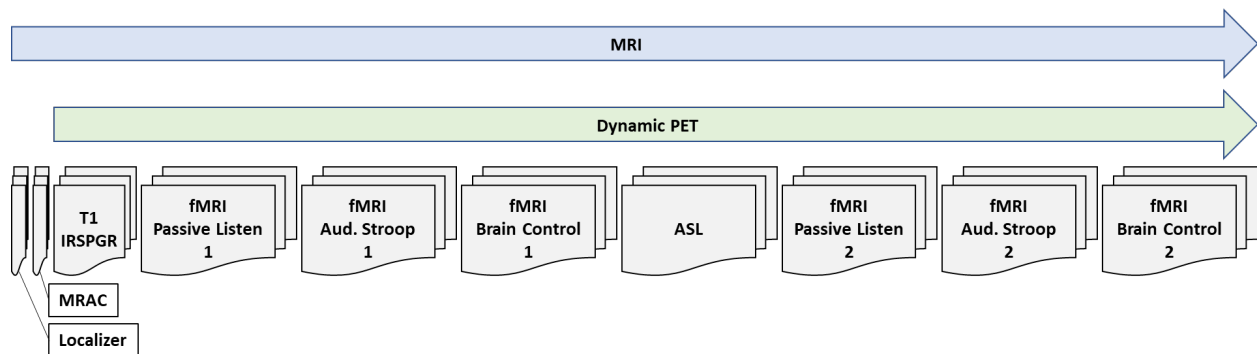


Figure 16. Simultaneous dynamic PET and MRI protocol paradigm. The protocol begins with a localizer and MR based attenuation correction (MRAC) sequence, then the dynamic PET begins with a constant infusion rate of 0.01 ml/sec. During the dynamic PET acquisition, an anatomical T1, an ASL, and six functional MRIs are acquired.

Auditory stimulation

The human auditory system was used for this dynamic PET and functional MRI study. To induce the hemodynamic and metabolic response three tasks were presented to the subject, the subject was given a break from the auditory stimulation during the ASL acquisition, then the three tasks were presented again. The three tasks (passive listening, auditory Stroop, and brain control), were in a block pattern and spanned 10 minutes and 14 seconds each.

During the passive listening task, the subject was informed that a dot would be on the screen and they may hear sounds in the headphones. The subject was instructed to relax, focus on the dot, and keep their body still. The auditory stimulation was white noise at constant volume presented in an on-off block pattern, Figure 15.

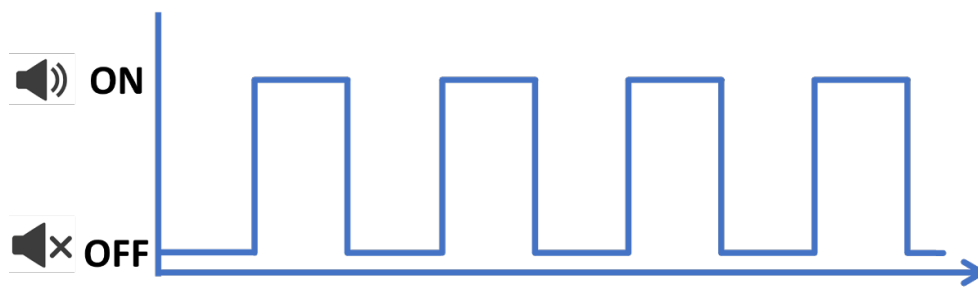


Figure 17. Passive listening on-off block design. During ‘on’ white noise sound is delivered to the participant through in ear headphones. During ‘off’ no sound is delivered to the participant through in ear headphones.

During the auditory Stroop task, the subject was informed that words would be on the screen and they would hear words in the headphones. The subject was instructed to press buttons with their right or left index finger to give a response and answer as quickly while keeping their body still. The auditory Stroop consisted of words presented on the screen and spoken words heard in the headphones. If the displayed and spoken words were both soft or low (congruent) the participant indicated with their left index finger. If the displayed and spoken words were both loud or high (congruent) the participant indicated with their right index finger. An example is shown in Figure 16.

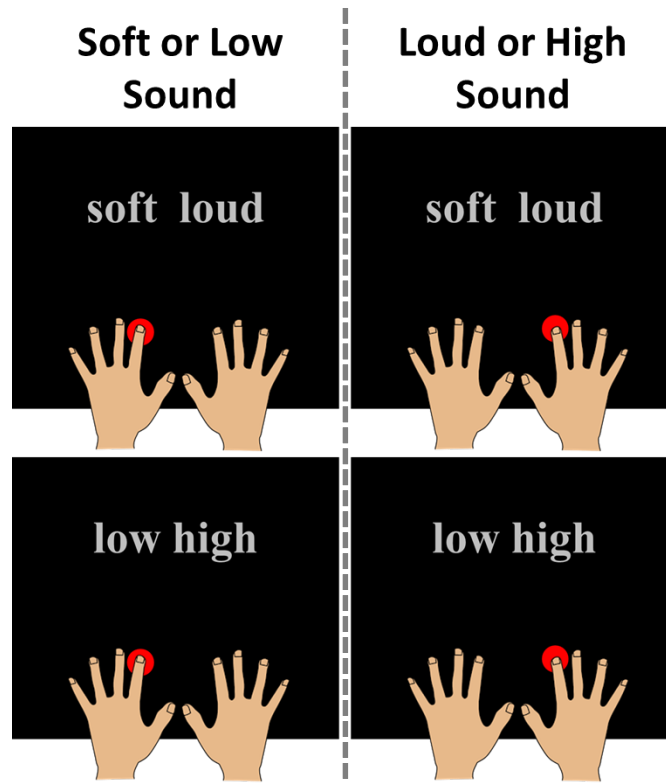


Figure 18. Auditory Stroop correct response examples. The red dot represents the subject using the indicated finger for a response. If the sound delivered is soft or low, the subject indicates with the button under their left index finger. If the sound delivered is loud or high, the subject indicates with the button under their right index finger.

For the brain control task, the participant was informed that the screen would say ‘focus on breathing’ or ‘focus on sound’ and they may hear sounds in the headphones. They were instructed to focus on their breathing and keep their body still when the screen displays ‘focus on breathing’ and to focus on the sound and keep their body still when ‘focus on sound’ is displayed. The auditory stimulation was white noise at constant volume presented in an on-off block pattern, see Figure 15.

Results

Subject recruitment

Recruitment efforts spanned a six-month period, 5,732 total users viewing the study recruitment website and entering personal information. Of the total users, 705 (12.29% of total users) completed their contact information and 441 (7.69% of total users) qualified for the study based

on their web-based responses. A total of 150 (2.62% of total users) requested to be contacted by a study staff member for a telephone eligibility appointment and 24 (0.42% of total users) consented to participate. Figure 17 shows the enrollment results by month.

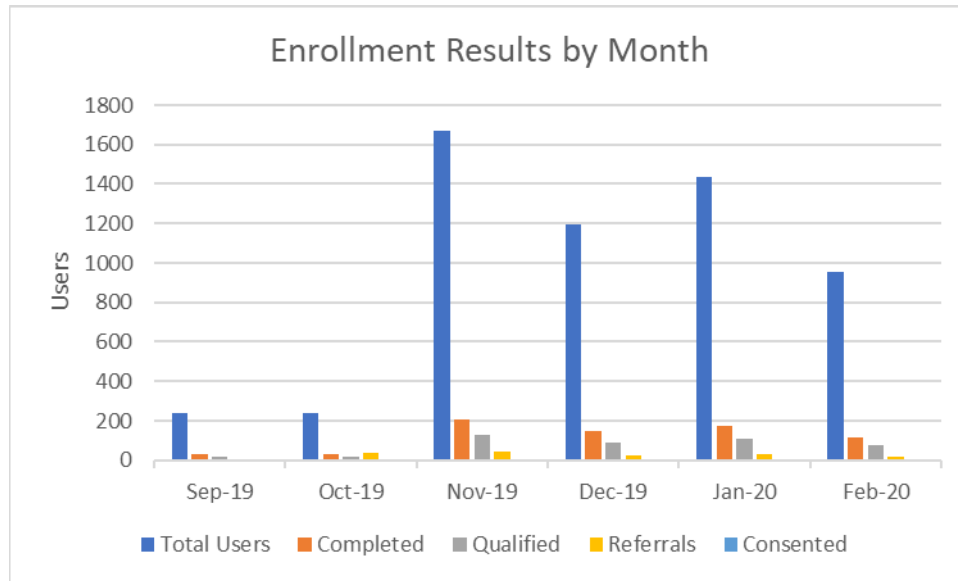


Figure 19. Enrollment results by month. Total users include potential subjects that enter some personal information on the Indiana CTSI study page. Completed users have completed all required information and the digital screener. Qualified users have completed the required information and passed the digital screener. Referrals are qualified users that have requested contact from study staff. Consented users have completed the informed consent process.

Of the twenty-four consented users, 33% (n=8) completed the study without issue. However, 13% (n=3) had incomplete data due to technical failure. Twenty-five percent of all consent users (n=6) were withdrawn from the study because they reported they no longer wanted to participate, or they did not attend an appointment. Unfortunately, 29% (n=7) were withdrawn due to novel coronavirus (COVID-19) scanning restrictions.

Initial and residual activity

Variability in initial dose was observed, however a students t-test showed there was no significant difference in the initial activity between sessions one and five ($p=0.46$) or residual activity between sessions one and five ($p=0.94$).

Table 8. Initial and residual activity by completed session

	<i>Session One (Initial)</i>	<i>Session Five (Initial)</i>	<i>Session One (Residual)</i>	<i>Session Five (Residual)</i>
<i>N</i>	11	10	11	8
<i>Mean activity (mCi)</i>	15.50818	16.04	0.661636364	0.67175
<i>Standard deviation (mCi)</i>	1.909224	1.224019	0.294065392	0.262880608
<i>Min activity (mCi)</i>	10.39	12.9	0.21	0.435
<i>Max activity (mCi)</i>	17	17	1.15	1.119

Discussion

Potential subject interest was high for this study, however the percentage of total users matriculating to consented subjects was less than one half percent, with one third of consented subjects completing the study. There are multiple factors responsible for this outcome. First, subjects were recruited from a university community. Potential subjects may have learned information, such as time requirement, and found they could not accommodate their complex schedule. Second, the study design may have presented unforeseen challenges for the participant leading to self-withdraw. Third, a global pandemic, the 2019 novel coronavirus, resulted in nearly one-third of subjects withdraw.

For many human studies, quality data hinges on consistent instructions. In this study, a script and power-point based tutorial was used for consistent subject instructions. An operator read the instructions to the participant for each task, however for greater standardization, the subject instructions could be recorded and added to the imaging protocol. Although all subjects had a training opportunity for each task, some reported misunderstanding the instructions.

Imaging studies with radioactive tracers, such as FDG, require consistent administration and initial activity. Clinically, there is an observed range in prescribed FDG dose. For this study our goal was an initial activity of 16.5 +/- 0.5 mCi, however we observed an average of 15.5 +/- 1.9 mCi and 16.0 +/- 1.2 mCi for sessions one and five respectively. Although the student's t-test demonstrated the initial activities were not significantly different between sessions, additional efforts should be made to standardize initial activity.

In conclusion, simultaneous dynamic PET and fMRI can be employed in a clinical setting. For diseased states, significant consideration for study design and reproducibility must be considered. Patients may not be able to reasonably complete their imaging sessions due to

acquisition length or frequent scheduling. Functional tasks must be carefully considered. The population in this study were healthy, young, and most connected to the Indiana University community. Although the cohort was presented with training materials, some were confused by task instructions.

PET count variation during PET/MRI acquisition with multiple EPI sequences

Purpose: Hybrid Positron emission tomography / magnetic resonance imaging (PET/MRI) holds potential to reduce total radiation dose and acquire simultaneous anatomical or functional MRI. However, some MRI sequences, such as echo-planar imaging (EPI), produce a considerable amount of heat and stress on PET detector components. We investigated if heating from an EPI intense MRI protocol effects normalized PET counts.

Methods: PET/MRI data was acquired prospectively on a Siemens Biograph mMR using a Siemens Ge-68 phantom in a Siemens Head/Neck 64 coil. The protocol spanned approximately 77 minutes acquiring: one SAG T1 IRSPGR; three EP 2D BOLD MOCO (approx. 10 min each); one TRA 2D ASL (approx. 10 min); and three EP 2D BOLD MOCO (approx. 10 min each). Data was collected under two conditions: (1) cold start, when the PET/MRI gradients were cool; and (2) warm start, when the PET/MRI gradients were warm from previous acquisitions. PET count data was normalized to a reference volume, defined as the volume of data acquired during the first five minutes of the protocol. Attenuation corrected (AC) and non-attenuation corrected (NAC) data were investigated. Decay correction over the acquisition period was not applied.

Results: During the cold start acquisition, the average initial temperature was 22C +/-1.12C and rose to 32.31C +/-9.31C as shown in Figure 18A. During the warm start acquisition, the average initial temperature was 33.83C +/-10.15C and rose to 38.67C +/-8.24C as shown in Figure 18B. For counts comparison, during the first half of the acquisition the normalized counts increased for both cold and warm starts with R-squared of 0.43 and 0.61 respectively.

Conclusion: EPI sequences produce a considerable amount of heat that may be deposited in PET detectors of hybrid PET/MRI systems. Between cold and warm start, considerable variation in gradient temperature is observed.

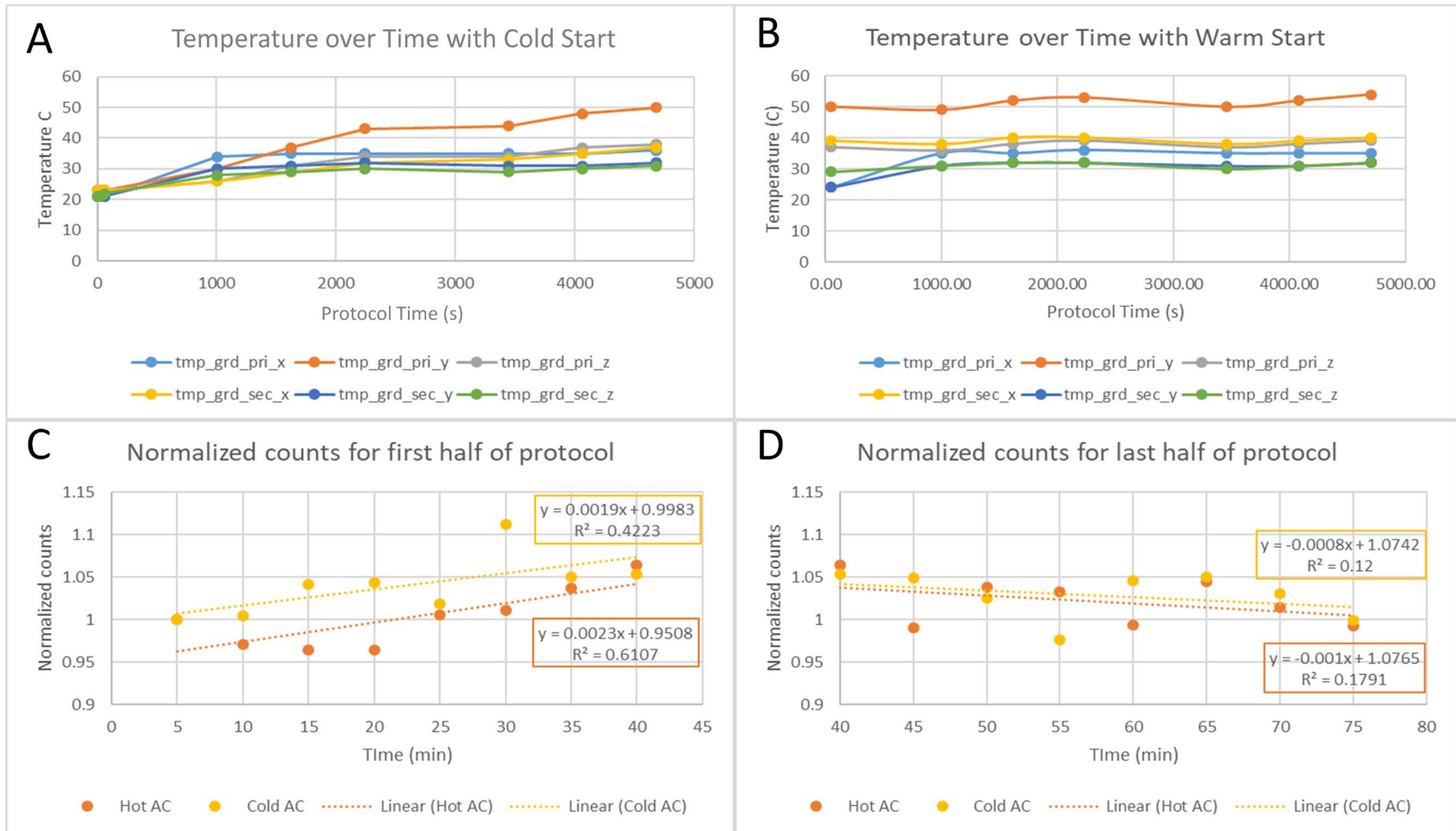


Figure 20. Temperature and counts changes during protocol. (A) Gantry temperatures during the protocol when the gantry started at homogeneous temperature (cold). (B) Gantry temperatures during the protocol when the gantry was “warm” with residual heat from previous protocol. (C) The normalized counts for the first half of the protocol for “cold” and “warm” conditions. (D) The normalized counts for the second half of the protocol for “cold” and “warm” conditions.

References

- [1] Phelps, M.E., Huang, S.C., Hoffman, E.J., Selin, C., Sokoloff, L., Kuhl, D.E., 1979. Tomographic measurement of local cerebral glucose metabolic rate in humans with (F-18)2-fluoro-2-deoxy-D-glucose: Validation of method. *Ann. Neurol.* 6, 371–388. <http://dx.doi.org/10.1002/ana.410060502>.
- [2] Reivich, M., Alavi, A., Wolf, A., Fowler, J., Russell, J., Arnett, C., MacGregor, R.R., Shiue, C.Y., Atkins, H., Anand, A., Dann, R., Greenberg, J.H., 1985. Glucose metabolic rate kinetic model parameter determination in humans: The lumped constants and rate constants for [18F]fluorodeoxyglucose and [11C]deoxyglucose. *J. Cereb. Blood Flow Metab.* 5, 179–192. <http://dx.doi.org/10.1038/jcbfm.1985.24>.
- [3] Fernandes C, Costa A, Osório L, et al. Current Standards of Care in Glioblastoma Therapy. In: De Vleeschouwer S, editor. *Glioblastoma*. Brisbane (AU): Codon Publications; 2017 Sep 27. Chapter 11. doi: 10.15586/codon.glioblastoma.2017.ch1
- [4] Demetriades AK, Almeida AC, Bhangoo RS, Barrington SF. Applications of positron emission tomography in neuro-oncology: A clinical approach. *Surg J R Coll Surg Edinb Irel.* 2014 Jun;12(3):148–57.
- [5] Verger A, Langen KJ. PET Imaging in Glioblastoma: Use in Clinical Practice. In: De Vleeschouwer S, editor. *Glioblastoma*. Brisbane (AU): Codon Publications; 2017 Sep 27. Chapter 9. doi: 10.15586/codon.glioblastoma.2017.ch9
- [6] Kalpathy-Cramer J, Gerstner ER, Emblem KE, Andronesi O, Rosen B. Advanced magnetic resonance imaging of the physical processes in human glioblastoma. *Cancer Res.* 2014;74(17):4622-4637. doi:10.1158/0008-5472.CAN-14-0383
- [7] Pike, G.B., 2012. Quantitative functional MRI: Concepts, issues and future challenges. *NeuroImage* 62, 1234–1240. <http://dx.doi.org/10.1016/j.neuroimage.2011.10.046>.

CHAPTER SIX: OUTLOOK

Glioblastoma (GBM) is an aggressive neoplasm, where if left untreated has a median overall survival (OS) of three months¹. Treatment for GBM is complex, the gold standard includes resection, radiation therapy, and conjunctive chemotherapy²⁻⁴. Since the breakthrough of Temozolomide (TMZ) chemotherapy, progression free survival (PFS) has increased while median OS with treatment remains at approximately 15 months⁴. Advances in medical imaging technique, genetic testing availability, and computational methods have resulted in large radiomic databases and increased interest in precision medicine. To advance GBM treatment and management, accurate models representing micro- and macroscopic intra-tumor heterogeneity are needed. Current models are largely based on correlations between qualitative magnetic resonance imaging (MRI) and single biopsy from an un-registered location. By utilizing hybrid imaging techniques, such as positron emission tomography (PET) and MRI, and spatially registered biopsy, we can establish quantitative models that may be more adaptable across institutions. Additionally, these radiomic models will likely provide useful insight for targeted, personalized therapy in GBM.

In 2016, the Food and Drug Administration (FDA) adapted a strategic plan to emphasize analytic approaches to health care⁵. Since then, multiple machine learning and predictive tools have been approved by the FDA for various disease states. For GBM treatment and management, quantitative computational analysis for personalized and precise treatment is in the horizon. However, there must be a sound ground truth that accurately describes microscopic intra-tumoral heterogeneity. Small animal models, such as mice, are intriguing and useful, but by nature fail to capture the full complexity of GBM in humans. Although complete resection of GBM is not possible, biopsy and resection is often spatially registered to medical imaging data by stereotaxis. Unfortunately, the stereotactic information is rarely saved with medical imaging data or medical records and thus not shared in repositories.

To create a reliable predictive model for GBM, a new clinical standard should be adopted across multiple institutions. Based on the presented work, incorporating advanced MRI and PET imaging results in critical information that is unattainable from qualitative MRI. Unfortunately, there are limitations to the extent of biopsies or resections obtained while maintaining patient safety and quality of life. However, relying on a single biopsy for a highly heterogenous tumor

like GBM is nonsensical, if available, multiple unique biopsy locations are critically important to capture the histologic and genomic variation. In order to improve GBM prognostic outcomes and develop targeted personalized treatments, future work must include critical data that correlates the micro to macroscopic features across space and time.

References

- [1] Malmstrom A, Gronberg BH, Marosi C, Stupp R, Frappaz D, Schultz H, et al. Temozolamide versus standard 6-week radiotherapy versus hypofractionated radiotherapy in patients older than 60 years with glioblastoma. The Nordic randomized phase 3 trial. *Lancet Oncol.* 2012;13:916–26.
- [2] Koshy M, Villano JL, Dolecek TA, Howard A, Mahmood U, Chmura SJ, et al. Improved survival time trends of glioblastoma using the SEER 17 population-based registries. *J Neuro Oncol.* 2012;107(1):207–12.
- [3] Stupp R, Mason WP, van den Bent MJ, Weller M, Fisher B, Taphoorn MJ, et al. Radiotherapy plus concomitant and adjuvant Temozolamide for glioblastoma. *N Engl J Med.* 2005;352:987–9
- [4] Fernandes C, Costa A, Osório L, et al. Current Standards of Care in Glioblastoma Therapy. In: De Vleeschouwer S, editor. *Glioblastoma*. Brisbane (AU): Codon Publications; 2017 Sep 27. Chapter 11. doi: 10.15586/codon.glioblastoma.2017.ch1
- [5] Shah, P., Kendall, F., Khozin, S. et al. Artificial intelligence and machine learning in clinical development: a translational perspective. *npj Digit. Med.* 2, 69 (2019). <https://doi.org/10.1038/s41746-019-0148-3>

APPENDIX A. SIMULTANEOUS PET AND MRI PROCEDURE INSTRUCTIONS

PROCEDURES

STUDY TITLE: Alternate Tinnitus Management Techniques Using Mobile Applications

FROM: Principle Investigator: **Jason Parker, Ph.D.**
Email Address: parkerjg@iu.edu
Cell: (941) 737-7549
Office: (317) 274-2072
Principle Investigator: **Matthew Sherwood, Ph.D.**
Email Address: matt.sherwood@wright.edu
Cell: (937) 503-7178
Associate Investigator: **Emily Diller, M.S.**
Email Address: emdiller@iu.edu; dillere@purdue.edu
Cell: (937) 701-1970
Office: (317) 278-9811

PROTOCOL #: 06168 (WSU-IRB); 1803751735 (IU-IRB)

VERSION: 2.0

DATE: 17 October 2019

ALTERNATIVE TINNITUS MANAGEMENT TECHNIQUES USING MOBILE APPLICATIONS

Exporting mMR Data Procedures

A. Export Subject MRI Data

1. Select the data to be exported in the **Patient Browser**.
2. In the Patient Browser menu, select **Transfer > Export to Offline...**
 - i. The **Export to Off-line...** dialog box opens.
3. Select the corresponding destination drive and start the export with **OK**.
 - i. You can check and control processing of the export in the **Local Job Status** dialog box.
4. In the main menu, select **Transfer > Local Job Status...**
 - i. The data structure of the Patient Browser will be maintained on the external device in the same hierarchy level (study, series, and images).
5. **Safely Eject** external drive. (i.e. click on USB icon on lower right of screen)

B. Export Subject Large ListMode data

1. Plug external hard drive into mMR control room PC
2. Enable Advanced User on Siemens PC
 - i. **CTRL+ESC > All Programs > Advanced User**
 - ii. Password: meduser1
3. Select the PET raw data in the **Patient Browser** (NOTE: Select sub folder not each individual LLM file)
4. In the Patient Browser menu, select **Applications > DICOM Tools > Export large ListMode files**. The **Export folder for large ListMode files** dialog box opens. The available and required disk space are displayed.
5. Select the corresponding destination folder. OR Create a new export folder by selecting **New Folder** in the context menu (right-click with the mouse).
6. Start the export with **OK**. If the required disk space is not sufficient, the **OK** button is dimmed. Large data exports might take some time to finish.
7. Check path that 8 files have been transferred and in **History** it should state "Dicom Tool Export LM succeeded (4/4)"
8. **Safely Eject** external drive. (i.e. click on USB icon on lower right of screen)

ALTERNATIVE TINNITUS MANAGEMENT TECHNIQUES USING MOBILE APPLICATIONS

Start Up Procedures

1. Turn on mMR
2. Turn on stimulus PC (IN-RADY-0217 PC left of mMR PC)
3. Unplug gray headphone cord and plug black headphone cord into stem PC (cords are under the table)
4. Turn on Cedrus Luimina (switch on back)
5. Turn on power injector
6. Turn on Brain Logics projector
 - a. Remove lens cap
 - b. Flip switch on back of projector
 - c. Press power button on remote while pointing it at wall side of projector (where IR receiver is)
 - d. Power light on projector and in control room will turn green
7. Move projector screen to mMR bore (black lines on floor for location)
8. Plug black earbuds into scanner (remove over ear headphones)
9. Plug in mMR head and neck coil
10. Check that stimulus cord is plugged into mMR (has arrow with head in circle -(>))
11. Start Presentation
 - a. Enter subject number (must be 201_1, 201_2, 202_1, 228_1, 228_2)
 - b. Fixation dot will be displayed until num-enter for passive listening task

ALTERNATIVE TINNITUS MANAGEMENT TECHNIQUES USING MOBILE APPLICATIONS

Shut down procedures

1. Export MR data to hard drive
2. Export Large List Mode data to hard drive
3. Turn off Cedrus Lumina
4. Turn off power injector
5. Send presentation data to box health
6. Unplug headphone cord and plug into gray cord
7. Turn off projector (flashes yellow/orange)
 - a. Press power button on remote (power light turns orange)
 - b. Flip switch on back of projector
 - c. Replace lens cap
8. Move screen away from MR bore
9. Replace earbuds with over the ear headphones
10. Remove head coil
11. Turn off stimulus PC
12. If data finished transferring and end of day, turn off mMR

ALTERNATIVE TINNITUS MANAGEMENT TECHNIQUES USING MOBILE APPLICATIONS

Power Injector Procedures

1. Acquire Components:

- Fluid source (FS) package
- 100 mL Saline
- Sterile fluid source cap

2. Fill Fluid Sources with Saline:

- Fill FS-A with 35 mL saline
- Fill FS-B with X mL saline (as instructed by Emily with slip of paper)
- Fill FS-B with 10 mL air
- Place sterile FS cap on FS-B
- Disconnect FS-B from power injector

3. Fill FS-B with FDG:

- Place FS-B in shielded work space
- Inject FDG into FS-B
- Place sterile cap on FS-B
- Gently mix FS-B
- Measure and record activity in FS-B

4. Connect hot FS-B to power injector and flush line

- Place FS-B in power injector
- Remove cap and place in hot trash holder
- Connect tubing to FS-B
- Advance power injector for FS-B
 - FS-B total volume= 53 mL
- Flush line with FS-A to clear air from line
 - FS-A total volume > 18 mL
- Place chuck under subject arm
- Connect tubing to patient IV
- Rotate power injector to down position

Component	Volume FDG (mL)	Volume Saline (mL)	Total Volume (mL)
FS-A	0	>18	>18
FS-B	X=	Y=53-X=	53

IU IRB Protocol: 1803751735

Revised 10/17/2019

ALTERNATIVE TINNITUS MANAGEMENT TECHNIQUES USING MOBILE APPLICATIONS

Verbal Instructions

Localizer, MRAC– *“During this scan relax and keep your body still. This scan will last approx. 2 minutes. Do you have any questions?”*

T1– *“During this scan relax and keep your body still. This scan will last approx. 5 minutes. Do you have any questions?”*

Passive listening fMRI- *“During this scan, a dot will be on the screen and you may hear sounds in the headphones. Your goal is to relax, focus on the dot, and keep your body still. This scan will last approx. 10 minutes. Do you have any questions?”*

Auditory Stroop fMRI – *“During this next scan, words will be on the screen and you will hear words in the headphones. Press buttons with your right or left index fingers to give a response. Your goal is to answer correctly as quickly as you can while keeping your body still. This scan will last approx. 10 minutes. Do you have any questions?”*

Brain control fMRI – *“During this scan, the screen will say ‘focus on breathing’ or ‘focus on sound’ and you may hear sounds in the headphones. When you see ‘focus on breathing’ your goal is to focus on your breathing and keep your body still. When you see ‘focus on sound’ your goal is to watch the screen, listen to the sound, and keep your body still. This scan will last approx. 10 minutes. Do you have any questions?”*

ASL– *“During this scan relax and keep your body still. This scan will last approx. 10 minutes. Do you have any questions?”*

Passive listening fMRI- *“During this scan, a dot will be on the screen and you may hear sounds in the headphones. Your goal is to relax, focus on the dot, and keep your body still. This scan will last approx. 10 minutes. Do you have any questions?”*

Auditory Stroop fMRI – *“During this next scan, words will be on the screen and you will hear words in the headphones. Press buttons with your right or left index fingers to give a response. Your goal is to answer correctly as quickly as you can while keeping your body still. This scan will last approx. 10 minutes. Do you have any questions?”*

Brain control fMRI – *“During this scan, the screen will say ‘focus on breathing’ or ‘focus on sound’ and you may hear sounds in the headphones. When you see ‘focus on breathing’ your goal is to focus on your breathing and keep your body still. When you see ‘focus on sound’ your goal is to watch the screen, listen to the sound, and keep your body still. This scan will last approx. 10 minutes. Do you have any questions?”*

ALTERNATIVE TINNITUS MANAGEMENT TECHNIQUES USING MOBILE APPLICATIONS

Patient Registration

PATIENT	
Field	Value
Last Name	2017-00161
First Name	# (where # is subject number)
Patient ID	R# (where # is the subject R number)
Date of Birth	Month of scan / Day of Scan / Year of Subject Birth
Sex	Other
Height	(real subject height from screener)
Weight	(real subject weight from screener)
Additional Info	Session #2 (if Monday) Session #6 (if Friday)

HOSPITAL	
Referring physician	Jason Parker

PROCEDURE	
Patient Position	Head First- Supine

STUDY	
Protocol	RESEARCH>Jason Parker>Tinnitus> Tinnitus protocol one Im
Body Part assignment	Brain

IU IRB Protocol: 1803751735
Revised 10/17/2019

APPENDIX B. PET/MR PROTOCOL

SIEMENS MAGNETOM Biograph_mMR

Table of contents	
\RESEARCH	
Jason Parker	
Tinnitus	
Tinnitus protocol one 1m	
localizer	
Head_PetAcquisition_all	
MRAC_Brain_HiRes	
SAG T1 IRSPGR 1mm ISO	
ep2d_bold_moco_PASSIVE_LISTEN_1	
ep2d_bold_moco_AUD_STROOP_1	
ep2d_bold_moco_BRAIN_CONTROL_1	
ASL_2D_tra	
ep2d_bold_moco_PASSIVE_LISTEN_2	
ep2d_bold_moco_AUD_STROOP_2	
ep2d_bold_moco_BRAIN_CONTROL_2	

\\RESEARCH\Jason Parker\Tinnitus\Tinnitus protocol one Im\localizer

TA: 0:14 PM: REF Voxel size: 0.5x0.5x7.0 mmPAT: Off Rel. SNR: 1.00 : fl

Properties

Prio recon	On
Load images to viewer	On
Inline movie	Off
Auto store images	On
Load images to stamp segments	On
Load images to graphic segments	On
Auto open inline display	Off
Auto close inline display	Off
Start measurement without further preparation	Off
Wait for user to start	Off
Start measurements	Single measurement

Routine

Slice group	1
Slices	1
Dist. factor	20 %
Position	L0.0 A20.0 H0.0 mm
Orientation	Sagittal
Phase enc. dir.	A >> P
Slice group	2
Slices	1
Dist. factor	20 %
Position	L0.0 A20.0 H0.0 mm
Orientation	Transversal
Phase enc. dir.	A >> P
Slice group	3
Slices	1
Dist. factor	20 %
Position	L0.0 A20.0 H0.0 mm
Orientation	Coronal
Phase enc. dir.	R >> L
AutoAlign	---
Phase oversampling	0 %
FoV read	250 mm
FoV phase	100.0 %
Slice thickness	7.0 mm
TR	8.6 ms
TE	3.69 ms
Averages	2
Concatenations	3
Filter	Distortion Corr.(2D), Prescan Normalize, Elliptical filter
Coil elements	HEA;HEP

Contrast - Common

TR	8.6 ms
TE	3.69 ms
TD	0 ms
MTC	Off
Magn. preparation	None
Flip angle	20 deg
Fat suppr.	None
Water suppr.	None
SWI	Off

Contrast - Dynamic

Averages	2
Averaging mode	Short term
Reconstruction	Magnitude

Contrast - Dynamic

Measurements	1
Multiple series	Each measurement

Resolution - Common

FoV read	250 mm
FoV phase	100.0 %
Slice thickness	7.0 mm
Base resolution	256
Phase resolution	91 %
Phase partial Fourier	Off
Interpolation	On

Resolution - iPAT

PAT mode	None
Matrix Coil Mode	Auto (Triple)

Resolution - Filter Image

Image Filter	Off
Distortion Corr.	On
Mode	2D
Unfiltered images	Off
Prescan Normalize	On
Unfiltered images	Off
Normalize	Off
B1 filter	Off

Resolution - Filter Rawdata

Raw filter	Off
Elliptical filter	On

Geometry - Common

Slice group	1
Slices	1
Dist. factor	20 %
Position	L0.0 A20.0 H0.0 mm
Orientation	Sagittal
Phase enc. dir.	A >> P
Slice group	2
Slices	1
Dist. factor	20 %
Position	L0.0 A20.0 H0.0 mm
Orientation	Transversal
Phase enc. dir.	A >> P
Slice group	3
Slices	1
Dist. factor	20 %
Position	L0.0 A20.0 H0.0 mm
Orientation	Coronal
Phase enc. dir.	R >> L
FoV read	250 mm
FoV phase	100.0 %
Slice thickness	7.0 mm
TR	8.6 ms
Multi-slice mode	Sequential
Series	Interleaved
Concatenations	3

Geometry - AutoAlign

Slice group	1
Slice group	2

Geometry - AutoAlign

Slice group	3
AutoAlign	---
Position	L0.0 A20.0 H0.0 mm
Orientation	Coronal
Phase enc. dir.	R >> L
Initial Position	L0.0 A20.0 H0.0
L	0.0 mm
A	20.0 mm
H	0.0 mm
Initial Rotation	0.00 deg
Initial Orientation	Sagittal

Geometry - Saturation

Saturation mode	Standard
Fat suppr.	None
Water suppr.	None
Special sat.	None

Geometry - Tim Planning Suite

Set-n-Go Protocol	Off
Table position	H
Table position	0 mm
Inline Composing	Off

Geometry - Tim CT

Tim CT mode	Off
Slices	1
Slice thickness	7.0 mm
Dist. factor	20 %
FoV read	250 mm
FoV phase	100.0 %
Segments	1

System - Miscellaneous

Positioning mode	REF
Table position	F
Table position	0 mm
MSMA	S - C - T
Sagittal	R >> L
Coronal	A >> P
Transversal	F >> H
Coil Combine Mode	Adaptive Combine
Save uncombined	Off
Matrix Coil Mode	Auto (Triple)
AutoAlign	---
Coil Select Mode	Off - AutoCoilSelect

System - Adjustments

B0 Shim mode	Tune up
B1 Shim mode	TrueForm
Adjust with body coil	Off
Confirm freq. adjustment	Off
Assume Dominant Fat	Off
Assume Silicone	Off
Adjustment Tolerance	Auto

System - Adjust Volume

Position	Isocenter
Orientation	Transversal
Rotation	0.00 deg
A >> P	263 mm
R >> L	350 mm
F >> H	350 mm
Reset	Off

System - Tx/Rx

Frequency 1H	123.259695 MHz
Correction factor	1
Gain	High
Img. Scale Cor.	1.000
Reset	Off
? Ref. amplitude 1H	0.000 V

Physio - Signal1

1st Signal/Mode	None
TR	8.6 ms
Concatenations	3
Segments	1

Physio - Cardiac

Magn. preparation	None
Fat suppr.	None
Dark blood	Off
FoV read	250 mm
FoV phase	100.0 %
Phase resolution	91 %

Physio - PACE

Resp. control	Off
Concatenations	3

Inline - Common

Subtract	Off
Measurements	1
StdDev	Off
Liver registration	Off
Save Original Images	On

Inline - MIP

MIP-Sag	Off
MIP-Cor	Off
MIP-Tra	Off
MIP-Time	Off
Save Original Images	On

Inline - Soft Tissue

Wash - In	Off
Wash - Out	Off
TTP	Off
PEI	Off
MIP - time	Off
Measurements	1

Inline - Composing

Inline Composing	Off
Distortion Corr.	On
Mode	2D
Unfiltered images	Off

Inline - MapIt

Save Original Images	On
MapIt	None
Flip angle	20 deg
Measurements	1
Contrasts	1
TR	8.6 ms
TE	3.69 ms

SIEMENS MAGNETOM Biograph_mMR

Sequence - Part 1

Introduction	On
Dimension	2D
Phase stabilisation	Off
Asymmetric echo	Allowed
Contrasts	1
Flow comp.	No
Multi-slice mode	Sequential
Bandwidth	320 Hz/Px

Sequence - Part 2

Segments	1
Acoustic noise reduction	None
RF pulse type	Normal
Gradient mode	Normal
Excitation	Slice-sel.
RF spoiling	On

Sequence - Assistant

Mode	Off
Allowed delay	0 s

\\RESEARCH\Jason Parker\Tinnitus\Tinnitus protocol one Im\Head_PetAcquisition_all

TA: 10:30 PM: FIX Voxel size: 2.3x2.3x5.0 mmRel. SNR: 1.00 ;

Properties

Prio recon	Off
Load images to viewer	On
Inline movie	Off
Auto store images	On
Load images to stamp segments	Off
Load images to graphic segments	Off
Auto open inline display	Off
Auto close inline display	Off
Wait for user to start	Off
Start measurements	Single measurement

<p style="text-align: center;">\\RESEARCH\Jason Parker\Tinnitus\Tinnitus protocol one Im\MRAC_Brain_HiRes</p> <p style="text-align: center;">TA: 0:39 PM: FIX Voxel size: 1.3x1.3x2.0 mmPAT: Off Rel. SNR: 1.00 : fl</p>

Properties

Prio recon	Off
Load images to viewer	On
Inline movie	Off
Auto store images	On
Load images to stamp segments	Off
Load images to graphic segments	Off
Auto open inline display	Off
Auto close inline display	Off
Start measurement without further preparation	Off
Wait for user to start	On
Start measurements	Single measurement

Inline - Composing

Mode	3D
Unfiltered images	Off

Resolution - iPAT

PAT mode	None
Matrix Coil Mode	Auto (Triple)

System - Miscellaneous

Positioning mode	FIX
Table position	H
Table position	0 mm
MSMA	S - C - T
Sagittal	R >> L
Coronal	A >> P
Transversal	F >> H
Coil Combine Mode	Adaptive Combine
Save uncombined	Off
Matrix Coil Mode	Auto (Triple)
AutoAlign	---
Coil Select Mode	Default

System - Adjustments

B0 Shim mode	Standard
B1 Shim mode	TrueForm
Adjust with body coil	Off
Confirm freq. adjustment	Off
Assume Dominant Fat	Off
Assume Silicone	Off
Adjustment Tolerance	Auto

System - Adjust Volume

Position	L0.0 A20.0 H0.0 mm
Orientation	Transversal
Rotation	0.00 deg
A >> P	266 mm
R >> L	500 mm
F >> H	259 mm
Reset	Off

System - Tx/Rx

Frequency 1H	123.259695 MHz
Correction factor	1
Gain	Low
Img. Scale Cor.	1.000
Reset	Off
? Ref. amplitude 1H	0.000 V

Inline - Composing

Inline Composing	Off
Distortion Corr.	On

\\RESEARCH\Jason Parker\Tinnitus\Tinnitus protocol one Im\SAG T1 IRSPGR 1mm ISO

TA: 4:34 PM: FIX Voxel size: 1.0x1.0x1.0 mmPAT: 2 Rel. SNR: 1.00 : tfl

Properties

Prio recon	Off
Load images to viewer	On
Inline movie	Off
Auto store images	On
Load images to stamp segments	On
Load images to graphic segments	On
Auto open inline display	Off
Auto close inline display	Off
Start measurement without further preparation	Off
Wait for user to start	On
Start measurements	Single measurement

Routine

Slab group	1
Slabs	1
Dist. factor	50 %
Position	L0.0 A20.3 H0.0 mm
Orientation	Sagittal
Phase enc. dir.	A >> P
AutoAlign	---
Phase oversampling	0 %
Slice oversampling	0.0 %
Slices per slab	176
FoV read	256 mm
FoV phase	100.0 %
Slice thickness	1.00 mm
TR	1960.0 ms
TE	2.19 ms
Averages	1
Concatenations	1
Filter	Raw filter, Distortion Corr.(2D), Prescan Normalize
Coil elements	HEA;HEP;NEA;NEP

Contrast - Common

TR	1960.0 ms
TE	2.19 ms
Magn. preparation	Non-sel. IR
TI	989 ms
Flip angle	10 deg
Fat suppr.	None
Water suppr.	None

Contrast - Dynamic

Averages	1
Averaging mode	Long term
Reconstruction	Magnitude
Measurements	1
Multiple series	Each measurement

Resolution - Common

FoV read	256 mm
FoV phase	100.0 %
Slice thickness	1.00 mm
Base resolution	256
Phase resolution	100 %
Slice resolution	100 %
Phase partial Fourier	Off
Slice partial Fourier	Off

Resolution - Common

Interpolation	Off
---------------	-----

Resolution - iPAT

PAT mode	GRAPPA
Accel. factor PE	2
Ref. lines PE	24
Accel. factor 3D	1
Matrix Coil Mode	Auto (Triple)
Reference scan mode	Integrated

Resolution - Filter Image

Image Filter	Off
Distortion Corr.	On
Mode	2D
Unfiltered images	Off
Prescan Normalize	On
Unfiltered images	Off
Normalize	Off
B1 filter	Off

Resolution - Filter Rawdata

Raw filter	On
Elliptical filter	Off

Geometry - Common

Slab group	1
Slabs	1
Dist. factor	50 %
Position	L0.0 A20.3 H0.0 mm
Orientation	Sagittal
Phase enc. dir.	A >> P
Slice oversampling	0.0 %
Slices per slab	176
FoV read	256 mm
FoV phase	100.0 %
Slice thickness	1.00 mm
TR	1960.0 ms
Multi-slice mode	Single shot
Series	Ascending
Concatenations	1

Geometry - AutoAlign

Slab group	1
AutoAlign	---
Position	L0.0 A20.3 H0.0 mm
Orientation	Sagittal
Phase enc. dir.	A >> P
Initial Position	L0.0 P0.0 H10.0
L	0.0 mm
P	0.0 mm
H	10.0 mm
Initial Rotation	0.00 deg
Initial Orientation	Sagittal

Geometry - Navigator**Geometry - Tim Planning Suite**

Set-n-Go Protocol	Off
Table position	H
Table position	0 mm

SIEMENS MAGNETOM Biograph_mMR

Geometry - Tim Planning Suite

Inline Composing	Off
------------------	-----

System - Miscellaneous

Positioning mode	FIX
Table position	H
Table position	0 mm
MSMA	S - C - T
Sagittal	R >> L
Coronal	P >> A
Transversal	F >> H
Coil Combine Mode	Adaptive Combine
Save uncombined	Off
Matrix Coil Mode	Auto (Triple)
AutoAlign	---
Coil Select Mode	On - AutoCoilSelect

System - Adjustments

B0 Shim mode	Tune up
B1 Shim mode	TrueForm
Adjust with body coil	Off
Confirm freq. adjustment	Off
Assume Dominant Fat	Off
Assume Silicone	Off
Adjustment Tolerance	Auto

System - Adjust Volume

Position	Isocenter
Orientation	Transversal
Rotation	0.00 deg
A >> P	263 mm
R >> L	350 mm
F >> H	350 mm
Reset	Off

System - Tx/Rx

Frequency 1H	123.259695 MHz
Correction factor	1
Gain	High
Img. Scale Cor.	1.000
Reset	Off
? Ref. amplitude 1H	0.000 V

Physio - Signal1

1st Signal/Mode	None
TR	1960.0 ms
Concatenations	1

Physio - Cardiac

Magn. preparation	Non-sel. IR
TI	989 ms
Fat suppr.	None
Dark blood	Off
FoV read	256 mm
FoV phase	100.0 %
Phase resolution	100 %

Physio - PACE

Resp. control	Off
Concatenations	1

Inline - Common

Subtract	Off
Measurements	1

Inline - Common

StdDev	Off
Save Original Images	On

Inline - MIP

MIP-Sag	Off
MIP-Cor	Off
MIP-Tra	Off
MIP-Time	Off
Save Original Images	On

Inline - Composing

Inline Composing	Off
Distortion Corr.	On
Mode	2D
Unfiltered images	Off

Inline - MapIt

Save Original Images	On
MapIt	None
Flip angle	10 deg
Measurements	1
TR	1960.0 ms
TE	2.19 ms

Sequence - Part 1

Introduction	On
Dimension	3D
Elliptical scanning	Off
Reordering	Linear
Asymmetric echo	Allowed
Flow comp.	No
Multi-slice mode	Single shot
Echo spacing	7.6 ms
Bandwidth	200 Hz/Px

Sequence - Part 2

RF pulse type	Normal
Gradient mode	Fast
Excitation	Non-sel.
RF spoiling	On
Incr. Gradient spoiling	On
Turbo factor	176

Sequence - Assistant

Mode	Off
------	-----

\\RESEARCH\Jason Parker\Tinnitus\Tinnitus protocol one Imlep2d_bold_moco_PASSIVE_LISTEN_1
TA: 10:14 PM: FIX Voxel size: 3.8x3.8x3.0 mmPAT: Off Rel. SNR: 1.00 : epfid

Properties

Prio recon	Off
Load images to viewer	On
Inline movie	Off
Auto store images	On
Load images to stamp segments	Off
Load images to graphic segments	Off
Auto open inline display	Off
Auto close inline display	Off
Start measurement without further preparation	Off
Wait for user to start	On
Start measurements	Single measurement

Routine

Slice group	1
Slices	41
Dist. factor	17 %
Position	Isocenter
Orientation	Transversal
Phase enc. dir.	A >> P
AutoAlign	---
Phase oversampling	0 %
FoV read	240 mm
FoV phase	100.0 %
Slice thickness	3.0 mm
TR	2000 ms
TE	17.0 ms
Averages	1
Concatenations	1
Filter	None
Coil elements	HEA,HEP

Contrast - Common

TR	2000 ms
TE	17.0 ms
MTC	Off
Flip angle	78 deg
Fat suppr.	Fat sat.

Contrast - Dynamic

Averages	1
Averaging mode	Long term
Reconstruction	Magnitude
Measurements	304
Delay in TR	0 ms
Multiple series	Off

Resolution - Common

FoV read	240 mm
FoV phase	100.0 %
Slice thickness	3.0 mm
Base resolution	64
Phase resolution	100 %
Phase partial Fourier	7/8
Interpolation	Off

Resolution - iPAT

PAT mode	None
Matrix Coil Mode	Auto (Triple)

Resolution - Filter Image

Distortion Corr.	Off
Prescan Normalize	Off

Resolution - Filter Rawdata

Raw filter	Off
Elliptical filter	Off
Hamming	Off

Geometry - Common

Slice group	1
Slices	41
Dist. factor	17 %
Position	Isocenter
Orientation	Transversal
Phase enc. dir.	A >> P
FoV read	240 mm
FoV phase	100.0 %
Slice thickness	3.0 mm
TR	2000 ms
Multi-slice mode	Interleaved
Series	Interleaved
Concatenations	1

Geometry - AutoAlign

Slice group	1
AutoAlign	---
Position	Isocenter
Orientation	Transversal
Phase enc. dir.	A >> P
Initial Position	Isocenter
L	0.0 mm
P	0.0 mm
H	0.0 mm
Initial Rotation	0.00 deg
Initial Orientation	Transversal

Geometry - Saturation

Fat suppr.	Fat sat.
Special sat.	None

Geometry - Tim Planning Suite

Set-n-Go Protocol	Off
Table position	H
Table position	0 mm
Inline Composing	Off

System - Miscellaneous

Positioning mode	FIX
Table position	H
Table position	0 mm
MSMA	S - C - T
Sagittal	R >> L
Coronal	A >> P
Transversal	F >> H
Coil Combine Mode	Sum of Squares
Matrix Coil Mode	Auto (Triple)
AutoAlign	---
Coil Select Mode	Off - AutoCoilSelect

SIEMENS MAGNETOM Biograph_mMR

System - Adjustments

B0 Shim mode	Standard
B1 Shim mode	TrueForm
Adjust with body coil	Off
Confirm freq. adjustment	Off
Assume Dominant Fat	Off
Assume Silicone	Off
Adjustment Tolerance	Auto

System - Adjust Volume

Position	Isocenter
Orientation	Transversal
Rotation	0.00 deg
A >> P	240 mm
R >> L	240 mm
F >> H	144 mm
Reset	Off

System - Tx/Rx

Frequency 1H	123.259695 MHz
Correction factor	1
Gain	High
Img. Scale Cor.	1.000
Reset	Off
? Ref. amplitude 1H	0.000 V

Physio - Signal1

1st Signal/Mode	None
TR	2000 ms
Concatenations	1

BOLD

GLM Statistics	Off
Dynamic t-maps	Off
Ignore meas. at start	0
Ignore after transition	0
Model transition states	On
Temp. highpass filter	On
Threshold	4.00
Paradigm size	40
Meas[1]	Baseline
Meas[2]	Baseline
Meas[3]	Baseline
Meas[4]	Baseline
Meas[5]	Baseline
Meas[6]	Baseline
Meas[7]	Baseline
Meas[8]	Baseline
Meas[9]	Baseline
Meas[10]	Baseline
Meas[11]	Baseline
Meas[12]	Baseline
Meas[13]	Baseline
Meas[14]	Baseline
Meas[15]	Baseline
Meas[16]	Baseline
Meas[17]	Baseline
Meas[18]	Baseline
Meas[19]	Baseline
Meas[20]	Baseline
Meas[21]	Active
Meas[22]	Active
Meas[23]	Active
Meas[24]	Active
Meas[25]	Active

BOLD

Meas[26]	Active
Meas[27]	Active
Meas[28]	Active
Meas[29]	Active
Meas[30]	Active
Meas[31]	Active
Meas[32]	Active
Meas[33]	Active
Meas[34]	Active
Meas[35]	Active
Meas[36]	Active
Meas[37]	Active
Meas[38]	Active
Meas[39]	Active
Meas[40]	Active
Motion Correction	Off
Spatial filter	Off
Measurements	304
Delay in TR	0 ms
Multiple series	Off

Sequence - Part 1

Introduction	On
Multi-slice mode	Interleaved
Free echo spacing	Off
Echo spacing	0.5 ms
Bandwidth	2298 Hz/Px

Sequence - Part 2

EPI factor	64
RF pulse type	Normal
Gradient mode	Fast

\\RESEARCH\Jason Parker\Tinnitus\Tinnitus protocol one Imep2d_bold_moco_AUD_STROOP_1
 TA: 10:14 PM: FIX Voxel size: 3.8x3.8x3.0 mmPAT: Off Rel. SNR: 1.00 : epdf

Properties

Prio recon	Off
Load images to viewer	On
Inline movie	Off
Auto store images	On
Load images to stamp segments	Off
Load images to graphic segments	Off
Auto open inline display	Off
Auto close inline display	Off
Start measurement without further preparation	Off
Wait for user to start	On
Start measurements	Single measurement

Routine

Slice group	1
Slices	41
Dist. factor	17 %
Position	Isocenter
Orientation	Transversal
Phase enc. dir.	A >> P
AutoAlign	---
Phase oversampling	0 %
FoV read	240 mm
FoV phase	100.0 %
Slice thickness	3.0 mm
TR	2000 ms
TE	17.0 ms
Averages	1
Concatenations	1
Filter	None
Coil elements	HEA;HEP

Contrast - Common

TR	2000 ms
TE	17.0 ms
MTC	Off
Flip angle	78 deg
Fat suppr.	Fat sat.

Contrast - Dynamic

Averages	1
Averaging mode	Long term
Reconstruction	Magnitude
Measurements	304
Delay in TR	0 ms
Multiple series	Off

Resolution - Common

FoV read	240 mm
FoV phase	100.0 %
Slice thickness	3.0 mm
Base resolution	64
Phase resolution	100 %
Phase partial Fourier	7/8
Interpolation	Off

Resolution - iPAT

PAT mode	None
Matrix Coil Mode	Auto (Triple)

Resolution - Filter Image

Distortion Corr.	Off
Prescan Normalize	Off

Resolution - Filter Rawdata

Raw filter	Off
Elliptical filter	Off
Hamming	Off

Geometry - Common

Slice group	1
Slices	41
Dist. factor	17 %
Position	Isocenter
Orientation	Transversal
Phase enc. dir.	A >> P
FoV read	240 mm
FoV phase	100.0 %
Slice thickness	3.0 mm
TR	2000 ms
Multi-slice mode	Interleaved
Series	Interleaved
Concatenations	1

Geometry - AutoAlign

Slice group	1
AutoAlign	---
Position	Isocenter
Orientation	Transversal
Phase enc. dir.	A >> P
Initial Position	Isocenter
L	0.0 mm
P	0.0 mm
H	0.0 mm
Initial Rotation	0.00 deg
Initial Orientation	Transversal

Geometry - Saturation

Fat suppr.	Fat sat.
Special sat.	None

Geometry - Tim Planning Suite

Set-n-Go Protocol	Off
Table position	H
Table position	0 mm
Inline Composing	Off

System - Miscellaneous

Positioning mode	FIX
Table position	H
Table position	0 mm
MSMA	S - C - T
Sagittal	R >> L
Coronal	A >> P
Transversal	F >> H
Coil Combine Mode	Sum of Squares
Matrix Coil Mode	Auto (Triple)
AutoAlign	---
Coil Select Mode	Off - AutoCoilSelect

System - Adjustments

B0 Shim mode	Standard
B1 Shim mode	TrueForm
Adjust with body coil	Off
Confirm freq. adjustment	Off
Assume Dominant Fat	Off
Assume Silicone	Off
Adjustment Tolerance	Auto

System - Adjust Volume

Position	Isocenter
Orientation	Transversal
Rotation	0.00 deg
A >> P	240 mm
R >> L	240 mm
F >> H	144 mm
Reset	Off

System - Tx/Rx

Frequency 1H	123.259695 MHz
Correction factor	1
Gain	High
Img. Scale Cor.	1.000
Reset	Off
? Ref. amplitude 1H	0.000 V

Physio - Signal1

1st Signal/Mode	None
TR	2000 ms
Concatenations	1

BOLD

GLM Statistics	Off
Dynamic t-maps	Off
Ignore meas. at start	0
Ignore after transition	0
Model transition states	On
Temp. highpass filter	On
Threshold	4.00
Paradigm size	40
Meas[1]	Baseline
Meas[2]	Baseline
Meas[3]	Baseline
Meas[4]	Baseline
Meas[5]	Baseline
Meas[6]	Baseline
Meas[7]	Baseline
Meas[8]	Baseline
Meas[9]	Baseline
Meas[10]	Baseline
Meas[11]	Baseline
Meas[12]	Baseline
Meas[13]	Baseline
Meas[14]	Baseline
Meas[15]	Baseline
Meas[16]	Baseline
Meas[17]	Baseline
Meas[18]	Baseline
Meas[19]	Baseline
Meas[20]	Baseline
Meas[21]	Active
Meas[22]	Active
Meas[23]	Active
Meas[24]	Active
Meas[25]	Active

BOLD

Meas[26]	Active
Meas[27]	Active
Meas[28]	Active
Meas[29]	Active
Meas[30]	Active
Meas[31]	Active
Meas[32]	Active
Meas[33]	Active
Meas[34]	Active
Meas[35]	Active
Meas[36]	Active
Meas[37]	Active
Meas[38]	Active
Meas[39]	Active
Meas[40]	Active
Motion Correction	Off
Spatial filter	Off
Measurements	304
Delay in TR	0 ms
Multiple series	Off

Sequence - Part 1

Introduction	On
Multi-slice mode	Interleaved
Free echo spacing	Off
Echo spacing	0.5 ms
Bandwidth	2298 Hz/Px

Sequence - Part 2

EPI factor	64
RF pulse type	Normal
Gradient mode	Fast

\\RESEARCH\Jason Parker\Tinnitus\Tinnitus protocol one Imlep2d_bold_moco_BRAIN_CONTROL_1
TA: 10:14 PM: FIX Voxel size: 3.8x3.8x3.0 mmPAT: Off Rel. SNR: 1.00 : epfid

Properties

Prio recon	Off
Load images to viewer	On
Inline movie	Off
Auto store images	On
Load images to stamp segments	Off
Load images to graphic segments	Off
Auto open inline display	Off
Auto close inline display	Off
Start measurement without further preparation	Off
Wait for user to start	On
Start measurements	Single measurement

Routine

Slice group	1
Slices	41
Dist. factor	17 %
Position	Isocenter
Orientation	Transversal
Phase enc. dir.	A >> P
AutoAlign	---
Phase oversampling	0 %
FoV read	240 mm
FoV phase	100.0 %
Slice thickness	3.0 mm
TR	2000 ms
TE	17.0 ms
Averages	1
Concatenations	1
Filter	None
Coil elements	HEA,HEP

Contrast - Common

TR	2000 ms
TE	17.0 ms
MTC	Off
Flip angle	78 deg
Fat suppr.	Fat sat.

Contrast - Dynamic

Averages	1
Averaging mode	Long term
Reconstruction	Magnitude
Measurements	304
Delay in TR	0 ms
Multiple series	Off

Resolution - Common

FoV read	240 mm
FoV phase	100.0 %
Slice thickness	3.0 mm
Base resolution	64
Phase resolution	100 %
Phase partial Fourier	7/8
Interpolation	Off

Resolution - iPAT

PAT mode	None
Matrix Coil Mode	Auto (Triple)

Resolution - Filter Image

Distortion Corr.	Off
Prescan Normalize	Off

Resolution - Filter Rawdata

Raw filter	Off
Elliptical filter	Off
Hamming	Off

Geometry - Common

Slice group	1
Slices	41
Dist. factor	17 %
Position	Isocenter
Orientation	Transversal
Phase enc. dir.	A >> P
FoV read	240 mm
FoV phase	100.0 %
Slice thickness	3.0 mm
TR	2000 ms
Multi-slice mode	Interleaved
Series	Interleaved
Concatenations	1

Geometry - AutoAlign

Slice group	1
AutoAlign	---
Position	Isocenter
Orientation	Transversal
Phase enc. dir.	A >> P
Initial Position	Isocenter
L	0.0 mm
P	0.0 mm
H	0.0 mm
Initial Rotation	0.00 deg
Initial Orientation	Transversal

Geometry - Saturation

Fat suppr.	Fat sat.
Special sat.	None

Geometry - Tim Planning Suite

Set-n-Go Protocol	Off
Table position	H
Table position	0 mm
Inline Composing	Off

System - Miscellaneous

Positioning mode	FIX
Table position	H
Table position	0 mm
MSMA	S - C - T
Sagittal	R >> L
Coronal	A >> P
Transversal	F >> H
Coil Combine Mode	Sum of Squares
Matrix Coil Mode	Auto (Triple)
AutoAlign	---
Coil Select Mode	Off - AutoCoilSelect

SIEMENS MAGNETOM Biograph_mMR

System - Adjustments

B0 Shim mode	Standard
B1 Shim mode	TrueForm
Adjust with body coil	Off
Confirm freq. adjustment	Off
Assume Dominant Fat	Off
Assume Silicone	Off
Adjustment Tolerance	Auto

System - Adjust Volume

Position	Isocenter
Orientation	Transversal
Rotation	0.00 deg
A >> P	240 mm
R >> L	240 mm
F >> H	144 mm
Reset	Off

System - Tx/Rx

Frequency 1H	123.259695 MHz
Correction factor	1
Gain	High
Img. Scale Cor.	1.000
Reset	Off
? Ref. amplitude 1H	0.000 V

Physio - Signal1

1st Signal/Mode	None
TR	2000 ms
Concatenations	1

BOLD

GLM Statistics	Off
Dynamic t-maps	Off
Ignore meas. at start	0
Ignore after transition	0
Model transition states	On
Temp. highpass filter	On
Threshold	4.00
Paradigm size	40
Meas[1]	Baseline
Meas[2]	Baseline
Meas[3]	Baseline
Meas[4]	Baseline
Meas[5]	Baseline
Meas[6]	Baseline
Meas[7]	Baseline
Meas[8]	Baseline
Meas[9]	Baseline
Meas[10]	Baseline
Meas[11]	Baseline
Meas[12]	Baseline
Meas[13]	Baseline
Meas[14]	Baseline
Meas[15]	Baseline
Meas[16]	Baseline
Meas[17]	Baseline
Meas[18]	Baseline
Meas[19]	Baseline
Meas[20]	Baseline
Meas[21]	Active
Meas[22]	Active
Meas[23]	Active
Meas[24]	Active
Meas[25]	Active

BOLD

Meas[26]	Active
Meas[27]	Active
Meas[28]	Active
Meas[29]	Active
Meas[30]	Active
Meas[31]	Active
Meas[32]	Active
Meas[33]	Active
Meas[34]	Active
Meas[35]	Active
Meas[36]	Active
Meas[37]	Active
Meas[38]	Active
Meas[39]	Active
Meas[40]	Active
Motion Correction	Off
Spatial filter	Off
Measurements	304
Delay in TR	0 ms
Multiple series	Off

Sequence - Part 1

Introduction	On
Multi-slice mode	Interleaved
Free echo spacing	Off
Echo spacing	0.5 ms
Bandwidth	2298 Hz/Px

Sequence - Part 2

EPI factor	64
RF pulse type	Normal
Gradient mode	Fast

\\RESEARCH\Jason Parker\Tinnitus\Tinnitus protocol one Im\ASL_2D_tra

TA: 9:38 PM: FIX Voxel size: 4.0x4.0x5.0 mmPAT: Off Rel. SNR: 1.00 : epfd

Properties

Prio recon	Off
Load images to viewer	On
Inline movie	Off
Auto store images	On
Load images to stamp segments	Off
Load images to graphic segments	Off
Auto open inline display	Off
Auto close inline display	Off
Start measurement without further preparation	Off
Wait for user to start	On
Start measurements	Single measurement

Routine

Slice group	1
Slices	22
Dist. factor	20 %
Position	Isocenter
Orientation	Transversal
Phase enc. dir.	A >> P
AutoAlign	Head > Brain
Phase oversampling	0 %
FoV read	256 mm
FoV phase	100.0 %
Slice thickness	5.0 mm
TR	3000 ms
TE	13.0 ms
Averages	1
Concatenations	1
Filter	Prescan Normalize
Coil elements	HEA;HEP

Contrast - Common

TR	3000 ms
TE	13.0 ms
Flip angle	90 deg
Fat suppr.	Fat sat.
Fat sat. mode	Strong

Contrast - Dynamic

Averages	1
Averaging mode	Long term
Reconstruction	Magnitude
Measurements	191
Delay in TR	0 ms
Multiple series	Off

Contrast - ASL

Perfusion mode	PICORE Q2T
Quality check	On
Bolus Duration	700 ms
Inversion Time	1800.0 ms
Inversion Array Size	1
Flow limit	100.0 cm/s

Resolution - Common

FoV read	256 mm
FoV phase	100.0 %
Slice thickness	5.0 mm
Base resolution	64

Resolution - Common

Phase resolution	100 %
Phase partial Fourier	6/8
Interpolation	Off

Resolution - iPAT

PAT mode	None
Matrix Coil Mode	Auto (Triple)

Resolution - Filter Image

Distortion Corr.	Off
Prescan Normalize	On

Resolution - Filter Rawdata

Raw filter	Off
Elliptical filter	Off
Hamming	Off

Geometry - Common

Slice group	1
Slices	22
Dist. factor	20 %
Position	Isocenter
Orientation	Transversal
Phase enc. dir.	A >> P
FoV read	256 mm
FoV phase	100.0 %
Slice thickness	5.0 mm
TR	3000 ms
Multi-slice mode	Interleaved
Series	Ascending
Concatenations	1

Geometry - AutoAlign

Slice group	1
AutoAlign	Head > Brain
Position	Isocenter
Orientation	Transversal
Phase enc. dir.	A >> P
Initial Position	Isocenter
L	0.0 mm
P	0.0 mm
H	0.0 mm
Initial Rotation	0.00 deg
Initial Orientation	Transversal

Geometry - Saturation

Fat suppr.	Fat sat.
Fat sat. mode	Strong
Special sat.	Parallel F
Gap	28.0 mm
Thickness	100 mm

Geometry - Tim Planning Suite

Set-n-Go Protocol	Off
Table position	H
Table position	0 mm
Inline Composing	Off

System - Miscellaneous

Positioning mode	FIX
Table position	H
Table position	0 mm
MSMA	S - C - T
Sagittal	R >> L
Coronal	A >> P
Transversal	F >> H
Coil Combine Mode	Adaptive Combine
Matrix Coil Mode	Auto (Triple)
AutoAlign	Head > Brain
Coil Select Mode	Off - AutoCoilSelect

System - Adjustments

B0 Shim mode	Standard
B1 Shim mode	TrueForm
Adjust with body coil	Off
Confirm freq. adjustment	Off
Assume Dominant Fat	Off
Assume Silicone	Off
Adjustment Tolerance	Auto

System - Adjust Volume

Position	Isocenter
Orientation	Transversal
Rotation	0.00 deg
A >> P	256 mm
R >> L	256 mm
F >> H	131 mm
Reset	Off

System - Tx/Rx

Frequency 1H	123.259695 MHz
Correction factor	1
Gain	High
Img. Scale Cor.	1.000
Reset	Off
? Ref. amplitude 1H	0.000 V

Physio - Signal1

1st Signal/Mode	None
TR	3000 ms
Concatenations	1

Perf

Measurements	191
Motion Correction	On
Spatial filter	Off

Sequence - Part 1

Introduction	On
Multi-slice mode	Interleaved
Free echo spacing	Off
Echo spacing	0.5 ms
Bandwidth	2368 Hz/Px

Sequence - Part 2

EPI factor	64
RF pulse type	Normal
Gradient mode	Fast

\\RESEARCH\Jason Parker\Tinnitus\Tinnitus protocol one Imlep2d_bold_moco_PASSIVE_LISTEN_2
TA: 10:14 PM: FIX Voxel size: 3.8x3.8x3.0 mmPAT: Off Rel. SNR: 1.00 : epfid

Properties

Prio recon	Off
Load images to viewer	On
Inline movie	Off
Auto store images	On
Load images to stamp segments	Off
Load images to graphic segments	Off
Auto open inline display	Off
Auto close inline display	Off
Start measurement without further preparation	Off
Wait for user to start	On
Start measurements	Single measurement

Routine

Slice group	1
Slices	41
Dist. factor	17 %
Position	Isocenter
Orientation	Transversal
Phase enc. dir.	A >> P
AutoAlign	---
Phase oversampling	0 %
FoV read	240 mm
FoV phase	100.0 %
Slice thickness	3.0 mm
TR	2000 ms
TE	17.0 ms
Averages	1
Concatenations	1
Filter	None
Coil elements	HEA,HEP

Contrast - Common

TR	2000 ms
TE	17.0 ms
MTC	Off
Flip angle	78 deg
Fat suppr.	Fat sat.

Contrast - Dynamic

Averages	1
Averaging mode	Long term
Reconstruction	Magnitude
Measurements	304
Delay in TR	0 ms
Multiple series	Off

Resolution - Common

FoV read	240 mm
FoV phase	100.0 %
Slice thickness	3.0 mm
Base resolution	64
Phase resolution	100 %
Phase partial Fourier	7/8
Interpolation	Off

Resolution - iPAT

PAT mode	None
Matrix Coil Mode	Auto (Triple)

Resolution - Filter Image

Distortion Corr.	Off
Prescan Normalize	Off

Resolution - Filter Rawdata

Raw filter	Off
Elliptical filter	Off
Hamming	Off

Geometry - Common

Slice group	1
Slices	41
Dist. factor	17 %
Position	Isocenter
Orientation	Transversal
Phase enc. dir.	A >> P
FoV read	240 mm
FoV phase	100.0 %
Slice thickness	3.0 mm
TR	2000 ms
Multi-slice mode	Interleaved
Series	Interleaved
Concatenations	1

Geometry - AutoAlign

Slice group	1
AutoAlign	---
Position	Isocenter
Orientation	Transversal
Phase enc. dir.	A >> P
Initial Position	Isocenter
L	0.0 mm
P	0.0 mm
H	0.0 mm
Initial Rotation	0.00 deg
Initial Orientation	Transversal

Geometry - Saturation

Fat suppr.	Fat sat.
Special sat.	None

Geometry - Tim Planning Suite

Set-n-Go Protocol	Off
Table position	H
Table position	0 mm
Inline Composing	Off

System - Miscellaneous

Positioning mode	FIX
Table position	H
Table position	0 mm
MSMA	S - C - T
Sagittal	R >> L
Coronal	A >> P
Transversal	F >> H
Coil Combine Mode	Sum of Squares
Matrix Coil Mode	Auto (Triple)
AutoAlign	---
Coil Select Mode	Off - AutoCoilSelect

System - Adjustments

B0 Shim mode	Standard
B1 Shim mode	TrueForm
Adjust with body coil	Off
Confirm freq. adjustment	Off
Assume Dominant Fat	Off
Assume Silicone	Off
Adjustment Tolerance	Auto

System - Adjust Volume

Position	Isocenter
Orientation	Transversal
Rotation	0.00 deg
A >> P	240 mm
R >> L	240 mm
F >> H	144 mm
Reset	Off

System - Tx/Rx

Frequency 1H	123.259695 MHz
Correction factor	1
Gain	High
Img. Scale Cor.	1.000
Reset	Off
? Ref. amplitude 1H	0.000 V

Physio - Signal1

1st Signal/Mode	None
TR	2000 ms
Concatenations	1

BOLD

GLM Statistics	Off
Dynamic t-maps	Off
Ignore meas. at start	0
Ignore after transition	0
Model transition states	On
Temp. highpass filter	On
Threshold	4.00
Paradigm size	40
Meas[1]	Baseline
Meas[2]	Baseline
Meas[3]	Baseline
Meas[4]	Baseline
Meas[5]	Baseline
Meas[6]	Baseline
Meas[7]	Baseline
Meas[8]	Baseline
Meas[9]	Baseline
Meas[10]	Baseline
Meas[11]	Baseline
Meas[12]	Baseline
Meas[13]	Baseline
Meas[14]	Baseline
Meas[15]	Baseline
Meas[16]	Baseline
Meas[17]	Baseline
Meas[18]	Baseline
Meas[19]	Baseline
Meas[20]	Baseline
Meas[21]	Active
Meas[22]	Active
Meas[23]	Active
Meas[24]	Active
Meas[25]	Active

BOLD

Meas[26]	Active
Meas[27]	Active
Meas[28]	Active
Meas[29]	Active
Meas[30]	Active
Meas[31]	Active
Meas[32]	Active
Meas[33]	Active
Meas[34]	Active
Meas[35]	Active
Meas[36]	Active
Meas[37]	Active
Meas[38]	Active
Meas[39]	Active
Meas[40]	Active
Motion Correction	Off
Spatial filter	Off
Measurements	304
Delay in TR	0 ms
Multiple series	Off

Sequence - Part 1

Introduction	On
Multi-slice mode	Interleaved
Free echo spacing	Off
Echo spacing	0.5 ms
Bandwidth	2298 Hz/Px

Sequence - Part 2

EPI factor	64
RF pulse type	Normal
Gradient mode	Fast

\\RESEARCH\Jason Parker\Tinnitus\Tinnitus protocol one Imep2d_bold_moco_AUD_STROOP_2
 TA: 10:14 PM: FIX Voxel size: 3.8x3.8x3.0 mmPAT: Off Rel. SNR: 1.00 : epdf

Properties

Prio recon	Off
Load images to viewer	On
Inline movie	Off
Auto store images	On
Load images to stamp segments	Off
Load images to graphic segments	Off
Auto open inline display	Off
Auto close inline display	Off
Start measurement without further preparation	Off
Wait for user to start	On
Start measurements	Single measurement

Routine

Slice group	1
Slices	41
Dist. factor	17 %
Position	Isocenter
Orientation	Transversal
Phase enc. dir.	A >> P
AutoAlign	---
Phase oversampling	0 %
FoV read	240 mm
FoV phase	100.0 %
Slice thickness	3.0 mm
TR	2000 ms
TE	17.0 ms
Averages	1
Concatenations	1
Filter	None
Coil elements	HEA;HEP

Contrast - Common

TR	2000 ms
TE	17.0 ms
MTC	Off
Flip angle	78 deg
Fat suppr.	Fat sat.

Contrast - Dynamic

Averages	1
Averaging mode	Long term
Reconstruction	Magnitude
Measurements	304
Delay in TR	0 ms
Multiple series	Off

Resolution - Common

FoV read	240 mm
FoV phase	100.0 %
Slice thickness	3.0 mm
Base resolution	64
Phase resolution	100 %
Phase partial Fourier	7/8
Interpolation	Off

Resolution - iPAT

PAT mode	None
Matrix Coil Mode	Auto (Triple)

Resolution - Filter Image

Distortion Corr.	Off
Prescan Normalize	Off

Resolution - Filter Rawdata

Raw filter	Off
Elliptical filter	Off
Hamming	Off

Geometry - Common

Slice group	1
Slices	41
Dist. factor	17 %
Position	Isocenter
Orientation	Transversal
Phase enc. dir.	A >> P
FoV read	240 mm
FoV phase	100.0 %
Slice thickness	3.0 mm
TR	2000 ms
Multi-slice mode	Interleaved
Series	Interleaved
Concatenations	1

Geometry - AutoAlign

Slice group	1
AutoAlign	---
Position	Isocenter
Orientation	Transversal
Phase enc. dir.	A >> P
Initial Position	Isocenter
L	0.0 mm
P	0.0 mm
H	0.0 mm
Initial Rotation	0.00 deg
Initial Orientation	Transversal

Geometry - Saturation

Fat suppr.	Fat sat.
Special sat.	None

Geometry - Tim Planning Suite

Set-n-Go Protocol	Off
Table position	H
Table position	0 mm
Inline Composing	Off

System - Miscellaneous

Positioning mode	FIX
Table position	H
Table position	0 mm
MSMA	S - C - T
Sagittal	R >> L
Coronal	A >> P
Transversal	F >> H
Coil Combine Mode	Sum of Squares
Matrix Coil Mode	Auto (Triple)
AutoAlign	---
Coil Select Mode	Off - AutoCoilSelect

System - Adjustments

B0 Shim mode	Standard
B1 Shim mode	TrueForm
Adjust with body coil	Off
Confirm freq. adjustment	Off
Assume Dominant Fat	Off
Assume Silicone	Off
Adjustment Tolerance	Auto

System - Adjust Volume

Position	Isocenter
Orientation	Transversal
Rotation	0.00 deg
A >> P	240 mm
R >> L	240 mm
F >> H	144 mm
Reset	Off

System - Tx/Rx

Frequency 1H	123.259695 MHz
Correction factor	1
Gain	High
Img. Scale Cor.	1.000
Reset	Off
? Ref. amplitude 1H	0.000 V

Physio - Signal1

1st Signal/Mode	None
TR	2000 ms
Concatenations	1

BOLD

GLM Statistics	Off
Dynamic t-maps	Off
Ignore meas. at start	0
Ignore after transition	0
Model transition states	On
Temp. highpass filter	On
Threshold	4.00
Paradigm size	40
Meas[1]	Baseline
Meas[2]	Baseline
Meas[3]	Baseline
Meas[4]	Baseline
Meas[5]	Baseline
Meas[6]	Baseline
Meas[7]	Baseline
Meas[8]	Baseline
Meas[9]	Baseline
Meas[10]	Baseline
Meas[11]	Baseline
Meas[12]	Baseline
Meas[13]	Baseline
Meas[14]	Baseline
Meas[15]	Baseline
Meas[16]	Baseline
Meas[17]	Baseline
Meas[18]	Baseline
Meas[19]	Baseline
Meas[20]	Baseline
Meas[21]	Active
Meas[22]	Active
Meas[23]	Active
Meas[24]	Active
Meas[25]	Active

BOLD

Meas[26]	Active
Meas[27]	Active
Meas[28]	Active
Meas[29]	Active
Meas[30]	Active
Meas[31]	Active
Meas[32]	Active
Meas[33]	Active
Meas[34]	Active
Meas[35]	Active
Meas[36]	Active
Meas[37]	Active
Meas[38]	Active
Meas[39]	Active
Meas[40]	Active
Motion Correction	Off
Spatial filter	Off
Measurements	304
Delay in TR	0 ms
Multiple series	Off

Sequence - Part 1

Introduction	On
Multi-slice mode	Interleaved
Free echo spacing	Off
Echo spacing	0.5 ms
Bandwidth	2298 Hz/Px

Sequence - Part 2

EPI factor	64
RF pulse type	Normal
Gradient mode	Fast

\\RESEARCH\Jason Parker\Tinnitus\Tinnitus protocol one Imlep2d_bold_moco_BRAIN_CONTROL_2
TA: 10:14 PM: FIX Voxel size: 3.8x3.8x3.0 mmPAT: Off Rel. SNR: 1.00 : epfid

Properties

Prio recon	Off
Load images to viewer	On
Inline movie	Off
Auto store images	On
Load images to stamp segments	Off
Load images to graphic segments	Off
Auto open inline display	Off
Auto close inline display	Off
Start measurement without further preparation	Off
Wait for user to start	On
Start measurements	Single measurement

Routine

Slice group	1
Slices	41
Dist. factor	17 %
Position	Isocenter
Orientation	Transversal
Phase enc. dir.	A >> P
AutoAlign	---
Phase oversampling	0 %
FoV read	240 mm
FoV phase	100.0 %
Slice thickness	3.0 mm
TR	2000 ms
TE	17.0 ms
Averages	1
Concatenations	1
Filter	None
Coil elements	HEA,HEP

Contrast - Common

TR	2000 ms
TE	17.0 ms
MTC	Off
Flip angle	78 deg
Fat suppr.	Fat sat.

Contrast - Dynamic

Averages	1
Averaging mode	Long term
Reconstruction	Magnitude
Measurements	304
Delay in TR	0 ms
Multiple series	Off

Resolution - Common

FoV read	240 mm
FoV phase	100.0 %
Slice thickness	3.0 mm
Base resolution	64
Phase resolution	100 %
Phase partial Fourier	7/8
Interpolation	Off

Resolution - iPAT

PAT mode	None
Matrix Coil Mode	Auto (Triple)

Resolution - Filter Image

Distortion Corr.	Off
Prescan Normalize	Off

Resolution - Filter Rawdata

Raw filter	Off
Elliptical filter	Off
Hamming	Off

Geometry - Common

Slice group	1
Slices	41
Dist. factor	17 %
Position	Isocenter
Orientation	Transversal
Phase enc. dir.	A >> P
FoV read	240 mm
FoV phase	100.0 %
Slice thickness	3.0 mm
TR	2000 ms
Multi-slice mode	Interleaved
Series	Interleaved
Concatenations	1

Geometry - AutoAlign

Slice group	1
AutoAlign	---
Position	Isocenter
Orientation	Transversal
Phase enc. dir.	A >> P
Initial Position	Isocenter
L	0.0 mm
P	0.0 mm
H	0.0 mm
Initial Rotation	0.00 deg
Initial Orientation	Transversal

Geometry - Saturation

Fat suppr.	Fat sat.
Special sat.	None

Geometry - Tim Planning Suite

Set-n-Go Protocol	Off
Table position	H
Table position	0 mm
Inline Composing	Off

System - Miscellaneous

Positioning mode	FIX
Table position	H
Table position	0 mm
MSMA	S - C - T
Sagittal	R >> L
Coronal	A >> P
Transversal	F >> H
Coil Combine Mode	Sum of Squares
Matrix Coil Mode	Auto (Triple)
AutoAlign	---
Coil Select Mode	Off - AutoCoilSelect

System - Adjustments

B0 Shim mode	Standard
B1 Shim mode	TrueForm
Adjust with body coil	Off
Confirm freq. adjustment	Off
Assume Dominant Fat	Off
Assume Silicone	Off
Adjustment Tolerance	Auto

System - Adjust Volume

Position	Isocenter
Orientation	Transversal
Rotation	0.00 deg
A >> P	240 mm
R >> L	240 mm
F >> H	144 mm
Reset	Off

System - Tx/Rx

Frequency 1H	123.259695 MHz
Correction factor	1
Gain	High
Img. Scale Cor.	1.000
Reset	Off
? Ref. amplitude 1H	0.000 V

Physio - Signal1

1st Signal/Mode	None
TR	2000 ms
Concatenations	1

BOLD

GLM Statistics	Off
Dynamic t-maps	Off
Ignore meas. at start	0
Ignore after transition	0
Model transition states	On
Temp. highpass filter	On
Threshold	4.00
Paradigm size	40
Meas[1]	Baseline
Meas[2]	Baseline
Meas[3]	Baseline
Meas[4]	Baseline
Meas[5]	Baseline
Meas[6]	Baseline
Meas[7]	Baseline
Meas[8]	Baseline
Meas[9]	Baseline
Meas[10]	Baseline
Meas[11]	Baseline
Meas[12]	Baseline
Meas[13]	Baseline
Meas[14]	Baseline
Meas[15]	Baseline
Meas[16]	Baseline
Meas[17]	Baseline
Meas[18]	Baseline
Meas[19]	Baseline
Meas[20]	Baseline
Meas[21]	Active
Meas[22]	Active
Meas[23]	Active
Meas[24]	Active
Meas[25]	Active

BOLD

Meas[26]	Active
Meas[27]	Active
Meas[28]	Active
Meas[29]	Active
Meas[30]	Active
Meas[31]	Active
Meas[32]	Active
Meas[33]	Active
Meas[34]	Active
Meas[35]	Active
Meas[36]	Active
Meas[37]	Active
Meas[38]	Active
Meas[39]	Active
Meas[40]	Active
Motion Correction	Off
Spatial filter	Off
Measurements	304
Delay in TR	0 ms
Multiple series	Off

Sequence - Part 1

Introduction	On
Multi-slice mode	Interleaved
Free echo spacing	Off
Echo spacing	0.5 ms
Bandwidth	2298 Hz/Px

Sequence - Part 2

EPI factor	64
RF pulse type	Normal
Gradient mode	Fast

PUBLICATIONS

Journal Papers

1. JG Parker, **EE Diller**, S Cao, JT Nelson, K Yeom, C Ho, RM Lober. “Statistical multiscale mapping of IDH1, MGMT, and microvascular proliferation from multiparametric MR and spatially-registered core biopsy.” *Scientific Reports*. 2019.
2. MS Sherwood, JG Parker, **EE Diller**, S Ganapathy, K Bennett, CR Esquivel, JT Nelson. “Self-directed down-regulation of auditory cortex activity mediated by real-time fMRI neurofeedback augments attentional processes, resting cerebral perfusion, and auditory activation.” *NeuroImage*. 2019.
3. MS Sherwood, JG Parker, **EE Diller**, S Ganapathy, K Bennett, JT Nelson. “Volitional down-regulation of the primary auditory cortex via directed attention mediated by real-time fMRI neurofeedback.” *AIMS Neuroscience*. Accepted June 25, 2018. Published July 7, 2018.
4. **EE Diller**, JG Parker, EH Ey, RM Lober. “Transient Neurologic Deficit without Vascular Pathology Correlates with Reversible Focal Hypoperfusion on Arterial Spin Labeled Perfusion Imaging.” *Journal of Pediatric Neurology*. Accepted May 5, 2018. Published June 11, 2018.
5. MS Sherwood, **EE Diller**, EH Ey, S Ganapathy, JT Nelson, JG Parker. “A Protocol for the Administration of Real-Time fMRI Neurofeedback Training.” *Journal of Visualized Experiments (JoVE)*. Accepted March 28, 2017. Published August 25, 2017.

Conference Proceedings

1. **EE Diller**, JG Parker. “PET count variation during PET/MRI acquisition with multiple EPI sequences” *American Association of Physicists in Medicine 2020 Annual Meeting*. Submitted February 26, 2020.
2. B Gray, JG Parker, **EE Diller**, Q Wen, YC Wu, G Anthony, C Ho. “Quantitative T2 values in grading pediatric brain tumors.” *American Society of Neuroradiology (ASNR) 2020 Annual Meeting*. Submitted November 1, 2019.

3. **EE Diller**, JG Parker. “Radiomic variability due from biopsy sampling.” *American Society of Neuroradiology (ASNR) 2020 Annual Meeting*. Submitted November 11, 2019.
4. JG Parker, **EE Diller**, S Cao, JT Nelson, K Yeom, C Ho, RM Lober. “Statistical multiscale mapping of IDH1, MGMT, and microvasculature in human brain tumors from multiparametric MR and registered core biopsy” *International Society for Magnetic Resonance in Medicine (ISMRM) 2020 Annual Meeting*. Submitted November 6, 2019.
5. JG Parker, CY Ho, R Radhakrishnan, **EE Diller**, BP Brown. “Fast Temperature Mapping of the Fetal Brain During Routine 3T MR Imaging” *Radiological Society of North America (RSNA) 2018 Annual Meeting*. Chicago, IL. Accepted July 24, 2018. Presented November 25, 2018.
6. MS Sherwood, **EE Diller**, S Ganapathy, K Bennett, JT Nelson, JG Parker. “Cerebral perfusion is altered by real-time fMRI neurofeedback-directed self-regulation of the primary auditory cortex” *Radiological Society of North America (RSNA) 2018 Annual Meeting*. Chicago, IL. Accepted July 24, 2018. Presented November 28, 2018.
7. MS Sherwood, **EE Diller**, S Ganapathy, K Bennett, JT Nelson, JG Parker. “Alternative tinnitus management techniques developed from volitional control over the activity of the auditory cortex” *Military Health System Research Symposium (MHSRS) 2018 Annual Meeting*. Kissimmee, Florida. August 20-23, 2018.
8. **EE Diller**, RM Lober, JG Parker. “Using Nosologic Imaging Algorithms to Quantitatively Standardize Grade Differentiation in Adult Primary Glioma.” *AAPM 60th Annual Meeting and Exhibition*. Nashville, TN. Presented July 29, 2018.
9. JG Parker, **EE Diller**, RM Lober. “Quantifying individual and collective prediction accuracy of MR contrasts for glioma tissue compartment classification.” *International Society for Magnetic Resonance in Medicine (ISMRM) 2018 Annual Meeting Paris, France*. Presented June 19, 2018.
10. **EE Diller**, RM Lober, JG Parker. “Multiparametric Nosologic Imaging Algorithms: Prognosis Predictions in Glioblastoma.” *5th Indiana Neuroimaging Symposium*. West Lafayette, IN. Presented November 3, 2017.
11. **EE Diller**, RM Lober, MS Sherwood, JG Parker. “Evaluating Glioma Grading Accuracy of a Multiparametric Nosologic Imaging Algorithm” *Radiological Society of North*

- America (RSNA) 2017 Annual Meeting*. Chicago, IL. Accepted June 20, 2017. Presented November 26-December 1, 2017.
12. MS Sherwood, **EE Diller**, JT Nelson, S Ganapathy, JG Parker. "Self-regulation of the primary auditory cortex attention via directed attention mediated by real-time fMRI neurofeedback" *Radiological Society of North America (RSNA) 2017 Annual Meeting*. Chicago, IL. Presented November 26-December 1, 2017.
 13. MS Sherwood, **EE Diller**, S Ganapathy, KB Bennett, JT Nelson, JG Parker. "Self-regulation of primary auditory cortex activity via directed attention mediated by real-time fMRI neurofeedback is related to attentional control processes" *Society for Neuroscience (SfN) 2017 Annual Meeting*. Washington, DC. Presented November 11-15, 2017.
 14. AM Linsk, **EE Diller**, KR Monden, G Sankaranarayanan, W Ahn, CS Awtrey, S De, DB Jones, SD Schwaitzberg, SK Epstein, JM Rideout, CGL Cao. "Comparison of learning curves on the FLS and the Virtual Basic Laparoscopic Skill Trainer (VBLaST): pattern cutting and ligating loop tasks." *Society of American Gastrointestinal and Endoscopy Surgeons (SAGES) 2016 Annual Meeting*. Boston, MA. Presented March 16-19, 2016.
 15. **EE Diller**, CGL Cao. "The Use of Stochastic Resonance in a Two Dimensional Fitts' Task." *Biomedical Engineering Society (BMES) 2015 Annual Meeting*. Tampa, FL. Presented October 7-10, 2015.
 16. KM Babbitt, RD Hoskins, J Wang, **EE Diller**, CGL Cao. "Vibrotactile Feedback and Stochastic Resonance Improves Simulated Laparoscopic Palpation." *American College of Surgeons (ACS) 2015 Clinical Congress*. Chicago, IL. Presented October 4-8, 2015.
 17. RD Hoskins, J Wang, K Babbitt, **EE Diller**, CGL Cao. "Use of stochastic resonance methods for improving laparoscopic surgery performance." *Society of American Gastrointestinal and Endoscopy Surgeons (SAGES) 2015 Annual Meeting*. Nashville, TN. Presented April 15-18, 2015
 18. **EE Diller**, BS Rinehart, JM Allen, TW Merrell Jr, DB Reynolds, CA Phillips. "Pneumatic Muscle Actuator Use in Leg Extension Exercise." *Biomedical Engineering Society (BMES) 2014 Annual Meeting*. San Antonio, Texas. Presented October 22-25, 2014.